A CHEMICAL BIOLOGY APPROACH TOWARDS THE DEVELOPMENT OF STRATEGIES TO TARGET DRUG REFRACTORY BREAST CANCER

by

Rachel Melinda Vaden

A dissertation submitted to the faculty of
The University of Utah
in partial fulfillment of the requirements for the degree of

Doctor of Philosophy

Department of Chemistry

The University of Utah

May 2015

The University of Utah Graduate School

STATEMENT OF DISSERTATION APPROVAL

The dissertation of **Rachel Melinda Vaden**

has been approved by the following supervisory committee members:

Matthew S. Sigman	, Chair	**21 Nov 2014** Date Approved
Gary E. Keck	, Member	**21 Nov 2014** Date Approved
Ryan E. Looper	, Member	**21 Nov 2014** Date Approved
Bethany A. Buck-Koehntop	, Member	**21 Nov 2014** Date Approved
Bryan E. Welm	, Member	**21 Nov 2014** Date Approved

and by **Cynthia J. Burrows** ,

Chair of the Department of **Chemistry**

and by David B. Kieda, Dean of The Graduate School.

ABSTRACT

The occurrence of treatment refractory tumors contributes significantly to the morbidity of cancer. Clinical treatment with chemotherapeutics frequently results in robust initial responses but the majority of patients relapse with drug-insensitive forms of the disease. Considering the lack of therapies available to these patients, our labs implemented a chemical biology approach towards understanding and defining molecular processes of drug-insensitive cancer cells. A small molecule screen was developed with the goal of identifying new molecular tools to characterize vulnerabilities of drug refractory tumor cells. The screen employed malignant pleural effusion cells derived from treatment refractory breast cancer patients in addition to untransformed mammary epithelial cells; the incorporation of untransformed cells in the screen permitted for the identification of small molecules with cancer-specific phenotypes. Fourteen novel small molecules were identified and two of these molecules, C-6 and zinaamidole (ZNA), were chosen for detailed follow-up studies. The first molecule, C-6, was found to be cytotoxic against multiple patient-derived malignant cell types in addition to a variety of breast cancer cell lines, but did not significantly affect to viability of untransformed cells. Next-generation RNA sequencing revealed that C-6 induced endoplasmic reticulum stress and blocked mitochondrial genome transcription. Cells treated with C-6 with disruptions in mitochondrial energy production as assessed by oxygen consumption measurements.

Cancer-specific increases in the oxidation of 2',7'-dichlorodihydrofluorescein diacetate were also observed, indicating that cellular redox states were altered by treatment with C-6. Finally, C-6 was found to induce cancer cell death via a caspase independent mechanism. The second molecule identified, ZNA, contains a cyclic guanidine core and was found to induce metal trafficking gene expression and disrupt Zn^{2+} homeostasis. $CuSO_4$ strongly potentiated ZNA's cytotoxic effects and treatment with ZNA/$CuSO_4$ promoted rapid cell death in both malignant and untransformed cell types. $ZnSO_4$ also potentiated ZNA's cytotoxicity, however, ZNA/$ZnSO_4$ only resulted in cell death in malignant cell types. ZNA and ZNA/$ZnSO_4$ were both found to induce caspase independent cell death selectively in cancer cells. Collectively, these investigations revealed a common theme of caspase independent cell death, suggesting a new strategy for the development of treatments targeting drug insensitive cancers.

To my parents.

TABLE OF CONTENTS

LIST OF TABLES

ACKNOWLEDGEMENTS

During the course of my graduate research, I have been taught, encouraged, supported, and inspired by phenomenal scientists at the University of Utah who have made this work possible. First and foremost, I am indebted to Professor Matt Sigman for his mentorship and guidance as my advisor. He is an exemplary model of progressive scientific thinking and his dedication to scientific research and his students is unmatched. He has taught me to take risks and think critically, and for this I am most grateful. I am also equally indebted to Dr. Bryan Welm. By generously sharing his lab and his time with me for the last five years, he altered my career path in a profound way. As a chemist treading hesitantly into the field of cancer biology, he encouraged my curiosity and patiently helped me develop the skills necessary for my scientific endeavors. I am grateful for the time he took to help me develop as a scientist in the field of molecular biology. I am also thankful for the feedback and advice I have received from each of my committee members during my time at the University of Utah. I am especially grateful to Dr. Ryan Looper for his thoughtful insight on my research throughout graduate school.

As much as I have learned from the faculty at the University of Utah, I have learned from my colleagues. Dr. Elizabeth Bess has taught me to be rigorous and tenacious in my science, but never forget that we are human. Dr. Brittni Smith's optimistic outlook on scientific research has taught me to let failures go and continually

look forward. Dr. Katie Basham's equal dedication to scientific principles and adventure has taught me to be a thorough as a scientist, but don't forget to live. Daria Drobysheva's dedication to her science has taught me to be persistent, be resolute. Celine Santiago has taught me to slow down, be thoughtful, and enjoy the journey of scientific discovery. Finally, Dr. Ryan DeLuca, Dr. Kaid Harper, and Dr. Ben Stokes have taught me that camaraderie and friendships are vital to a healthy and balanced life in science.

This work would not have been possible without the loving support and encouragement of my parents. My father's insatiable curiosity to understand the world around him continually shaped my growth throughout life and engendered me with an inquisitive mind. My mother's organized and detailed nature, coupled with her energetic and determined work ethic, provided me with crucial skills necessary for scientific success. Finally, and most importantly, I am thankful for my husband, Thomas. Through it all, he has been unwavering in his support, love, and encouragement for me. He has been steadfast and committed to this unpredictable adventure since day one and is the single most important contributor to my success. He is completely selfless in support of my ambitions and words cannot express how grateful I am for his companionship and love throughout this process.

CHAPTER 1

AN INTRODUCTION TO CHEMORESISTANCE

The prevalence of cancer in society

Cancer is a leading cause of the death in the United States, second only to heart disease in mortality (1). The impact of the disease is readily apparent when considering that one in three women and one in two men will be diagnosed with cancer during their lifetime (2). Cancer, however, is not a recent development in the history of human maladies; descriptions of the disease can be found from civilizations existing more than 3000 years ago (3). It has long paralleled human existence and has presented a seemingly insurmountable challenge to researchers working to eradicate the disease. Despite significant efforts put forth by the clinical and scientific research communities, the combined cancer mortality rates of men and women decreased by only 12.1% between the years of 1950 and 2010 (2). This statistic alone illustrates the difficult nature of the problem and also alludes to the deep and innate complexity of cancer.

Cancer as a heterogeneous disease

The biological diversity of cancer contributes to its complexity and results in cancer being a collection of diseases rather than a single disorder. Cancer is the product of abnormal cellular growth; growth-deregulated cells propagate and colonize environments within healthy tissue and create a burden that terminally impairs the function of the healthy tissue, ultimately causing host death. An individual tumor is heterogeneous in nature and comprised of many different tumor cell types that vary in cellular function, genetic makeup, and proliferation potential. Collectively, the different populations, or clones, within the tumor coalesce to form complex and dynamic ecosystems that vary in their nutrient and oxygen availability, metastatic potential, and

proliferation rates. This dynamic, phenotypic heterogeneity in tumors is widely acknowledged and hypothesized to significantly affect clinical treatment outcomes in patients. However, the biological basis for the cellular diversity is not fully understood; as such, a better understanding of the source of cellular diversity could play an important role in the development of more effective treatment strategies. Two models have been proposed to explain the basis for the cellular heterogeneity observed within tumors and more recently, a unified model of the two hypotheses has emerged. Notably, the differences in the three models inspire dramatically different treatment strategies for patients.

The cancer stem cell model of tumor heterogeneity

A single type of tissue within an organism is comprised of different cell types that vary in function. Within the tissue, these cells are organized in a hierarchal manner based on their degree of differentiation and functional specialization. The least specialized, least differentiated cells are considered adult stem cells. Stem cells possess the unique ability to self-renew; that is, upon cell division, they can generate either one (asymmetric division) or two (symmetric division) exact copies of the mother cell, which then have the ability to further produce progeny in a similar fashion (reviewed in (4)). Adult stem cells are responsible for the production of highly specialized, fully differentiated cells within tissue. Analogous to healthy tissue, evidence exists to suggest that tumor tissue, being heterogeneous in nature, contains malignant stem cells with self-perpetuating potential. These cells, termed “cancer stem cells” (CSCs), are proposed to engender phenotypic and histological heterogeneity within the tumor (5-7).

Operationally, CSCs are distinguished from other more differentiated cell populations within the tumor based on the expression of specific cell surface proteins; these proteins also facilitate their fractionation and isolation using fluorescence activated cell sorting (FACS). Multiple cell surface proteins have been identified as markers of CSCs and their usage often depends on the origin of the tissue (i.e., lung, liver, brain, breast) (reviewed in (8)). Coupled with the presence of specific cell surface markers, Hoechst nuclear staining and subsequent side population analysis by FACS can also distinguish CSC populations in some cases (9, 10). The ability to isolate specific populations of cells within a heterogeneous tumor has allowed for variations in tumorigenic potential to be studied between cell types. Studies of this nature have revealed that CSCs have a propensity to both initiate tumorigenesis and recapitulate the cellular diversity of the parental tumor when transplanted into a whole organism tumor model (11-14). These reports provide experimental evidence in support of the CSC model and further suggest that tumor heterogeneity arises from a unique subpopulation of cells.

Collectively, literature reports detailing the frequency of CSCs within bulk tumors have indicated that the contribution of CSCs to the overall cell number is highly variable. While results from early studies suggested that CSCs were exceedingly rare, more recent investigations have revealed that the frequency of CSC occurrence can vary dramatically between different malignancies as evidenced by some animal models of cancer and different analyses of human cancers (15-18). However, the use of disparate analytical techniques as well as technical variations in cell isolation and transplantation have been suggested to contribute at least partially towards the variation observed in CSC frequency (19). Considering the literature as a whole though, CSCs are most often thought to

constitute only a small portion of the cell population within solid tumors.

The CSC model does not address the origin of the CSC and two hypotheses are commonly evoked when considering the CSC cell of origin. In the first hypothesis, CSCs are proposed to originate from adult stem or progenitor cells that, upon mutation, become tumorigenic; in the second hypothesis, CSCs are proposed to originate from more differentiated cells that acquire stem-like properties during the course of transformation. These explanations are not considered mutually exclusive and evidence in support of both can be found in various reports, suggesting that the development of transformed cells with stem-like features is context-dependent (20, 21). Regardless of a CSC's cell of origin though, the CSC model proposes that only a subset of cells within the tumor are ultimately responsible for tumor propagation due to their ability to produce differentiated progeny in a hierarchal manner; this differentiated progeny then in turn constitutes the cellular heterogeneity observed in tumors.

The clonal evolution model of tumor heterogeneity

Unlike the CSC model of tumor heterogeneity, the clonal evolution model posits that cellular diversity in tumors can arise from any somatic cell, regardless of its capacity to self-perpetuate and generate more differentiated cell types. In the clonal evolution model, genetic drift and compound mutations produce tumorigenic clones that constantly undergo natural selection as the neoplasm grows, producing the variety of cell types observed. The inherent genetic instability of malignant cells further promotes mutations and contributes to the likelihood that more diverse, and subsequently more fit, clones will be produced (22). This model was first proposed by Nowell in 1976 and based upon

observations that over time, tumors varied in their degree of heterogeneity (23). Further evidence in support of this model can be found in reports detailing the genetic analysis of human hepatocellular carcinoma (HCC); Wu and coworkers conducted whole genome sequencing experiments using spatially sequential sections of human HCC samples (24). Their analyses allowed for the identification of different genetic lineages within the tumor and permitted for the development of a model describing the branching evolution. In all, the researchers concluded that tumors accrued many mutations throughout the course of evolution, but only a small subset of these mutations, termed driver mutations, promoted survival advantages, the remainder of the mutations being inert. In this case, the high degree of mutation diversity observed provides support for the clonal expansion model of tumor heterogeneity wherein many mutations would be expected in many cell types, but only a small number would provide growth and survival advantage.

A unified model of tumor heterogeneity

In all, experimental evidence exists to support both models of genomic and phenotypic heterogeneity in tumors, suggesting that the source of cellular diversity may be context-dependent and that the models are not mutually exclusive. In consideration of this, a unification of the CSC and clonal evolution models has been proposed (25, 26). The unified model states that within a nascent tumor, a cellular hierarchy exists in a manner analogous to nonmalignant tissue; at the top of the hierarchy, a CSC or malignant cell with stem-like capabilities is responsible for the cellular heterogeneity observed. As tumor growth progresses though, the tumor-initiating cell accumulates mutations that promote self-renewal and result in an increased proportion of cells with the capacity to

generate diverse progeny. Later stages of tumor growth are therefore marked by genetically shallow hierarchies that eventually appear homogeneous. As such, the unified model proposes that CSCs (or tumor-initiating cells) are ultimately responsible for tumor heterogeneity but that clonal evolution and selection processes occurs within the CSC population over time. The model also presents an explanation for the variation in CSC frequency observed in different tumors since tumors sampled at different stages will likely vary in their CSC frequency, genetic composition, and phenotype.

Clinical treatment strategies according to tumor heterogeneity models

Each model of tumor heterogeneity has the potential to greatly impact clinical treatment strategies. Historically, treatment success has been a measure of bulk tumor loss; that is, when a therapy stimulates a decrease in the overall size of a tumor or decreases overall tumor burden, the therapy is considered successful. This treatment strategy conforms well to the focus of the clonal evolution model wherein every cell has the potential to propagate tumor growth. In opposition to this, the CSC model suggests that only CSCs or tumor-initiating cells have the regenerative capacity necessary to regrow the tumor; therefore, only therapies targeting tumor-initiating cells will prove successful. The closely related unified model of tumor heterogeneity would also inspire treatment options that target CSCs and tumor-initiating cells. In all though, the three models suggest different clinical strategies for the successful treatment of cancer and the choice of strategy will depend on the genetic and phenotypic composition of the tumor.

The advent of chemotherapy as a treatment for cancer

Current cancer treatment regimens most often rely upon a combination of treatment approaches including surgical resection of the primary tumor, radiation therapy, chemotherapy, and immunotherapy. While the practice of surgical resection has been used therapeutically for thousands of years, the concept of chemotherapeutics emerged only recently. After World War I, it was discovered that nitrogen mustards found in the chemical warfare agent mustard gas could attenuate lymphoma cell proliferation, albeit the effect was temporary (27). Numerous chemical agents and drugs have since been developed for the treatment of cancer and common biological modes of action have stratified these agents into distinct drug classes. Chemotherapeutics can be broadly classified as either cytotoxic therapies or targeted therapies; cytotoxic agents target rapidly proliferating cells, indiscriminately affecting both transformed and untransformed cells, while targeted therapies affect critical biological pathways preferentially in transformed cells (reviewed in (28)). Within these two broad classes of chemotherapeutic drugs, additional classifications can be made based on the molecular mechanism of action. Alkylating agents, antimetabolites, and anthracyclines are examples of cytotoxic therapies that interfere with DNA synthesis and replication; other classes of cytotoxic therapies such as topoisomerase and mitotic inhibitors directly block cell cycle progression (reviewed in (29)). Examples of targeted therapy drug classes include hormone receptor modulators, proteasome inhibitors, monoclonal antibodies, and small molecule kinase inhibitors.

The development of cytotoxic and targeted therapies has significantly expanded available cancer treatment options; current clinical treatment regimens rely heavily upon chemotherapeutics to extend patient survival. Despite the marked improvement in patient

survival achieved through the use of chemotherapeutics though, many patients will still ultimately succumb to the disease. The failure of chemotherapeutics to completely eradicate a patient's disease is due largely to the occurrence of drug resistance. While many tumors initially respond to clinical treatments using chemotherapeutics, drug-insensitive cancer recurrence is commonly observed; as such, preventing and treating chemoresistant tumors could have a significant impact on long-term patient survival.

Molecular mechanisms of cancer chemoresistance

Studies aimed to understand chemoresistance on a cell autonomous level have identified two general forms, innate and acquired; additionally, noncell autonomous mechanisms have been identified for their role in drug resistance. The occurrence of drug resistance in tumors is strongly correlated with poor patient prognosis; understanding the biological basis for the different types of chemoresistance and their contribution to tumor relapse is therefore paramount for the development of improved treatment strategies.

Innate, cell autonomous drug resistance

Innate, cell autonomous drug resistance is often attributed to the existence of CSCs. The results of studies designed to elucidate the role of CSCs in drug resistance have led to the development of a model wherein CSCs are able to survive drug treatment; this small fraction of surviving CSCs are responsible for cancer relapse due to their ability to repopulate the bulk tumor (30-32). To add further complexity to the role of

CSCs in tumor progression, Gurney and coworkers concluded from a study in 2008 that chemotherapeutic drug treatment could enrich for colorectal CSCs in a mouse xenograft model and that regrowth of the population following drug treatment resulted in higher levels of CSCs, an observation proposed to be the consequence of a selection process (33). In a subsequent independent investigation, Lokshin and coworkers similarly concluded that drug treatment enriched for CSCs by using *in vitro* models of breast, ovarian, and lung cancer (34). Furthermore, when the drug insensitive CSC-enriched fraction was allowed to proliferate, the resulting population was less sensitive to subsequent drug treatment, a proposed result of the higher percentage of innate, drug resistant CSCs. Overall, multiple research studies have established a connection between CSCs and drug treatment. This connection has led to the development of a hypothesis that suggests that standard clinical chemotherapy treatments may promote CSC enrichment and ultimately contribute to drug refractory tumor relapse.

That cancer stem cells may contribute to drug resistant tumor relapse acknowledges a commonly observed characteristic of the cell type: an intrinsic insensitivity to cytotoxic insult compared to their more differentiated counterparts. Research conducted to establish the biological basis for this phenomenon has led to the development of several potential mechanistic explanations including increased expression of small molecule efflux transporters, increased expression of intracellular drug detoxification enzymes, and highly efficient DNA damage repair mechanisms.

One parameter frequently used to identify and isolate CSCs by FACS is based on the side population (SP) phenotype, the observation that CSCs within a heterogeneous cell population resist Hoechst nuclear stain and segregate into a negatively stained side population. Studies by Sorrentino and coworkers undertaken to elucidate the molecular

basis for the phenotype revealed ABCG2, an ATP-binding cassette (ABC) transporter protein, mediated Hoechst stain efflux, resulting in the negatively stained side population; the authors found that ABCG2 was highly expressed in CSCs from a variety of sources and proposed its use as a molecular marker for CSC identification (35). The culmination of this and other scientific reports in the field has been the identification of additional proteins within the ABC transporter family that are also highly expressed in CSCs (reviewed in (36)). Functionally, these transporters utilize ATP to actively efflux drugs from the intracellular space; as such, the high expression of drug efflux proteins in CSCs can confer a significant survival advantage to the cell during chemotherapeutic treatment compared to the more differentiated population within the bulk tumor. The increased expression of drug efflux proteins therefore constitutes an innate mechanism by which some populations of tumor cells can evade clinical therapies.

The increased expression of intracellular drug detoxification enzymes also contributes to CSC survival during drug treatment. Using an *in vitro* mammary epithelial cell assay, Dontu and coworkers established that the enzyme aldehyde dehydrogenase 1 (ALDH1) could be used as a marker for the identification of both normal mammary epithelial stem cells and breast cancer stem cells (37). The enzyme ALDH1 oxidizes aldehydes to carboxylic acids and its increased expression in stem cells is hypothesized to facilitate early normal development by oxidizing retinol to retinoic acid, a tightly regulated molecule that signals critical transcriptional activation and repression events during embryonic development (38). In 1984, a correlation between high ALDH1 expression and cyclophosphamide drug resistance was made using the leukemia cell line L1210 (39). Further investigation revealed that ALDH1 directly acted upon cyclophosphamide, oxidizing it to an inactive metabolite, carboxycyclophosphamide, and

rendering its drug function inert (40). Since these initial discoveries connecting ALDH1 to cyclophosphamide resistance, additional correlations have been made between high expression of ALDH enzymes and resistance to other anticancer therapeutics (41, 42). As such, heightened expression of detoxification enzymes such as ALDH1 likely contributes to innate mechanisms by which CSCs resist drug treatment.

Altered DNA damage response pathways are also hypothesized to contribute to the innate, cell autonomous resistance of CSCs to tumor drug treatment. All cell types within the body must frequently contend with DNA-damaging insults. DNA lesions can occur via many different mechanisms including spontaneous hydrolysis and base deamination, exposure to reactive oxygen species generated by metabolic processes, exposure to UV light and ionizing radiation, and exposure to external environmental mutagens (reviewed in (43, 44)). In order to cope with the various forms of molecular damage induced by these insults, cells utilize multiple repair mechanisms to mitigate genomic damage. Since adult stem cells are responsible for tissue maintenance and homeostasis of an organism, genomic integrity must be well preserved to ensure that genetic mutations are not transferred to differentiated progeny. The privileged nature of the stem cell therefore necessitates highly efficient mechanisms to both prevent and repair damage to the genome. One general mechanism by which the potential for DNA damage can be prevented or lessened in tissue-specific stem cells is through decreased rates in cell cycling, or proliferative quiescence; in nontumorigenic settings, the relatively dormant nature of adult stem cells offers the advantage of minimizing replication-based errors (45-47). In a tumor setting, however, CSCs possessing this particular feature are intrinsically less sensitive to cytotoxic cancer therapeutics that target rapidly proliferating cells; drug treatment can therefore enrich for populations with innately slow cell cycles

and render the treatment ineffective (48).

In addition to this general mechanism of CSC drug resistance, more specific molecular alterations in DNA damage repair pathways also exist preferentially in CSCs over the bulk of tumor cells and contribute to innate, cell autonomous drug resistance. Through transcriptional profiling of murine mammary cell populations, Rosen and coworkers found that the expression of DNA damage repair genes was increased in the CSC population; this transcriptional increase was correlated with more efficient repair of ionizing radiation-induced damage compared to the more differentiated cells within the tumor (49). In the context of cancer chemotherapy, increased DNA repair efficiency would be expected to impart a certain level of intrinsic resistance to DNA damaging therapeutics. Consistent with this expectation, Rich and coworkers observed that compared to neighboring differentiated cells, glioma stem cells were more resistant to ionizing radiation due to their increased capacity for DNA repair (31). Overall, the reports of these and others suggest that the efficient mechanisms by which CSCs repair damaged DNA can contribute at least in part to innate, cell autonomous chemotherapy resistance.

Acquired, cell autonomous drug resistance

Acquired, cell autonomous drug resistance constitutes a significant portion of the research conducted on cancer chemoresistance to date. Drug treatment perturbs the dynamic nature of the tumor milieu and accordingly, a tumor can develop adaptive responses to manage disruptions. Multiple adaptive response mechanisms have been identified in tumors and generalized mechanisms include drug target modifications, DNA

damage repair pathway modifications, and improved drug efflux mechanisms. These adaptive responses can precede drug resistance and contribute to chemotherapeutic failures and tumor relapse.

Drug target modifications leading to decreased drug sensitivity can include both direct modification of the drug-protein interface via genetic mutations or increased expression of the protein target. This type of resistance is frequently observed with small molecule kinase inhibitors such as imatinib, in the case of chronic myelogenous leukemia, and erlotinib, in the case of non-small cell lung cancer (NSCLC) (50-53). With both molecules, mutations at the drug-protein interface decrease the binding affinity of the drug and result in the emergence of resistance. In examples such as these, synthetic modifications made to the small molecule to reestablish drug sensitivity can prolong the therapeutic benefits of targeting the protein.

Amplified expression of genes encoding for drug-targeted proteins and their related pathway proteins also contributes to drug resistance in cancer; however, this form of drug resistance is reported to be less prevalent compared to direct mutation of the target protein (54). Utilizing *in vitro* models of NSCLC, Janne and coworkers reported that treatment with an irreversible epidermal growth factor receptor (EGFR) inhibitor resulted in the selection of a small subset of cells (6%) harboring an EGFR amplification; upon repopulation after treatment, 100% of cells contained the EGFR amplification (55). In all, altered drug targets, occurring through either mutations or increased expression, can impact the success of targeted cancer therapeutics and result in tumor relapse even after a robust initial treatment response.

Altered DNA damage response (DDR) pathways can also contribute to drug resistance. Most commonly used chemotherapies function mechanistically by interfering

with DNA synthesis or replication and include drugs such as cisplatin (a DNA crosslinker), cyclophosphamide (a DNA alkylating agent that interferes with replication), and doxorubicin (a topoisomerase II inhibitor). Following a DNA-targeted insult, normal, untransformed cells will either arrest the cell cycle and repair the damage or initiate cell death, each as a means to maintain long-term genomic integrity; when repair processes are utilized, the repair pathway activated depends upon the type of damage sustained (for a review of the DNA damage response, see (44)). In tumor cells, defects in specific repair mechanisms can be exploited for treatment gain, as is the case with breast cancers harboring BRCA1 and BRCA2 mutations. With these tumors, the homologous recombination (HR) repair pathway is ineffective and cells rely heavily upon alternative pathways for DNA damage repair. Accordingly, in studies conducted by Ashworth and coworkers, pharmacologic inhibition of the base excision repair (BER) repair pathway in *BRCA1*- and *BRCA2*-deficient systems resulted in significant cell death in *in vitro* assays and blocked tumor formation in an *in vivo* xenograft tumor model (56). The profound synthetic lethality observed in this case has generated significant enthusiasm in the research community and clinical trials aimed to test this strategy are ongoing. However, indications of resistance have already been reported; secondary mutations in *Brca1* and *Brca2* that restore the function of the HR repair pathway have been identified (57, 58). In addition to this resistance mechanism, Nussenzweig and coworkers demonstrated that cells could also utilize other repair pathways, the non-homologous end joining pathway, as a means to survive drug treatment (59). Whether via pathway reactivation or transfer of the genomic repair burden to alternative repair pathways, these examples illustrate how changes in the DDR pathway can facilitate drug resistance in tumors treated with DNA damaging chemotherapeutics.

The increased capacity of tumor cells to efflux small molecules also represents an adaptive response to chemotherapy, wherein increased efflux results in lowered drug accumulation, rendering the treatment ineffective. Similarly to CSCs, ATP-binding cassette (ABC) transporter proteins are thought to be responsible for this effect. By profiling 23 drug resistant human cell lines and comparing them to their drug-sensitive counterparts, Inazawa and coworkers found that alterations in the copy numbers of ABC transporter genes correlated with resistance (60). More specifically, 19 of the 23 drug-resistant lines had amplifications in at least one ABC transporter gene, with *ABCA3*, *ABCB1*, and *ABCC9* presenting with greater than a two-fold increase. While *ABCB1* was known previously to contribute to acquired resistance, the study also implicated 10 other ABC family members whose involvement had not been previously linked. Together, these results suggest that multiple ABC family members may contribute to drug resistance by promoting drug efflux.

Acquired, cell autonomous drug resistance represents a well-studied area of drug resistance. However, the mechanisms of resistance described here represent only a fraction of those that have been reported. Cancer's genomic instability provides a consistent source of cellular variety; coupled with selective pressure from drug treatment, the survival of cells with improved fitness characteristics can allow for the tumor to circumvent chemotherapeutic treatment. As such, it is reasonable to consider that improved early cancer detection, before the accumulation of mutations and the further diversification of cell types, could significantly reduce the ability of the tumor to acquire resistance.

Non-cell autonomous drug resistance

Non-cell autonomous drug resistance represents an emerging field of study in oncological research; this form of drug resistance describes the contribution of the stroma and tumor microenvironment to drug insensitivity in tumors. It is becoming increasingly apparent that non-cell autonomous mechanisms play a significant role in tumor progression via the tumor's ability to manipulate nonmalignant cells and exploit their normal function. Better understanding the interactions of these components of noncell autonomous drug resistance with the tumor is therefore vital to developing improved strategies to overcome chemoresistance in patients.

The connective and structurally supportive nonmalignant tissue that surrounds a tumor is known as the stroma, which consists of several different cell types; the coordinating nature of the stroma and the tumor together form the tumor microenvironment. While the stroma initially exists outside of the nascent tumor, it will increasingly incorporate and blend with the tumor as the tumor grows and expands (for a review of stromal contribution to neoplastic progression, see (61)). The stroma can be coaxed to facilitate tumor expansion by exposure to growth factors produced by malignant cells; several well-studied growth factors known to participate in this process include epidermal growth factor (EGF), fibroblast growth factor (FGF), and platelet-derived growth factor (PDGF). Fibroblasts, one of the cell types that comprises the nonmalignant stroma, can acquire an "activated" phenotype during tumorigenesis. The resulting cells, referred to as myofibroblasts or carcinoma-associated fibroblasts (CAFs), express altered cell surface markers and possess the ability to remodel the structural components of the tumor stroma (62-66). Considering the complex function of the stroma in carcinogenesis, it is reasonable to consider that it may also participate in

chemoresistance. Accordingly, Golub and colleagues cultivated 45 cancer cell lines with 23 different stromal cell lines and found that, in general, the presence of stromal cells altered cancer cell sensitivity to chemotherapeutics (67). Moreover, evidence of resistance to targeted therapies, as opposed to conventional cytotoxic therapies, was found in 65% of the conditions tested. While explanations to understand the molecular basis for this effect with specific targeted therapies have yet to be determined, evidence has been presented to suggest that stromal secretion of hepatocyte growth factor (HGF) and subsequent activation of MAPK signaling in BRAF-mutant melanoma cells is sufficient to induce resistance to small molecule RAF inhibitors (67). In all, stromal-driven resistance to anticancer agents is a largely underdeveloped area of research; the sparse number of results that have been reported, however, suggest that the stroma can significantly modulate a patient's response to chemotherapeutic treatment.

Strategies for the treatment of chemoresistant tumors

The mechanisms by which malignant cells limit the efficacy of cancer treatments described herein represent only a fraction of the mechanisms that have been reported; however, even from this subset, the diversity of cellular mechanisms is apparent. As such, developing strategies to treat drug-insensitive cancers will require a personalized approach and comprehensive knowledge of each patient's malignancy. Several approaches have been taken to combat frequently occurring forms of resistance, though. Two of these strategies include the development of ABC transporter inhibitors and pharmacologic agents that target CSCs.

A considerable number of studies have been conducted to assess the affects of

ABC transporter inhibition on anticancer drug sensitivity with the goal of preventing drug efflux. In early clinical trials, drugs with inhibitor activity that had already obtained FDA-approval to treat unrelated medical conditions were used. However, the first clinical trials were unable to demonstrate drug efficacy with these first generation drugs and some drugs resulted in significant systemic toxicity (68, 69). Unfortunately, later generation drugs designed to target specific ABC transporters also failed clinical trials, with most proving to be ineffective at reversing chemoresistance (70-73). As a class, ABC transporter inhibitors have yet to be implemented in clinical treatment regimens and some hypotheses have been proposed to explain their failures in clinical trials including off-target actions against unrelated P450 enzymes and poor clinical trial design (i.e., trials that examine late stages of chemoresistance) (74, 75).

Another strategy currently being explored for the treatment of drug refractory cancers is the development of pharmacologic agents that target CSCs. To date, several drugs have been identified for their preferential cytotoxicity towards CSCs. Low-dose metformin, which is used in the treatment of diabetes, was found to selectively eliminate CSCs and also promote relapse-free survival in a mouse xenograft tumor model (76). Combined with traditional chemotherapeutic drugs to eliminate more differentiated, bulk tumor cells, this approach shows promise for the treatment of drug insensitive tumors and other reports have identified additional pharmacologic agents that act against CSCs in a manner similar to metformin (77, 78). In addition to strategies designed to directly eliminate CSCs, another complementary approach has been proposed: forced differentiation. Lander and colleagues identified the small molecule salinomycin from a high throughput screen for its ability to reduce the number of CSCs in a heterogeneous cell population compared to treatment with conventional chemotherapeutics (79, 80).

Further analysis of salinomycin's mechanism of action revealed that it reduced CSC numbers by inducing differentiation, suggesting that forced CSC differentiation may be a viable approach to target innately drug insensitive CSCs in tumors. In all, the results of multiple studies have suggested that targeting CSCs, either by elimination or forced differentiation, is a promising approach towards the development of new therapeutics against chemoresistant cancers.

Conclusion

The development of chemoresistance in tumors following an initial positive response to treatment is commonly observed following the administration of chemotherapeutics. The tumor landscape is heterogeneous and dynamic, with evidence to suggest these characteristics become more prominent during tumor progression; as such, tumors can utilize an overwhelming number of biological mechanisms to recover from the perturbations induced by drug treatment. The specific resistance mechanisms discussed here represent only a small subset of those that have been identified. The sheer number of mechanisms existing has thus presented the greatest challenge for new treatment development; currently, only a limited number of clinical treatment strategies targeting these mechanisms have been developed. Furthermore, overcoming the barrier of drug insensitivity will likely require detailed knowledge of each tumor's cellular composition and level of heterogeneity before a treatment can be successfully implemented. The work presented herein describes our efforts to identify vulnerabilities of chemoresistant cells that can be targeted therapeutically. With this body of work, we aim to both add to our current understanding of cancer biology and provide insight into

strategies for the development of new therapeutics.

References

1. Siegel R, Ma J, Zou Z, & Jemal A (2014) Cancer statistics, 2014. *CA Cancer J Clin* 64(1):9-29.

2. Howlader N*, et al.* (2013) SEER Cancer Statistics Review, 1975-2010. *National Cancer Institute*, Bethesda, MD.

3. (translator) BE & Banov L (1937) *The Papyrus Ebers: The Greatest Egyptian Medical Document* (Copenhagen, Levin & Munksgaard).

4. Morrison SJ & Kimble J (2006) Asymmetric and symmetric stem-cell divisions in development and cancer. *Nature* 441(7097):1068-1074.

5. Lapidot T*, et al.* (1994) A cell initiating human acute myeloid leukaemia after transplantation into SCID mice. *Nature* 367(6464):645-648.

6. Jiang X*, et al.* (2007) Chronic myeloid leukemia stem cells possess multiple unique features of resistance to BCR-ABL targeted therapies. *Leukemia* 21(5):926-935.

7. Pierce GB & Speers WC (1988) Tumors as caricatures of the process of tissue renewal: prospects for therapy by directing differentiation. *Cancer Res* 48(8):1996-2004.

8. Visvader JE & Lindeman GJ (2008) Cancer stem cells in solid tumours: accumulating evidence and unresolved questions. *Nat Rev Cancer* 8(10):755-768.

9. Patrawala L*, et al.* (2005) Side population is enriched in tumorigenic, stem-like cancer cells, whereas ABCG2+ and ABCG2− cancer cells are similarly tumorigenic. *Cancer Res* 65(14):6207-6219.

10. Kondo T, Setoguchi T, & Taga T (2004) Persistence of a small subpopulation of cancer stem-like cells in the C6 glioma cell line. *Proc Natl Acad Sci USA* 101(3):781-786.

11. O/'Brien CA, Pollett A, Gallinger S, & Dick JE (2007) A human colon cancer cell capable of initiating tumour growth in immunodeficient mice. *Nature* 445(7123):106-110.

12. Curley MD*, et al.* (2009) CD133 expression defines a tumor initiating cell

population in primary human ovarian cancer. *Stem Cells* 27(12):2875-2883.

13. Prince ME*, et al.* (2007) Identification of a subpopulation of cells with cancer stem cell properties in head and neck squamous cell carcinoma. *Proc Natl Acad Sci USA* 104(3):973-978.

14. Suvà M-L*, et al.* (2009) Identification of cancer stem cells in ewing's sarcoma. *Cancer Res* 69(5):1776-1781.

15. Ishizawa K*, et al.* (2010) Tumor-initiating cells are rare in many human tumors. *Cell Stem Cell* 7(3):279-282.

16. Kelly PN, Dakic A, Adams JM, Nutt SL, & Strasser A (2007) Tumor growth need not be driven by rare cancer stem cells. *Science* 317(5836):337.

17. Schatton T*, et al.* (2008) Identification of cells initiating human melanomas. *Nature* 451(7176):345-349.

18. Quintana E*, et al.* (2008) Efficient tumour formation by single human melanoma cells. *Nature* 456(7222):593-598.

19. dos Santos RV & da Silva LM (2013) A possible explanation for the variable frequencies of cancer stem cells in tumors. *PLoS ONE* 8(8):e69131.

20. Tan BT, Park CY, Ailles LE, & Weissman IL (2006) The cancer stem cell hypothesis: a work in progress. *Lab Investigation* 86(12):1203-1207.

21. O'Connor ML*, et al.* (2014) Cancer stem cells: a contentious hypothesis now moving forward. *Cancer Lett* 344(2):180-187.

22. Cahill DP, Kinzler KW, Vogelstein B, & Lengauer C (1999) Genetic instability and darwinian selection in tumours. *Trends Genet* 15(12):M57-M60.

23. Nowell P (1976) The clonal evolution of tumor cell populations. *Science* 194(4260):23-28.

24. Tao Y*, et al.* (2011) Rapid growth of a hepatocellular carcinoma and the driving mutations revealed by cell-population genetic analysis of whole-genome data. *Proc Natl Acad Sci USA* 108(29):12042-12047.

25. Campbell LL & Polyak K (2007) Breast tumor heterogeneity: cancer stem cells or clonal evolution? *Cell Cycle* 6(19):2332-2338.

26. Kreso A & Dick John E (2014) Evolution of the cancer stem cell model. *Cell Stem Cell* 14(3):275-291.

27. DeVita VT & Chu E (2008) A history of cancer chemotherapy. *Cancer Res*

68(21):8643-8653.

28. Ciavarella S, Milano A, Dammacco F, & Silvestris F (2010) Targeted therapies in cancer. *BioDrugs* 24(2):77-88.

29. Malhotra V & Perry MC (2003) Classical chemotherapy: mechanisms, toxicities and the therapeutc window. *Cancer Biol Ther* 2(0):1-3.

30. Li X*, et al.* (2008) Intrinsic resistance of tumorigenic breast cancer cells to chemotherapy. *J Natl Cancer Inst* 100(9):672-679.

31. Bao S*, et al.* (2006) Glioma stem cells promote radioresistance by preferential activation of the DNA damage response. *Nature* 444(7120):756-760.

32. Woodward WA*, et al.* (2007) WNT/β-catenin mediates radiation resistance of mouse mammary progenitor cells. *Proc Natl Acad Sci USA* 104(2):618-623.

33. Dylla SJ*, et al.* (2008) Colorectal cancer stem cells are enriched in xenogeneic tumors following chemotherapy. *PLoS ONE* 3(6):e2428.

34. Levina V, Marrangoni AM, DeMarco R, Gorelik E, & Lokshin AE (2008) Drug-selected human lung cancer stem cells: cytokine network, tumorigenic and metastatic properties. *PLoS ONE* 3(8):e3077.

35. Zhou S*, et al.* (2001) The ABC transporter Bcrp1/ABCG2 is expressed in a wide variety of stem cells and is a molecular determinant of the side-population phenotype. *Nat Med* 7(9):1028-1034.

36. Dean M (2009) ABC transporters, drug resistance, and cancer stem cells. *J Mammary Gland Biol Neoplasia* 14(1):3-9.

37. Ginestier C*, et al.* (2007) ALDH1 is a marker of normal and malignant human mammary stem cells and a predictor of poor clinical outcome. *Cell Stem Cell* 1(5):555-567.

38. Mangelsdorf DJ*, et al.* (1992) Characterization of three RXR genes that mediate the action of 9-cis retinoic acid. *Genes Dev* 6(3):329-344.

39. Hilton J (1984) Role of aldehyde dehydrogenase in cyclophosphamide-resistant l1210 leukemia. *Cancer Res* 44(11):5156-5160.

40. Russo JE & Hilton J (1988) Characterization of cytosolic aldehyde dehydrogenase from cyclophosphamide resistant l1210 cells. *Cancer Res* 48(11):2963-2968.

41. Duong H*, et al.* (2012) Aldehyde dehydrogenase 1A1 confers intrinsic and acquired resistance to gemcitabine in human pancreatic adenocarcinoma MIA PaCa-2 cells. *Int J Oncol* 41(3):855-861.

42. Awad O*, et al.* (2010) High ALDH activity identifies chemotherapy-resistant ewing's sarcoma stem cells that retain sensitivity to EWS-FLI1 inhibition. *PLoS ONE* 5(11):e13943.

43. Sancar A, Lindsey-Boltz LA, Ünsal-Kaçmaz K, & Linn S (2004) Molecular mechanisms of mammalian DNA repair and the DNA damage checkpoints. *Annu Rev Biochem* 73(1):39-85.

44. Jackson SP & Bartek J (2009) The DNA-damage response in human biology and disease. *Nature* 461(7267):1071-1078.

45. Orford KW & Scadden DT (2008) Deconstructing stem cell self-renewal: genetic insights into cell-cycle regulation. *Nat Rev Genet* 9(2):115-128.

46. Cheshier SH, Morrison SJ, Liao X, & Weissman IL (1999) In vivo proliferation and cell cycle kinetics of long-term self-renewing hematopoietic stem cells. *Proc Natl Acad Sci USA* 96(6):3120-3125.

47. Beerman I, Seita J, Inlay Matthew A, Weissman Irving L, & Rossi Derrick J (2014) Quiescent hematopoietic stem cells accumulate dna damage during aging that is repaired upon entry into cell cycle. *Cell Stem Cell* 15(1):37-50.

48. Calcagno AM*, et al.* (2010) Prolonged drug selection of breast cancer cells and enrichment of cancer stem cell characteristics. *J Natl Cancer Inst* 102(21):1637-1652.

49. Zhang M, Atkinson RL, & Rosen JM (2010) Selective targeting of radiation-resistant tumor-initiating cells. *Proc Natl Acad Sci USA* 107(8):3522-3527.

50. Branford S*, et al.* (2003) Detection of BCR-ABL mutations in patients with CML treated with imatinib is virtually always accompanied by clinical resistance, and mutations in the ATP phosphate-binding loop (P-loop) are associated with a poor prognosis. *Blood* 102(1):276-283.

51. Balak MN*, et al.* (2006) Novel D761Y and common secondary T790M mutations in epidermal growth factor receptor–mutant lung adenocarcinomas with acquired resistance to kinase inhibitors. *Clin Cancer Res* 12(21):6494-6501.

52. Yun C-H*, et al.* (2008) The T790M mutation in EGFR kinase causes drug resistance by increasing the affinity for ATP. *Proc Natl Acad Sci USA* 105(6):2070-2075.

53. Gorre ME*, et al.* (2001) Clinical resistance to STI-571 cancer therapy caused by bcr-abl gene mutation or amplification. *Science* 293(5531):876-880.

54. Sequist LV*, et al.* (2011) Genotypic and histological evolution of lung cancers acquiring resistance to EGFR inhibitors. *Sci Transl Med* 3(75):75ra26.

55. Ercan D, *et al.* (2010) Amplification of EGFR T790M causes resistance to an irreversible EGFR inhibitor. *Oncogene* 29(16):2346-2356.

56. Farmer H, *et al.* (2005) Targeting the DNA repair defect in BRCA mutant cells as a therapeutic strategy. *Nature* 434(7035):917-921.

57. Sakai W, *et al.* (2009) Functional restoration of BRCA2 rrotein by secondary BRCA2 mutations in BRCA2-mutated ovarian carcinoma. *Cancer Res* 69(16):6381-6386.

58. Swisher EM, *et al.* (2008) Secondary BRCA1 mutations in BRCA1-mutated ovarian carcinomas with platinum resistance. *Cancer Res* 68(8):2581-2586.

59. Bunting SF, *et al.* (2010) 53BP1 Inhibits homologous recombination in brca1-deficient cells by blocking resection of DNA breaks. *Cell* 141(2):243-254.

60. Yasui K, *et al.* (2004) Alteration in copy numbers of genes as a mechanism for acquired drug resistance. *Cancer Res* 64(4):1403-1410.

61. Tlsty TD & Coussens LM (2006) Tumor stroma and regulation of cancer development. *Annu Rev Pathol* 1(1):119-150.

62. Rockey DC, Weymouth N, & Shi Z (2013) Smooth muscle α actin (Acta2) and myofibroblast function during hepatic wound healing. *PLoS ONE* 8(10):e77166.

63. Olumi AF, *et al.* (1999) Carcinoma-associated fibroblasts direct tumor progression of initiated human prostatic epithelium. *Cancer Res* 59(19):5002-5011.

64. Erez N, Truitt M, Olson P, & Hanahan D (2010) Cancer-associated fibroblasts are activated in incipient neoplasia to orchestrate tumor-promoting inflammation in an NF-κB-dependent manner. *Cancer Cell* 17(2):135-147.

65. Bailey JM, *et al.* (2008) Sonic hedgehog promotes desmoplasia in pancreatic cancer. *Clin Cancer Res* 14(19):5995-6004.

66. Müerköster SS, *et al.* (2008) Role of myofibroblasts in innate chemoresistance of pancreatic carcinoma—Epigenetic downregulation of caspases. *Int J Cancer* 123(8):1751-1760.

67. Straussman R, *et al.* (2012) Tumour micro-environment elicits innate resistance to RAF inhibitors through HGF secretion. *Nature* 487(7408):500-504.

68. Ozols RF, *et al.* (1987) Verapamil and adriamycin in the treatment of drug-resistant ovarian cancer patients. *J Clin Oncol* 5(4):641-647.

69. Solary E, *et al.* (2003) Quinine as a multidrug resistance inhibitor: a phase 3

multicentric randomized study in adult de novo acute myelogenous leukemia. *Blood* 102(4):1202-1210.

70. Saeki T*, et al.* (2007) Dofequidar fumarate (MS-209) in combination with cyclophosphamide, doxorubicin, and fluorouracil for patients with advanced or recurrent breast cancer. *J Clin Oncol* 25(4):411-417.

71. Greenberg PL*, et al.* (2004) Mitoxantrone, etoposide, and cytarabine with or without valspodar in patients with relapsed or refractory acute myeloid leukemia and high-risk myelodysplastic syndrome: a phase III trial (E2995). *J Clin Oncol* 22(6):1078-1086.

72. Reyno L*, et al.* (2004) Phase III study of N,N-Diethyl-2-[4-(phenylmethyl) phenoxy]ethanamine (BMS-217380-01) combined with doxorubicin versus doxorubicin alone in metastatic/recurrent breast cancer: National Cancer Institute of Canada Clinical Trials Group Study MA.19. *J Clin Oncol* 22(2):269-276.

73. Cripe LD*, et al.* (2010) Zosuquidar, a novel modulator of P-glycoprotein, does not improve the outcome of older patients with newly diagnosed acute myeloid leukemia: a randomized, placebo-controlled trial of the Eastern Cooperative Oncology Group 3999. *Blood* 116(20):4077-4085.

74. Englund G*, et al.* (2014) Cytochrome P450 inhibitory properties of common efflux transporter inhibitors. *Drug Metab Dispos* 42(3):441-447.

75. Yu M, Ocana A, & Tannock I (2013) Reversal of ATP-binding cassette drug transporter activity to modulate chemoresistance: why has it failed to provide clinical benefit? *Cancer Metastasis Rev* 32(1-2):211-227.

76. Hirsch HA, Iliopoulos D, Tsichlis PN, & Struhl K (2009) Metformin selectively targets cancer stem cells, and acts together with chemotherapy to block tumor growth and prolong remission. *Cancer Res* 69(19):7507-7511.

77. Lagadinou Eleni D*, et al.* (2013) BCL-2 Inhibition targets oxidative phosphorylation and selectively eradicates quiescent human leukemia stem cells. *Cell Stem Cell* 12(3):329-341.

78. Ben-David U, Nudel N, & Benvenisty N (2013) Immunologic and chemical targeting of the tight-junction protein Claudin-6 eliminates tumorigenic human pluripotent stem cells. *Nat Commun* 4.

79. Gupta PB*, et al.* (2009) Identification of selective inhibitors of cancer stem cells by high-throughput screening. *Cell* 138(4):645-659.

80. Beug H (2009) Breast cancer stem cells: eradication by differentiation therapy? *Cell* 138(4):623-625.

CHAPTER 2

DEVELOPMENT OF A SCREEN TO IDENTIFY SMALL MOLECULE TOOLS FOR THE STUDY OF DRUG-INSENSITIVE CANCERS

Results of the studies presented herein have been published: Gligorich KM, Vaden RV, *et al.* (2013) Development of a screen to identify selective small molecules active against patient-derived metastatic and chemoresistant breast cancer cells. *Breast Cancer Res* 15(4):R58.

Abstract

The occurrence of treatment refractory tumors contributes significantly to the morbidity of cancer. On a molecular level, a plethora of mechanisms contributing to anti-cancer drug resistance have been identified. For this reason, modeling chemoresistance and its heterogeneity has presented a challenge to the development of therapeutics that are effective against the drug refractory disease. With the goal of identifying new chemical tools for the study of late-stage cancers, we utilized an *in vitro* model of breast cancer that recapitulates clinically relevant features of heterogeneity and drug resistance to conduct a small molecule screen. The model utilizes metastatic cells obtained from the pleural effusions of breast cancer patients that have undergone clinical treatment with multiple frontline chemotherapeutics; the small molecule screen was designed to identify novel compounds that induce cancer cell death. In all, fourteen small molecules inducing cytotoxic, cancer-selective phenotypes were identified. The incorporation of this specialized *in vitro* model into our chemical biology approach towards understanding advanced-stage, drug-insensitive breast cancer has resulted in the identification of new tools for disease study.

Introduction

Breast cancer is currently the second leading cause of cancer-related deaths among women in the United States and more than 230,000 women were diagnosed with the disease in 2013 alone (1). As with many cancers, one challenge associated with its treatment is its heterogeneity. An individual neoplasm generally contains a variety of cell types that can vary significantly in genomic and molecular composition. Healthy breast

tissue is composed of a variety of cell types that coalesce to form the tissue architecture and this variety of cell types found in healthy tissue adds an additional layer of complexity to tumors arising form the breast.

Breast cancer cell lines are the most frequently used models of the disease and have contributed significantly not only to our understanding of cancer, but also molecular biology in general (2, 3). Different cell lines represent a wide variety of malignancies and serve as renewable and standardized resources for disease research. Furthermore, the capacity of cell lines to be expanded has historically allowed for experiments to be conducted that require significant amounts of biological material, although newer, more sensitive technologies have abrogated this need to some extent.

Even though cancer cell lines constitute a vital component of biomedical research and they model many aspects of the disease, not all features are accurately represented. Specifically, breast cancer cell lines are homogeneous in nature, as a result of selection processes during long-term culture, and do not reflect the cellular diversity and heterogeneity of the disease found in patients (4, 5). Additionally, artificial culture environments have selected for rapidly proliferating cell populations over time, another divergence from the phenotypes observed in patients' diseases (6, 7). Finally, breast cancer patients are exposed to multiple treatments—radiation, chemotherapy, and immunotherapy—which result in tumor adaptation responses and selection processes; cancer cell lines are unlikely to accurately model the nuances of these adaptive processes in an artificial setting because they lack the necessary interacting systems (e.g., the immune system, stroma, etc.). As such, even though cancer cell lines are valuable models for oncological research, not all aspects of the disease are fully recapitulated with their use.

Late-state, metastatic breast cancer patients often present with malignant pleural effusions, a collection of fluid between the parietal and visceral layers of the pleurae. The accumulation of fluid in the pleural space prevents the full expansion of the lung and results in difficult, shallow breathing. More than 75% of malignant pleural effusions occur in conjunction with lung, breast, or ovarian cancers or lymphoma; the debilitating disease complication can result from permeation of the pleural space to interstitial fluid, blocked lymphatic drainage, or inflammation (8, 9). With malignant pleural effusions, cancer cells that have metastasized from the primary tumor can reside in this fluid in suspension, or near-suspension, and continue to proliferate (10). As part of a palliative care effort, a thoracentesis can be performed to drain the fluid from the pleural space in order to ease respiratory discomfort; this process is not curative though, and continued, gradual fluid accumulation necessitates multiple medical interventions. Unfortunately, malignant pleural effusions are disease complications associated with late-stage cancers and patient survival following diagnosis with the condition is generally less than four months (11).

The isolation of malignant pleural effusion (PE) cells from patient thoracenteses provides a valuable opportunity to study metastatic and late-stage forms of breast cancer in a manner that does not require patients to undergo additional medical procedures. The use of PE cells for oncological research has been reported by others but their use is not widespread, likely a result of limited patient access at many research institutes and an inability to significantly expand these cells *in vitro* (12-15). Previously, our group reported the results of a study wherein we characterized the molecular and phenotypic features of PE cells and measured their sensitivity to different chemotherapeutics (16). Briefly, PE cells were obtained from consented breast cancer patients receiving treatment

at the Huntsman Cancer Hospital in collaboration with the Biorepository and Molecular Pathology group at the Huntsman Cancer Institute. Following their isolation from the drained pleural effusion fluid, these cells were frozen and stored in aliquots for research use; as such, the isolated PE cells could be minimally passaged *in vitro* with the goal of reducing their exposure to artificial culture environments that might alter their molecular characteristics over time. Experiments conducted with Dr. Keith Gligorich, a colleague at the Huntsman Cancer Institute, revealed that the isolated PE cells were not only heterogeneous in nature, but also had dramatically reduced proliferation rates compared to commonly used breast cancer cell lines (Figures 2.1 and 2.2). Additionally, these cells varied in their sensitivity to *in vitro* chemotherapeutic treatments, likely resulting from the different treatment histories of the patients from whom they were derived (Figure 2.3). In all, patient-derived malignant PE cells were found to recapitulate aspects of the disease not represented by breast cancer cell lines and permitted for the development of an *in vitro* model of chemoresistant, late-stage breast cancer. Herein, the results of a small molecule screen utilizing these patient-derived cells are discussed. These experiments have resulted in the identification of novel small molecules with anticancer properties that are active against metastatic, patient-derived tumor cells (16). The small molecules identified represent tools that can be used to further probe vulnerabilities of tumor cells and ultimately inform new strategies for therapeutic development.

Results

In an effort to explore and better understand the characteristics of drug-insensitive breast cancer cells, a small molecule screen was initiated with two aims in mind: 1)

Figure 2.1. Patient-derived malignant pleural effusion (PE) cells are heterogeneous in nature. Short-term culture of PE cells does not alter the cellular composition of the total population. PE1007070, PE1008032, and PE904557a (PE cell samples derived from three individual drug refractory breast cancer patients) were stained with markers for luminal and basal mammary epithelial cells, Keratin 8 and Keratin 14, respectively.

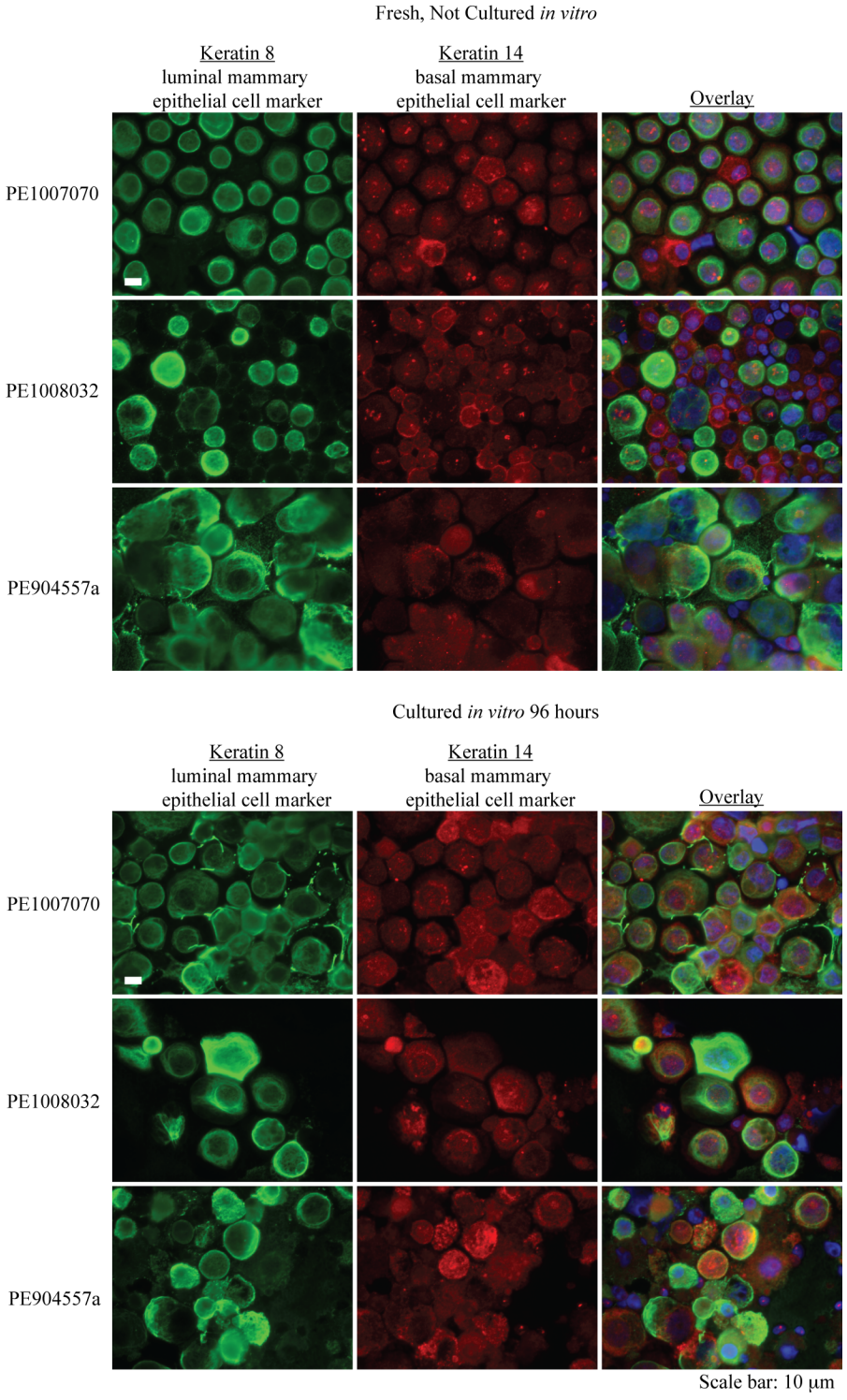
Fresh, Not Cultured *in vitro*
Keratin 8
luminal mammary
epithelial cell marker
Keratin 14
basal mammary
epithelial cell marker
Overlay
PE1007070
PE1008032
PE904557a
Cultured *in vitro* 96 hours
Keratin 8
luminal mammary
epithelial cell marker
Keratin 14
basal mammary
epithelial cell marker
Overlay
PE1007070
PE1008032
PE904557a
Scale bar: 10 µm

Figure 2.2. Malignant pleural effusion cells derived from breast cancer patients have reduced proliferation rates compared to breast cancer cell lines. Cells were cultured with either bromodeoxyuridine (BrdU) or 5-ethynyl-2'-deoxyuridine (EdU) for 30 minutes or 6 hours; subsequently, genomic incorporation of the nucleoside analog was measured by flow cytometry as a measure of cellular proliferation. The following cell types were evaluated: untransformed cell types- MCF-10A (mammary epithelial cell line) and hTERT-HMEC (immortalized primary human mammary epithelial cells); malignant cell lines- MCF-7, T47D, and MDA-MB-231; patient-derived malignant pleural effusion cells- PE1007070, PE1008032, and PE904557a.

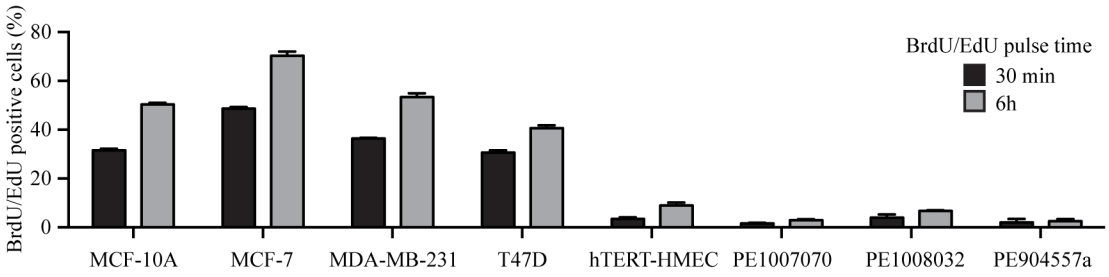
BrdU/EdU positive cells (%)
80
60
40
20
0
BrdU/EdU pulse time
30 min
6h
MCF-10A
MCF-7
MDA-MB-231
T47D
hTERT-HMEC
PE1007070
PE1008032
PE904557a

Figure 2.3. Patient-derived malignant pleural effusion cells obtained from breast cancer patients that have developed drug refractory disease display altered responses to chemotherapeutics *in vitro*. Cells were treated with each chemotherapeutic for four days; cell viability was then measured by assessing cellular ATP content. Values plotted represent the mean and standard deviation of three replicates. Breast cancer cell lines evaluated: MCF-7, T47D, MDA-MB-231. Patient-derived malignant pleural effusion cells evaluated: PE1007070, PE1008032, PE904557a.

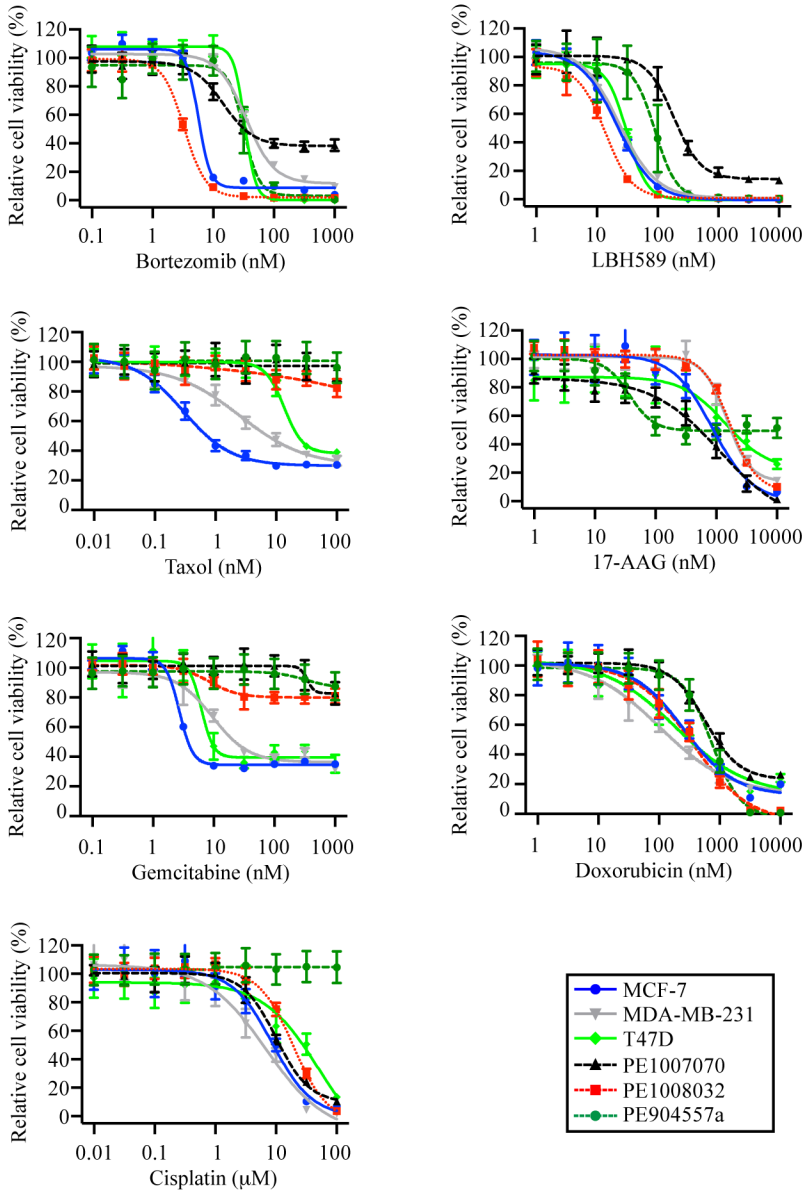
Relative cell viability (%)
120
100
80
60
40
20
0
0.1
1
10
100
1000
Bortezomib (nM)
1
10
100
1000
10000
LBH589 (nM)
0.01
0.1
1
10
100
Taxol (nM)
17-AAG (nM)
Gemcitabine (nM)
Doxorubicin (nM)
Cisplatin (μM)
MCF-7
MDA-MB-231
T47D
PE1007070
PE1008032
PE904557a

identify small molecule modulators of biological pathways specific to tumor cells and 2) use these small molecules to define vulnerabilities existing in drug-insensitive cells. First, a screening system was designed to allow for the identification of cancer-selective phenotypes; immortalized human mammary epithelial cells (hTERT-HMECs) were chosen to represent nontumorigenic cells and PE cells obtained from a single patient were chosen to represent tumor cells in the screen. Upon selecting cell types appropriate for the experiment, a library of small molecules was chosen; we sought to employ molecules previously untested in biological systems as a means to identify scaffolds with novel biological modes of action. As such, a library of 560 novel compounds containing a variety of chemical scaffolds was chosen. The compounds originated from different labs within the University of Utah Department of Chemistry and a variety of chemical space was represented (Figure 2.4). Importantly, most compounds could be synthesized in significant quantities, permitting for follow-up *in vitro* and *in vivo* studies to be conducted without regard for compound scarcity.

Employing both hTERT-HMECs and PE cells, a four-day treatment assay with the 560-small molecule library was conducted by Dr. Keith Gligorich using a 20 μM concentration of each small molecule; following the conclusion of treatment, cell viability was assessed by quantifying cellular ATP-content and comparing control- and small molecule-treated conditions. Then, using these measurements, hTERT-HMEC viability was compared to PE cell viability and an assessment of each small molecule's cancer-selective cytotoxicity was conducted (Figure 2.5). Selecting an arbitrary cut-off, the fourteen molecules with the highest degree of cancer-selectivity, representing 2.5% of the total library, were chosen for follow-up studies. In the follow-up studies, hTERT-

Figure 2.4. Examples of the chemical scaffolds found within the small molecule library. The small molecule library developed by the University of Utah Department of Chemistry was comprised of diverse chemical scaffolds and represented a variety of chemical space.

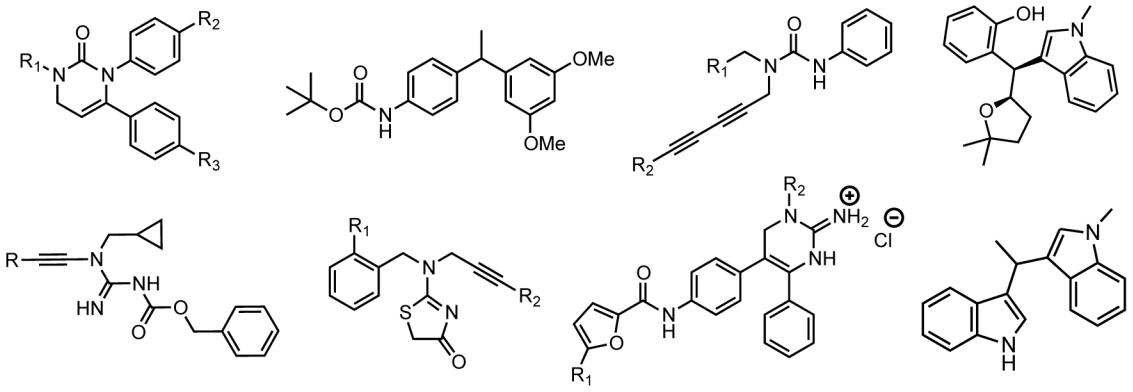

Figure 2.5. Results of a small molecule library screen conducted using untransformed mammary epithelial cells (hTERT-HMECs) and patient-derived malignant pleural effusion cells (PE1007070). Results are plotted as a difference in cell viability between hTERT-HMEC and PE1007070 cells as a measure of small molecule's cytotoxic cancer-selectivity. An arbitrary threshold (hit limit) was chosen to assess the most cancer-selective small molecules. The screen was conducted by Dr. Keith Gligorich.

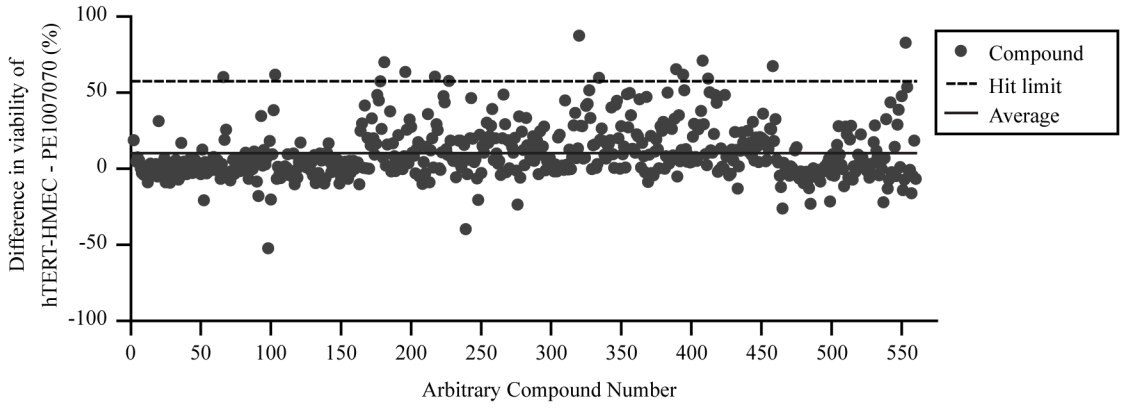
Difference in viability of
hTERT-HMEC - PE1007070 (%)
100
50
0
-50
-100
0
50
100
150
200
250
300
350
400
450
500
550
Arbitrary Compound Number
Compound
Hit limit
Average

HMEC and PE cells were tested against a 12-point concentration range of the small molecules, instead of a single concentration, and EC_{50} values were calculated to better assess small molecule activity (Figure 2.6). Collectively, the follow-up studies revealed a variety of dose response profiles, both in potency and in the degree of cancer-specific cytotoxicity, suggesting that the small molecule panel modulates diverse biological pathways.

Discussion

Models of breast cancer that accurately represent the human disease are indispensable for biomedical research aimed at improving patient survival outcomes. *In vitro* and *in vivo* models contribute directly to our understanding of breast cancer's molecular characteristics, genomic plasticity, interactions with host systems, and responses to treatment. Breast cancer cell lines are ubiquitously employed as *in vitro* models of the disease and are excellent tools for the study of cell autonomous signaling pathways in cancer. However, not all aspects of the disease found in patients are reflected in their use; compared to the primary breast tumor, cell lines are homogeneous in nature, have increased proliferation rates, and fail to model changes that occur over the course of patient treatment. Considering these shortcomings, we chose to implement a preclinical model that uses patient-derived breast cancer cells for our investigations into the nature of late-stage, drug-insensitive cancers. The cells used were derived from the malignant pleural effusions of breast cancer patients undergoing clinical treatment at the Huntsman Cancer Hospital. Characterization studies revealed that the malignant PE cells were not only heterogeneous with regard to the types of tumor cells present, but they

Figure 2.6. Results of follow-up studies examining the efficacies of fourteen molecules identified from the small molecule screen. Twelve-point dose response analyses were used to measure the effects of the small molecules on the cell viabilities of untransformed mammary epithelial cells (hTERT-HMEC) and patient-derived malignant pleural effusion cells (PE1007070); experiment was performed by Dr. Keith Gligorich. Cells were treated with small molecules from the screen for four days then viability was measured by assessing cellular ATP content. Values plotted represent the mean and standard deviation of three replicates.

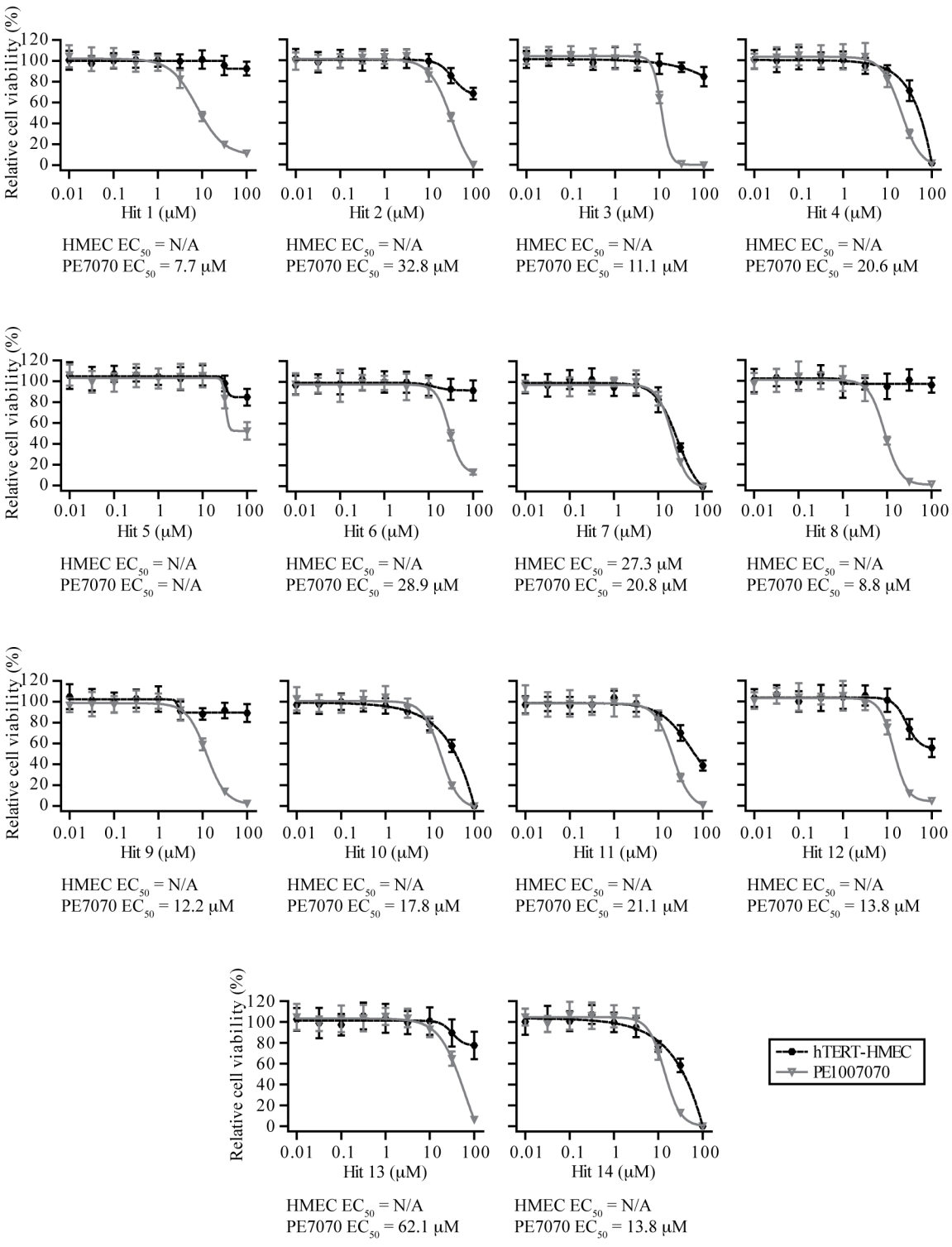
Relative cell viability (%)
120
100
80
60
40
20
0
0.01 0.1 1 10 100
Hit 1 (μM)
HMEC EC50 = N/A
PE7070 EC50 = 7.7 μM
Hit 2 (μM)
HMEC EC50 = N/A
PE7070 EC50 = 32.8 μM
Hit 3 (μM)
HMEC EC50 = N/A
PE7070 EC50 = 11.1 μM
Hit 4 (μM)
HMEC EC50 = N/A
PE7070 EC50 = 20.6 μM
Hit 5 (μM)
HMEC EC50 = N/A
PE7070 EC50 = N/A
Hit 6 (μM)
HMEC EC50 = N/A
PE7070 EC50 = 28.9 μM
Hit 7 (μM)
HMEC EC50 = 27.3 μM
PE7070 EC50 = 20.8 μM
Hit 8 (μM)
HMEC EC50 = N/A
PE7070 EC50 = 8.8 μM
Hit 9 (μM)
HMEC EC50 = N/A
PE7070 EC50 = 12.2 μM
Hit 10 (μM)
HMEC EC50 = N/A
PE7070 EC50 = 17.8 μM
Hit 11 (μM)
HMEC EC50 = N/A
PE7070 EC50 = 21.1 μM
Hit 12 (μM)
HMEC EC50 = N/A
PE7070 EC50 = 13.8 μM
Hit 13 (μM)
HMEC EC50 = N/A
PE7070 EC50 = 62.1 μM
Hit 14 (μM)
HMEC EC50 = N/A
PE7070 EC50 = 13.8 μM
hTERT-HMEC
PE1007070

more closely matched the proliferation rates of tumors in patients and they also varied in their responses to *in vitro* drug treatment, variations likely resulting from patients' adaptive responses to clinical treatment. Together, these features suggested that the patient-derived PE cells could provide clinically relevant insight into the disease where cell lines would fall short.

With the overall goals of advancing our general understanding of chemoresistance and identifying vulnerabilities of drug resistant cells that can be targeted therapeutically, a small molecule screen, together with hTERT-HMECs and patient-derived PE cells, was implemented as a means to identify chemical modulators of tumor-specific pathways. Small molecules identified from the screen could then be used as tools to elucidate mechanistic pathways, define new modes of drug-induced tumor cell death, and explore new strategies for treatment design and development. Using a library of compounds synthesized at the University of Utah Department of Chemistry, the two cell types were tested against the library and small molecules that resulted in cell death in tumor cells, but not in untransformed mammary epithelial cells, were used for follow-up studies. In all, fourteen compounds were chosen for more detailed dose response analysis studies. These small molecules were found to induce cytotoxic effects in tumor cells at varied, low micromolar efficacies and produced diverse selectivity profiles, suggesting that the different chemical scaffolds modulated a variety of biological pathways. This encouraging result hints at the existence of multiple, drug-targetable vulnerabilities and extends an optimistic outlook for future therapeutic drug design.

In all, the incorporation of patient-derived malignant PE cells into the experimental design allowed for relevant, focused results to be obtained; while it would have been possible to identify small molecules with cytotoxic, cancer selective

phenotypes using breast cancer cell lines as a model, it is unlikely that all of the resultant molecules would be active in cells with altered drug sensitivities and naturally slower proliferation rates. As such, this study highlights the benefits of using a breast cancer model that closely recapitulates the disease state in patients.

Methods

Detailed descriptions of the materials and methods used for the study presented herein have been reported previously (16).

References

1. Howlader N*, et al.* (2013) SEER Cancer Statistics Review, 1975-2010. *National Cancer Institute*, Bethesda, MD.

2. Burdall S, Hanby A, Lansdown M, & Speirs V (2003) Breast cancer cell lines: friend or foe? *Breast Cancer Res* 5(2):89 - 95.

3. Holliday D & Speirs V (2011) Choosing the right cell line for breast cancer research. *Breast Cancer Res* 13(4):215.

4. Keller P*, et al.* (2010) Mapping the cellular and molecular heterogeneity of normal and malignant breast tissues and cultured cell lines. *Breast Cancer Res* 12(5):R87.

5. Stingl J & Caldas C (2007) Molecular heterogeneity of breast carcinomas and the cancer stem cell hypothesis. *Nat Rev Cancer* 7(10):791-799.

6. Remvikos Y*, et al.* (1991) Breast cancer proliferation measured on cytological samples: a study by flow cytometry of S-phase fractions and BrdU incorporation. *Br J Cancer* 64(3):501-507.

7. Ross DT*, et al.* (2000) Systematic variation in gene expression patterns in human cancer cell lines. *Nat Genet* 24(3):227-235.

8. Heffner JE (2008) Diagnosis and management of malignant pleural effusions. *Respirology* 13(1):5-20.

9. Marazioti A & Stathopoulos GT (2013) Malignant pleural effusion. *Experimental Metastasis: Modeling and Analysis*, ed Malek A (Springer, Netherlands), pp 163-187.

10. Johnston WW (1985) The malignant pleural effusion. A review of cytopathologic diagnoses of 584 specimens from 472 consecutive patients. *Cancer* 56(4):905-909.

11. Burrows CM, Mathews WC, & Colt HG (2000) Predicting survival in patients with recurrent symptomatic malignant pleural effusions: an assessment of the prognostic values of physiologic, morphologic, and quality of life measures of extent of disease. *Chest* 117(1):73-78.

12. Lin C-C*, et al.* (2011) Malignant pleural effusion cells show aberrant glucose metabolism gene expression. *Eur Respir J* 37(6):1453-1465.

13. Jian G*, et al.* (2010) Prediction of epidermal growth factor receptor mutations in the plasma/pleural effusion to efficacy of gefitinib treatment in advanced non-small cell lung cancer. *J Cancer Res Clin Oncol* 136(9):1341-1347.

14. Ye Z-J*, et al.* (2010) Generation and differentiation of IL-17–producing CD4+ T cells in malignant pleural effusion. *J Immunol* 185(10):6348-6354.

15. Szulkin A*, et al.* (2014) Characterization and drug sensitivity profiling of primary malignant mesothelioma cells from pleural effusions. *BMC Cancer* 14(1):709.

16. Gligorich K*, et al.* (2013) Development of a screen to identify selective small molecules active against patient-derived metastatic and chemoresistant breast cancer cells. *Breast Cancer Res* 15(4):R58.

CHAPTER 3

THE SMALL MOLECULE C-6 PROMOTES CANCER-SELECTIVE CELL DEATH VIA A CASPASE INDEPENDENT MECHANISM

Results of the studies presented herein have been previously published: Gligorich KM, Vaden RM, *et al.* (2013) Development of a screen to identify selective small molecules active against patient-derived metastatic and chemoresistant breast cancer cells. *Breast Cancer Res* 15(4):R58 and Vaden RM, Gligorich KM, Jana R, Sigman MS, & Welm BE (2014) The small molecule C-6 is selectively cytotoxic against breast cancer cells and its biological action is characterized by mitochondrial defects and endoplasmic reticulum stress. *Breast Cancer Res* (DOI: 10.1186/s13058-014-0472-0).

Abstract

Our limited understanding of the molecular processes of drug insensitive neoplastic cells has posed a significant challenge for the development of new treatment strategies. Small molecules that elicit desired phenotypes can be used as molecular tools to probe and define biological systems. We previously reported the identification of the small molecule C-6, which induces cytotoxic and cytostatic phenotypes in drug refractory tumor cells. Using this small molecule as a chemical tool, studies were conducted to characterize the cellular pathways affected in an effort to identify dependencies and vulnerabilities of advanced stage cancers. These studies revealed that C-6 induces cancer cell death via a caspase independent mechanism. Additionally, the small molecule induces endoplasmic reticulum stress and alters mitochondrial morphology and function. Alterations in energetic homeostasis and metabolic profiles were also observed. In all, these studies suggest that pharmacologic induction of mitochondrial and endoplasmic reticulum stress may be a useful strategy for the treatment of advanced stage cancers.

Introduction

The application of chemical tools to the study of biological systems has added significantly to our knowledge of molecular biology, cellular signaling, and disease states. Well-known examples of molecules that have directly contributed to our understanding of cell systems include rapamycin, colchicine, and pioglitazone; these chemical tools have allowed scientists to elucidate mechanisms of cellular nutrient sensing, microtubule polymerization, and glucose metabolism and adipogenesis, respectively (1-4). Previously, we reported the development of a chemical screen that

utilized malignant pleural effusion cells as a model of advanced stage cancer; these aggressive metastatic cells were derived from breast cancer patients whose disease had become resistant to treatment (5). The screen was conducted with the purpose of identifying biologically active small molecules that could be used as tools to elucidate cellular mechanisms of advanced stage cancers and drug resistance; in all, fourteen molecules were identified for their cytotoxic, cancer-selective phenotypes. Herein are described the results of mode of action studies conducted with C-6, one of the small molecules identified. With the overall goal of uncovering vulnerabilities of chemoresistant tumor cells that can be targeted therapeutically, these experiments have provided insight into the nature of drug insensitive cancers.

Results

The small molecule C-6 selectively affects cancer cells

Previously, we reported the identification of a novel diarylmethine-containing small molecule, C-6, for its biological activity against patient-derived malignant pleural effusion cells. Additionally, while the molecule was found to reduce the viability of three different patient-derived tumor cell types, it did not significantly affect untransformed mammary epithelial cells (Figure 3.1A and 3.1B) (5). Considering the paucity of patient-derived malignant pleural effusion cells and the inherent limitations associated with their expansion in culture, we sought to identify additional models of breast cancer with which to conduct mechanistic studies; the additional models could also be used to assess the generality of C-6's mode of action. Turning to breast cancer cell lines, MCF-7, T47D, and MDA-MB-231 cells were evaluated for their sensitivity to C-6 using twelve-

Figure 3.1. The small molecule C-6 is selectively cytotoxic against tumor cells. (A) The small molecule C-6. (B) Twelve-point dose response analyses of untransformed primary mammary epithelial cells (hTERT-HMECs) and three patient-derived malignant pleural effusion cells (PE1007070, PE1008032, and PE904557a) treated with C-6 for four days. (C) 12-point dose response analyses of an untransformed primary mammary epithelial cell line (MCF-10A) and three breast cancer cell lines (MCF-7, T47D, and MDA-MB-231) treated with C-6 for five days.

A

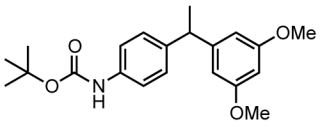

C-6

B

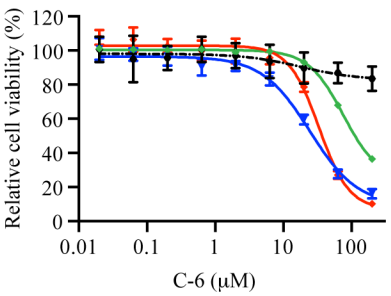

Cell Type	C-6 EC_{50}
hTERT-HMEC	N/A
PE1007070	24.4 μM
PE1008032	33.3 μM
PE904557a	75.7 μM

C

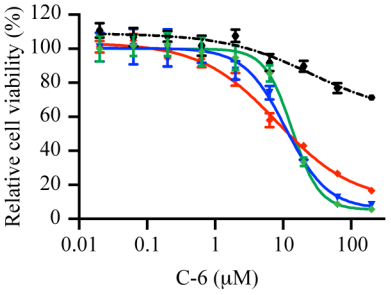

Cell Type	C-6 EC_{50}
MCF-10A	N/A
MCF-7	11.0 μM
MDA-MB-231	10.5 μM
T47D	8.29 μM

point dose response analyses to assess the effect of the small molecule on cell viability. Opportunely, C-6 was found to affect each of the three cell types examined and the EC_{50} values were comparable to the low micromolar efficacies observed with patient-derived cells (Figure 3.1C). To further assess whether breast cancer cell lines might be used to complement patient-derived cells in mode of action studies, an untransformed mammary epithelial cell line (MCF-10A) was also tested against C-6. As with the primary cells, C-6's activity was restricted largely to transformed cells and MCF-10A cells were only minimally affected, even at the highest concentrations tested. Collectively, the low micromolar efficacy and selectivity for untransformed cell lines suggested that cell lines could be used reliably for mechanistic studies aimed at better understanding the basis for C-6's biological activity.

C-6 induces cell cycle arrest and caspase independent cell death in cancer cells

As a first approach towards elucidating mechanisms contributing to C-6's ability to reduce tumor cell viability, experiments were conducted to probe the effect of the small molecule on cell cycle; alterations in cell cycle progression can be informative of a molecule's mode of action if blocks occur in specific phases (e.g., mitosis). Three breast cancer cell lines and one untransformed mammary epithelial cell line were treated with C-6 for either 24 or 48 hours. Following the conclusion of treatment, the cells were incubated with a nucleoside analog (BrdU, bromodeoxyuridine), which is incorporated into newly synthesized DNA (6). The incorporation, which is proportional to the degree of cellular proliferation, can be quantified by flow cytometry and further analyzed to

determine phases of the cell cycle present within the overall population. The results of these experiments conducted by a colleague, Dr. Keith Gligorich, revealed that treatment with C-6 significantly reduced proliferation of breast cancer cells; untransformed mammary epithelial cells also experienced a reduction in proliferation but the change was not statistically significant (Figure 3.2). Analysis of the cell cycle profile (i.e., S phase, G_1/G_0 phase, G_2 phase, and mitosis) revealed that treatment with the small molecule resulted in an accumulation of cells in G_1/G_0 phase accompanied by a reduction of cells in S phase, again, an effect observed only in malignant cells. In all, these initial studies further demonstrated the preferential nature of C-6's effect on tumor cells and provided evidence to suggest that C-6 treatment inhibits progression from G_1/G_0 to S phase of the cell cycle in malignant cells.

Based on the results of the cell cycle analyses, follow-up experiments were designed to probe whether C-6 induced cytostatic phenotypes exclusively or if the small molecule also induced cell death since dose response analyses alone cannot differentiate between cytotoxic- and cytostatic-induced reductions in cell viability. To assess cytotoxic characteristics, an AAF-Glo assay was employed; the assay can measure the total number of cells as well as the number of dead cells simultaneously and can therefore be used to assess cytotoxicity. Examining both cell lines and patient-derived malignant pleural effusion cells, C-6 was found to elicit a cytotoxic phenotype in MCF-7, PE1007070, PE904557a, and PE1100025 cells and a cytostatic phenotype in MDA-MB-231 and PE1008032 cells, suggesting that the observed reductions in cell viability could occur by either mechanism and were likely cell-type dependent (Figure 3.3). Interestingly, evidence has been presented to suggest that cytostatic effects can be as important as cytotoxic effects for the overall success of anticancer agents (7).

Figure 3.2. C-6-treatment alters cell cycle progression in tumor cells, but not untransformed cells. A mammary epithelial cell line (MCF-10A) and three breast cancer cell lines (MCF-7, T47D, and MDA-MB-231) were treated with C-6 for either 24 or 48 hours. Relative proliferation was then assessed by measuring bromodeoxyuridine (BrdU) incorporation by flow cytometry. Statistical significance (p-value ≤ 0.05) is annotated with an asterisk.

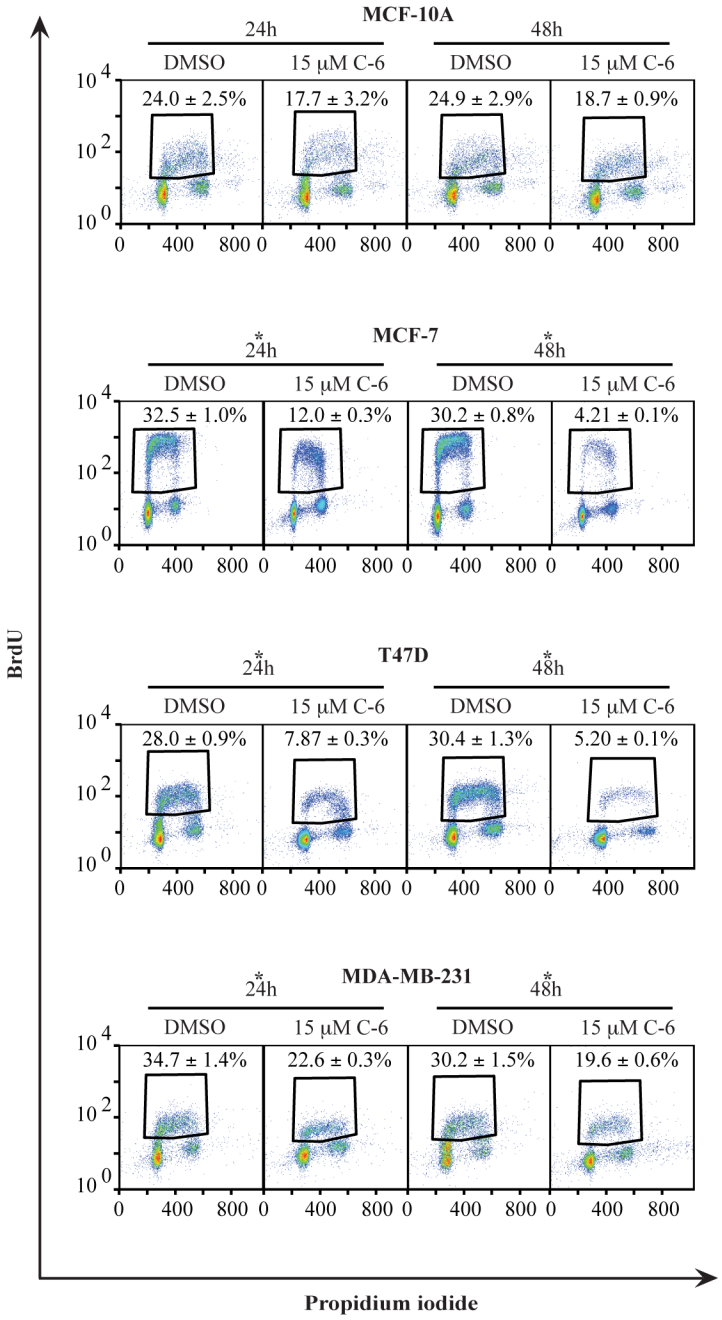
MCF-10A
24h
48h
DMSO
15 μM C-6
DMSO
15 μM C-6
24.0 ± 2.5%
17.7 ± 3.2%
24.9 ± 2.9%
18.7 ± 0.9%
MCF-7
*24h
*48h
DMSO
15 μM C-6
DMSO
15 μM C-6
32.5 ± 1.0%
12.0 ± 0.3%
30.2 ± 0.8%
4.21 ± 0.1%
T47D
*24h
*48h
DMSO
15 μM C-6
DMSO
15 μM C-6
28.0 ± 0.9%
7.87 ± 0.3%
30.4 ± 1.3%
5.20 ± 0.1%
MDA-MB-231
*24h
*48h
DMSO
15 μM C-6
DMSO
15 μM C-6
34.7 ± 1.4%
22.6 ± 0.3%
30.2 ± 1.5%
19.6 ± 0.6%
BrdU
Propidium iodide

Figure 3.3. C-6 promotes both cytotoxic and cytostatic phenotypes. Four patient-derived cell types and three cell lines were treated with C-6 for up to four-days in a time course study. The relative numbers of live and dead cells were quantified using an AAF-Glo assay. Values plotted represent the relative number of dead cells and are the average of three replicates. Error bars represent the standard deviation of the replicates measured. Statistical significance (p-value ≤ 0.05) is annotated with an asterisk.

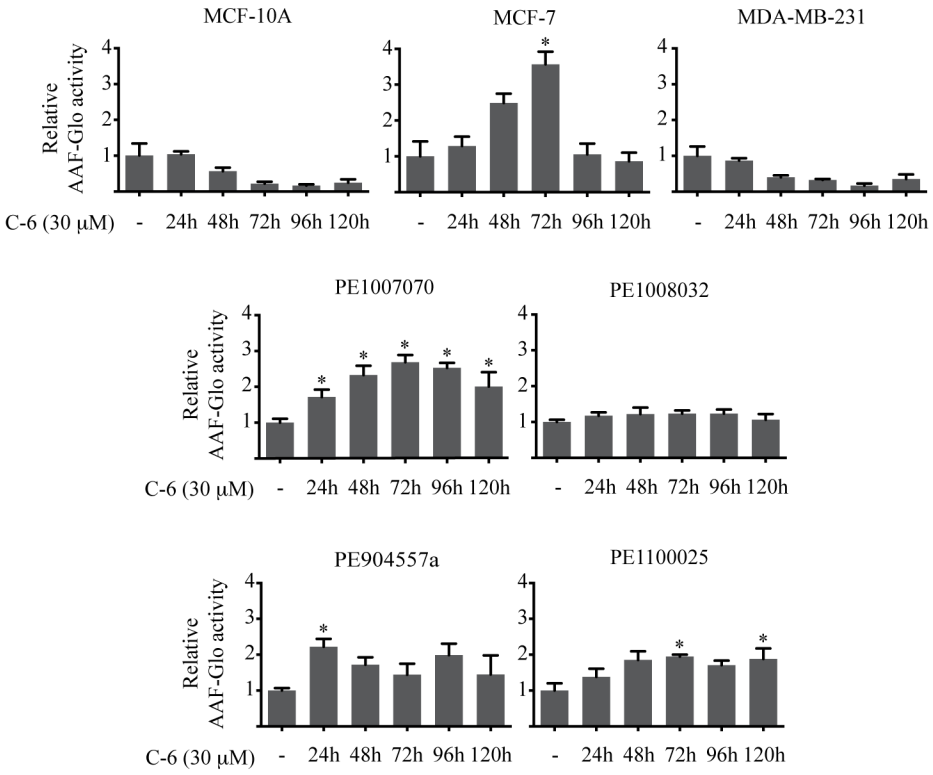
MCF-10A
MCF-7
MDA-MB-231
Relative AAF-Glo activity
C-6 (30 μM) - 24h 48h 72h 96h 120h
PE1007070
PE1008032
PE904557a
PE1100025

Furthermore, that C-6 induced cytostasis is followed by delayed cell death cannot be excluded as a mechanism of reduction in cell viability.

Upon observing that C-6 was capable of inducing cancer cell death, additional experiments were conducted as to determine whether cell death was accompanied by caspase activation. Caspases participate in signaling cascades directly involved in apoptosis and their contribution to programmed cell death has been well characterized (reviewed in (8)). Two methods were used to measure caspase activity: immunoblot and enzymatic Caspase-Glo assays. Surprisingly, treatment of malignant pleural effusion cells and cell lines with C-6 revealed that the small molecule did not induce activation of caspases 3/7, 8, or 9 as compared to positive control-treated cells in either the immunoblot or the Caspase-Glo assays (Figure 3.4A and 3.4B). These results suggest that the form of cell death induced by C-6 is not mediated by classic apoptotic signaling mechanisms.

Considering other forms of cell death not mediated by caspases, we next sought to assess whether autophagy could be participating in the determination of cancer cell fate following treatment with the small molecule. Autophagy describes a process of self-degradation wherein cells can "recycle" intracellular components, which can help balance overall cellular energy levels (reviewed in (9)). Intracellular components destined for degradation can be sequestered into double membrane-bound autophagosomes for decomposition by hydrolytic enzymes. Microtubule-associated protein 1A/1B-light chain 3-II (LC3-II), following its conversion from LC3-I via protein lipidation, is then recruited to the autophagosome membrane to facilitate additional autophagic processes (10). As such, changes in LC3-II can be monitored via immunoblot experiments to assess cellular activation of autophagy. Patient-derived malignant pleural effusion cells and cell lines

Figure 3.4. Treatment with C-6 does not stimulate caspase activity. (A) Immunoblot analysis of PARP cleavage and caspases 3, 8, and 9 protein levels in cells treated with C-6 for 48 hours. Staurosporine and trail/doxorubicin were used as positive control treatment conditions; vinculin was used as a loading control. Experiment was conducted in collaboration with Dr. Keith Gligorich. (B) Measurement of enzymatic caspase activity in cells treated with C-6. Staurosporine was used as a positive control. Values plotted represent the average of three replicates; error bars represent the standard deviation of the replicates measured. Statistical significance (p-value ≤ 0.05) is annotated with an asterisk.

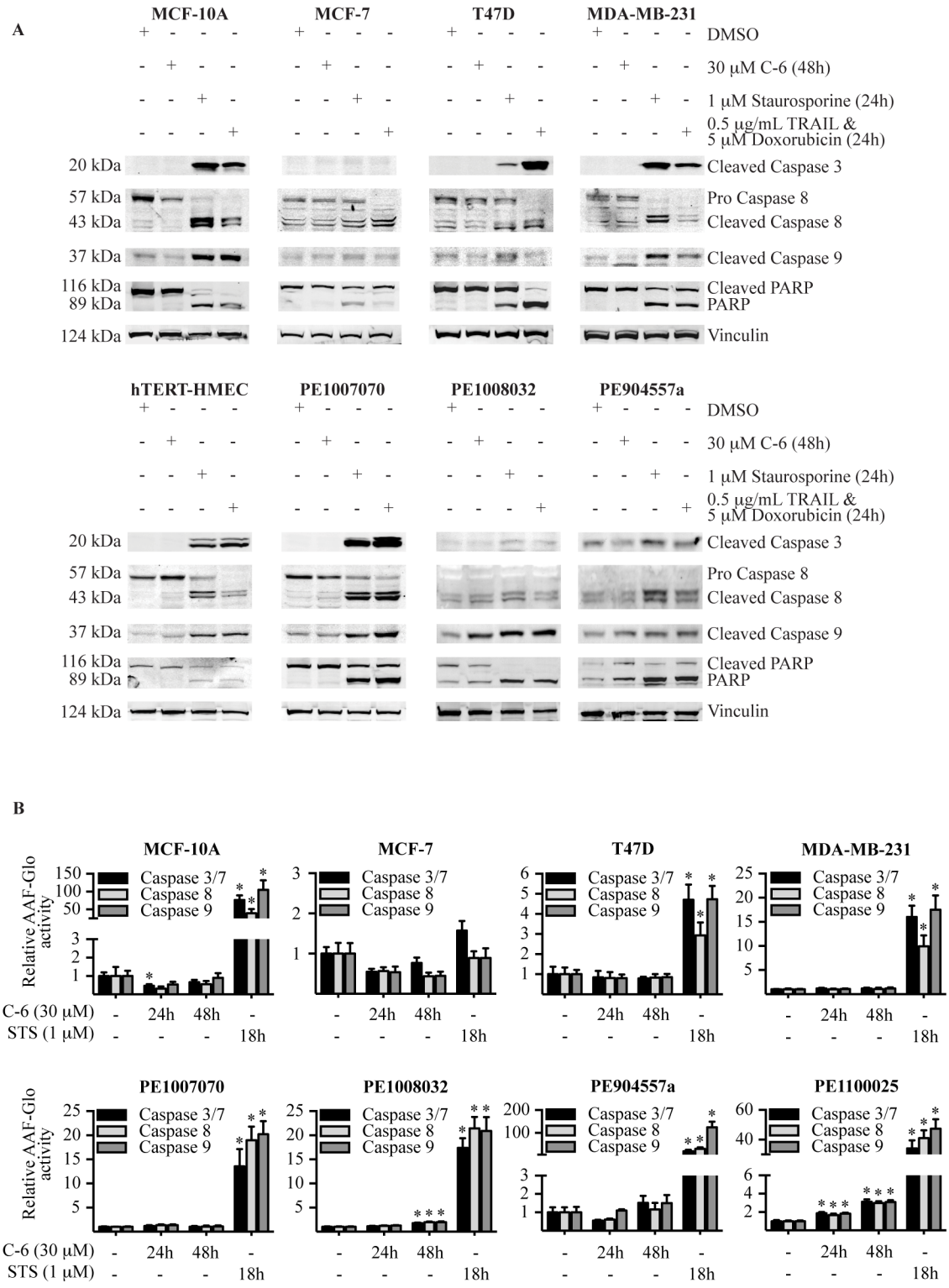
A
MCF-10A
MCF-7
T47D
MDA-MB-231
DMSO
30 μM C-6 (48h)
1 μM Staurosporine (24h)
0.5 μg/mL TRAIL & 5 μM Doxorubicin (24h)
20 kDa
Cleaved Caspase 3
57 kDa
43 kDa
Pro Caspase 8
Cleaved Caspase 8
37 kDa
Cleaved Caspase 9
116 kDa
89 kDa
Cleaved PARP
PARP
124 kDa
Vinculin
hTERT-HMEC
PE1007070
PE1008032
PE904557a
B
MCF-10A
MCF-7
T47D
MDA-MB-231
PE1007070
PE1008032
PE904557a
PE1100025
Relative AAF-Glo activity
Caspase 3/7
Caspase 8
Caspase 9
C-6 (30 μM)
STS (1 μM)
24h
48h
18h

were treated with either C-6 or a positive control, chloroquine; in conjunction with a colleague, Dr. Keith Gligorich, immunoblot assays were then conducted to monitor changes induced in LC3-I and LC3-II protein levels. With the exception of T47D breast cancer cells, no changes were observed in the eight cell types tested; T47D cells presented with an unexpected increase in both LC3-I and LC3-II (Figure 3.5). This observation in T47D cells suggest that these cells respond to C-6 treatment by increasing the levels of LC3-I, either transcriptionally or by processing additional proLC3, and also that the autophagosome degradation may be inhibited, as evidenced by increased LC3-II. Collectively, the data suggest that C-6's biological activity against cancer cells is generally not dependent upon the activation of autophagy, although context-dependent activation of autophagy cannot be excluded.

Mitochondrial and endoplasmic reticulum stress are components of C-6's phenotype

In an effort to further elucidate C-6's mode of action in cancer cells, we next conducted a transcriptome profiling experiment to assess the effect of C-6 on gene transcription. MCF-7 breast cancer cells were treated with either C-6 for three hours; following treatment, RNA was isolated and purified before analysis by next generation sequencing. A differential expression analysis was then performed comparing C-6 treatment to control treatment. Interestingly, the results of the experiment revealed two key observations. First, of the most differentially expressed genes whose expression was increased in C-6-treated cells, seven of the top twenty genes were associated with endoplasmic reticulum (ER) stress. Second, of the most differentially expressed genes

Figure 3.5. Activation of the autophagosome marker LC3 is not compulsory for C-6's biological activity. Protein was isolated from cells treated with C-6 for 48 hours and an immunoblot assay was used to detect changes in LC3. The cytotoxic molecule staurosporine was used as a negative control and chloroquine was used as a positive control for the detection of LC3; α-tubulin was used as a loading control. Experiment was conducted in collaboration with Dr. Keith Gligorich

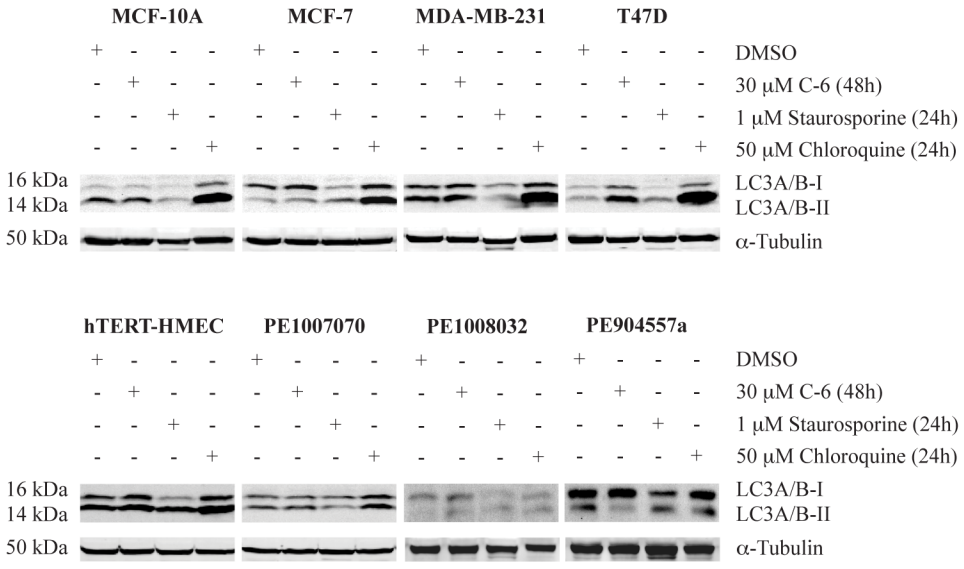
MCF-10A
MCF-7
MDA-MB-231
T47D
DMSO
30 μM C-6 (48h)
1 μM Staurosporine (24h)
50 μM Chloroquine (24h)
16 kDa
14 kDa
LC3A/B-I
LC3A/B-II
50 kDa
α-Tubulin
hTERT-HMEC
PE1007070
PE1008032
PE904557a
DMSO
30 μM C-6 (48h)
1 μM Staurosporine (24h)
50 μM Chloroquine (24h)
16 kDa
14 kDa
LC3A/B-I
LC3A/B-II
50 kDa
α-Tubulin

whose expression was decreased in C-6-treated cells, six of the top twenty genes were encoded by the mitochondrial genome (Figure 3.6A). Furthermore, nearly every gene encoded by the mitochondrial genome was decreased in expression, suggesting that C-6 induced broad perturbations in mitochondria.

Based on the results obtained from the next generation sequencing experiment, an investigation into the impact of ER stress on C-6 treated cells was conducted. In general, the ER stress response pathway can be activated during times of protein misfolding or accumulation following translation in the lumen of the ER. Some of the cellular mechanisms used to abate ER stress include translation attenuation and increased expression of protein-folding chaperones (reviewed in (11)). In order to assess ER stress levels, proteins known to participate in ER stress were assayed by immunoblot using cell lines that had been treated with C-6; these experiments were conducted by a colleague, Dr. Keith Gligorich (Figure 3.6B). A marked increase in the expression of DDIT3 (CCAAT-enhancer-binding protein homologous protein, CHOP), a transcription factor whose expression is increased during times of ER stress, was observed in MCF-7 and T47D cells but not in MCF-10A or MDA-MB-231 cells (12). The expression of a protein-folding chaperone, GRP78, was increased in three breast cancer cell lines examined but not in a C-6 insensitive untransformed mammary epithelial cell line (13). Another protein involved in the ER stress response, EIF2α, was also assayed by immunoblotting; the phosphorylation of EIF2α is known to occur as part of a cellular response to ER stress (14). Collectively, the relative levels of phosphorylated EIF2α following C-6 treatment were found to occur variably between the cell lines examined and the interpretation of the these results were confounded partially by the high basal levels of phosphorylation observed in three of the cell types examined. Finally, changes

Figure 3.6. Endoplasmic reticulum (ER) stress is induced following C-6 treatment. (A) A next generation sequencing experiment was conducted in triplicate with MCF-7 cells treated with either 30 μM C-6 or DMSO as a vehicle control. The values plotted represent the results of a differential expression analysis between the two treatment groups; the twenty most up- and down-regulated genes are shown. (B) A panel of four proteins associated with the ER stress response was assayed by immunoblotting following a time course treatment of cells with C-6; vinculin was used as a positive control.

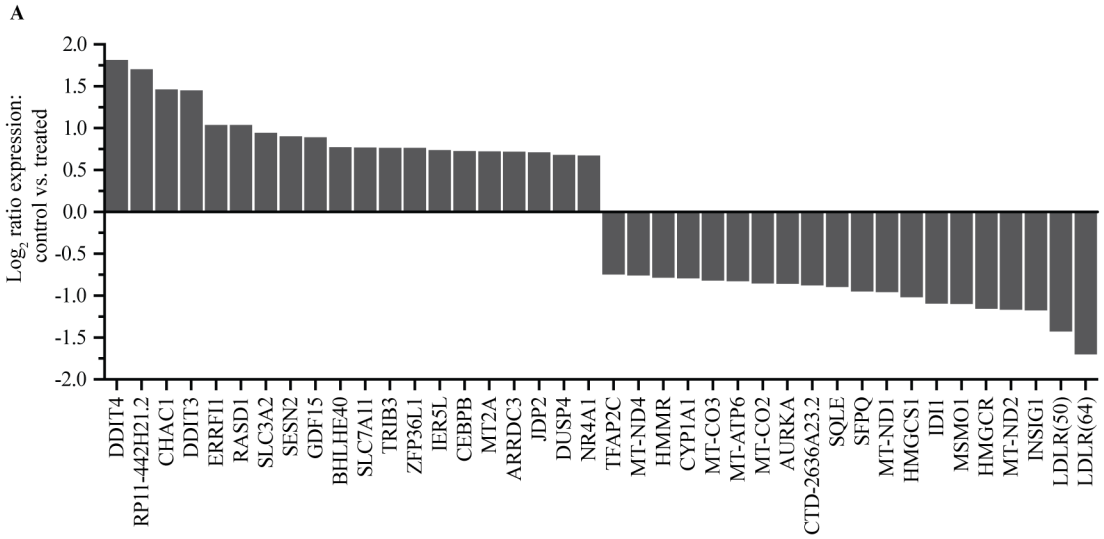
A
Log2 ratio expression: control vs. treated
2.0
1.5
1.0
0.5
0.0
-0.5
-1.0
-1.5
-2.0
DDIT4
RP11-442H21.2
CHAC1
DDIT3
ERRFI1
RASD1
SLC3A2
SESN2
GDF15
BHLHE40
SLC7A11
TRIB3
ZFP36L1
IER5L
CEBPB
MT2A
ARRDC3
JDP2
DUSP4
NR4A1
TFAP2C
MT-ND4
HMMR
CYP1A1
MT-CO3
MT-ATP6
MT-CO2
AURKA
CTD-2636A23.2
SQLE
SFPQ
MT-ND1
HMGCS1
IDI1
MSMO1
HMGCR
MT-ND2
INSIG1
LDLR(50)
LDLR(64)

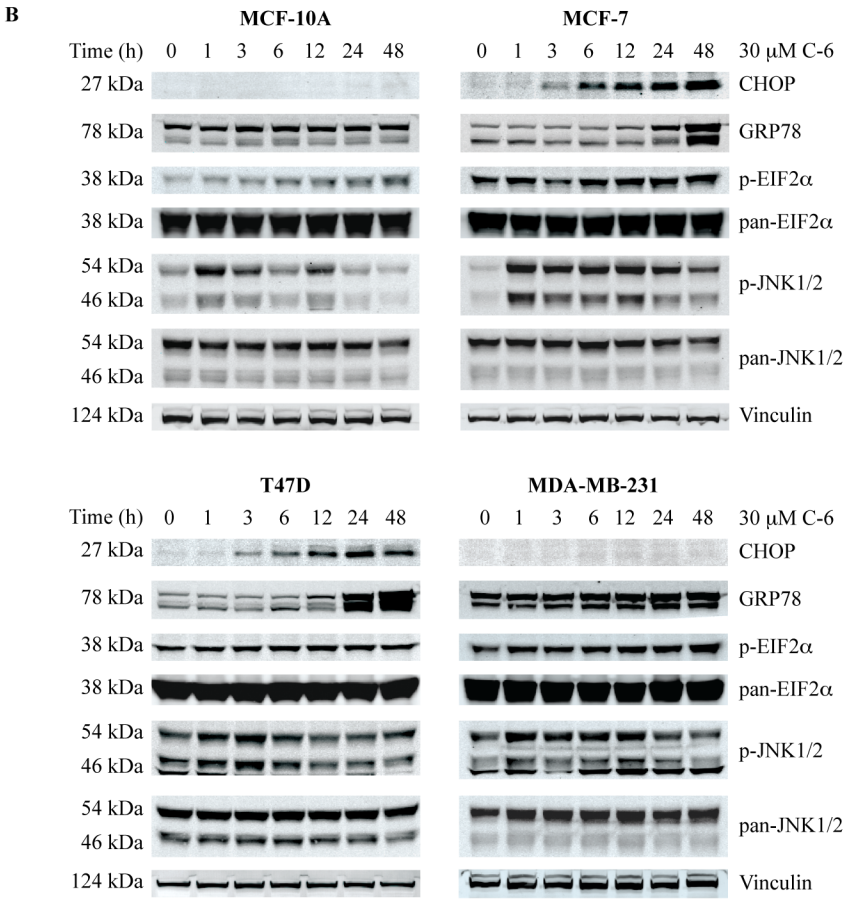
B
MCF-10A
MCF-7
Time (h) 0 1 3 6 12 24 48
0 1 3 6 12 24 48 30 μM C-6
27 kDa
CHOP
78 kDa
GRP78
38 kDa
p-EIF2α
38 kDa
pan-EIF2α
54 kDa
46 kDa
p-JNK1/2
54 kDa
46 kDa
pan-JNK1/2
124 kDa
Vinculin
T47D
MDA-MB-231
Time (h) 0 1 3 6 12 24 48
0 1 3 6 12 24 48 30 μM C-6
27 kDa
CHOP
78 kDa
GRP78
38 kDa
p-EIF2α
38 kDa
pan-EIF2α
54 kDa
46 kDa
p-JNK1/2
54 kDa
46 kDa
pan-JNK1/2
124 kDa
Vinculin

in the phosphorylation status of c-Jun Kinase (JNK) were evaluated following treatment it has been previously reported that activation of the JNK pathway during ER stress can potentiate cellular prodeath mechanisms (15-18). In all, every cell type tested presented with increased JNK phosphorylation following C-6-treatment although the kinetics of the expression varied over the course of the 48-hour treatment time course. Considering the sum of experiments conducted, ER stress is likely a general component of C-6's biological activity. However, the variable response magnitudes suggest that the degree of ER stress may be cell type-dependent.

C-6 treatment alters mitochondrial morphology

During the course of our studies to characterize C-6's mode of action, unique cytoplasmic vacuoles were frequently observed in cells treated with the small molecule. These features, however, were observed only in breast cancer cells and not in untransformed mammary epithelial cells. Cancer cells developed cytoplasmic vacuoles shortly after exposure to C-6 and these vacuoles expanded in size and number as exposure time increased (Figure 3.7A). In an effort to determine the origin and composition of these structures, transmission electron microscopy (TEM) imaging was conducted with MCF-7 breast cancer cells that had been treated with C-6; as a control, MCF-10A untransformed mammary epithelial cells were also included in the imaging experiment. Surprisingly, the acquired images revealed that the cytoplasmic vacuoles induced by C-6 in cancer cells were distended mitochondria (Figure 3.7B). Double-membrane mitochondria with gross morphological defects were observed in C-6-treated MCF-7 cells compared to a control while C-6-insensitive MCF-10A cells displayed no

Figure 3.7. C-6 treatment stimulates mitochondrial swelling and a subsequent vacuole phenotype in tumor cells but not untransformed cells. (A) An untransformed mammary epithelial cell line and two breast cancer cell lines were treated with 30 μM C-6; phase contrast images were acquired at 0, 12, and 24 hours to assess vacuole formation. Scale bar represents 10 μm; arrows denote cytoplasmic vacuoles. (B) Transmission electron microscopy images of C-6-treated cells reveal enlarged mitochondria in MCF-7 breast cancer cells, but not untransformed MCF-10A cells, treated with the small molecule. Cells were exposed to 30 μM C-6 for 24 hours before fixing and imaging.

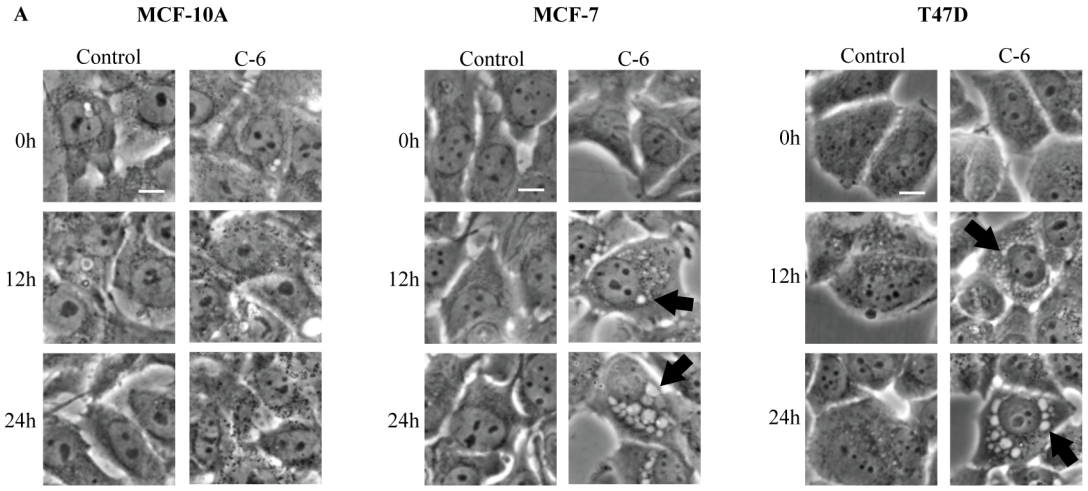
A
MCF-10A
MCF-7
T47D
Control
C-6
0h
12h
24h

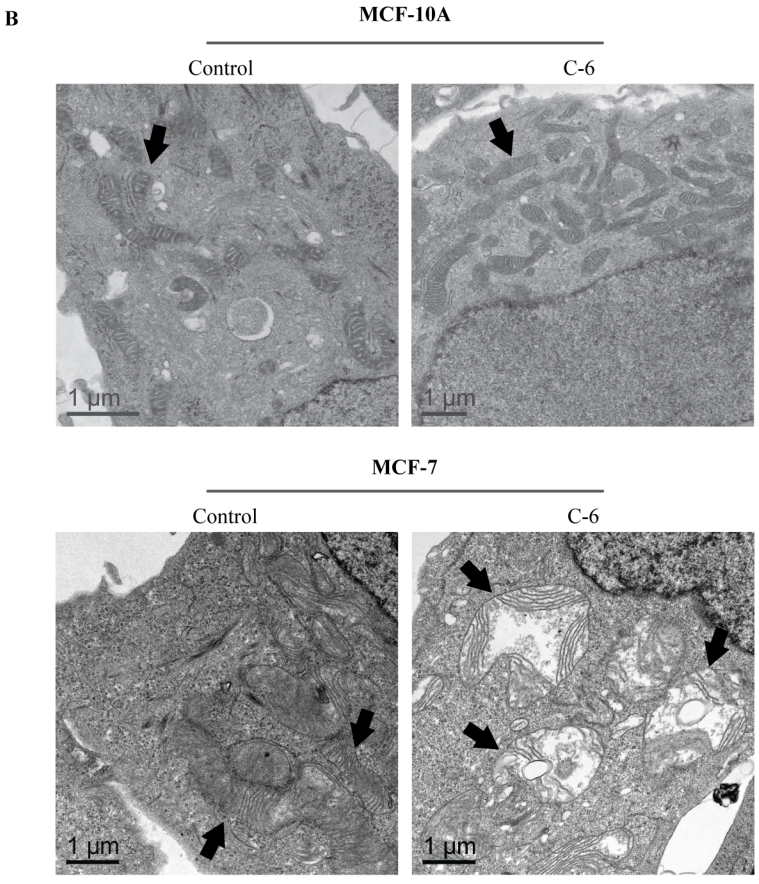
B
MCF-10A
Control
C-6
1 µm
MCF-7
Control
C-6
1 µm

alterations in mitochondrial morphology between control and treated conditions. Paraptosis, a caspase independent form of programmed cell death, was considered as a possible explanation for these morphological observations because the cell death program is characterized by cytoplasmic vacuole formation, mitochondrial swelling, and ER dysfunction. Furthermore, the paraptosis-associated vacuole phenotype can be prevented by pharmacologically inhibiting transcription and translation (19). Therefore, experiments were conducted to assess whether the formation of C-6-induced vacuoles could be blocked by cotreatment with Actinomycin D or cycloheximide, inhibitors of transcription and translation, respectively. Three breast cancer cell lines were treated with either C-6 alone or in combination with Actinomycin D or cycloheximide; subsequently, cells were stained with MitoTracker, a fluorescent mitochondrial marker, and live-imaged (Figure 3.8). Consistent with others' reports detailing features of paraptosis, C-6-induced mitochondrial swelling and cytoplasmic vacuolation were inhibited by both Actinomycin D and cycloheximide (20, 21). In all, the results of these experiments reveal that C-6 treatment significantly alters mitochondrial morphology, which may implicate paraptotic processes as contributors to C-6's biological activity.

Energetic homeostasis is perturbed by C-6 treatment

Upon discovering the marked affect of C-6-treatment on mitochondrial morphology, metabolomics profiling experiments were conducted to assess the impact of C-6 on the organelle's function. Specifically, metabolic intermediates related to the tricarboxylic acid (TCA) cycle, an ATP generating cycle that functions within mitochondria, were measured. These experiments were conducted using MCF-7 breast

Figure 3.8. Inhibitors of transcription and translation block the formation of C-6-induced vacuoles. Three breast cancer cells lines were treated with C-6 alone or in combination with Actinomycin D, a transcription inhibitor, or cycloheximide, a translation inhibitor. After 24 hours of treatment, mitochondria were stained with MitoTracker and the cells imaged by phase contrast microscopy. Scale bar represents 10 μm.

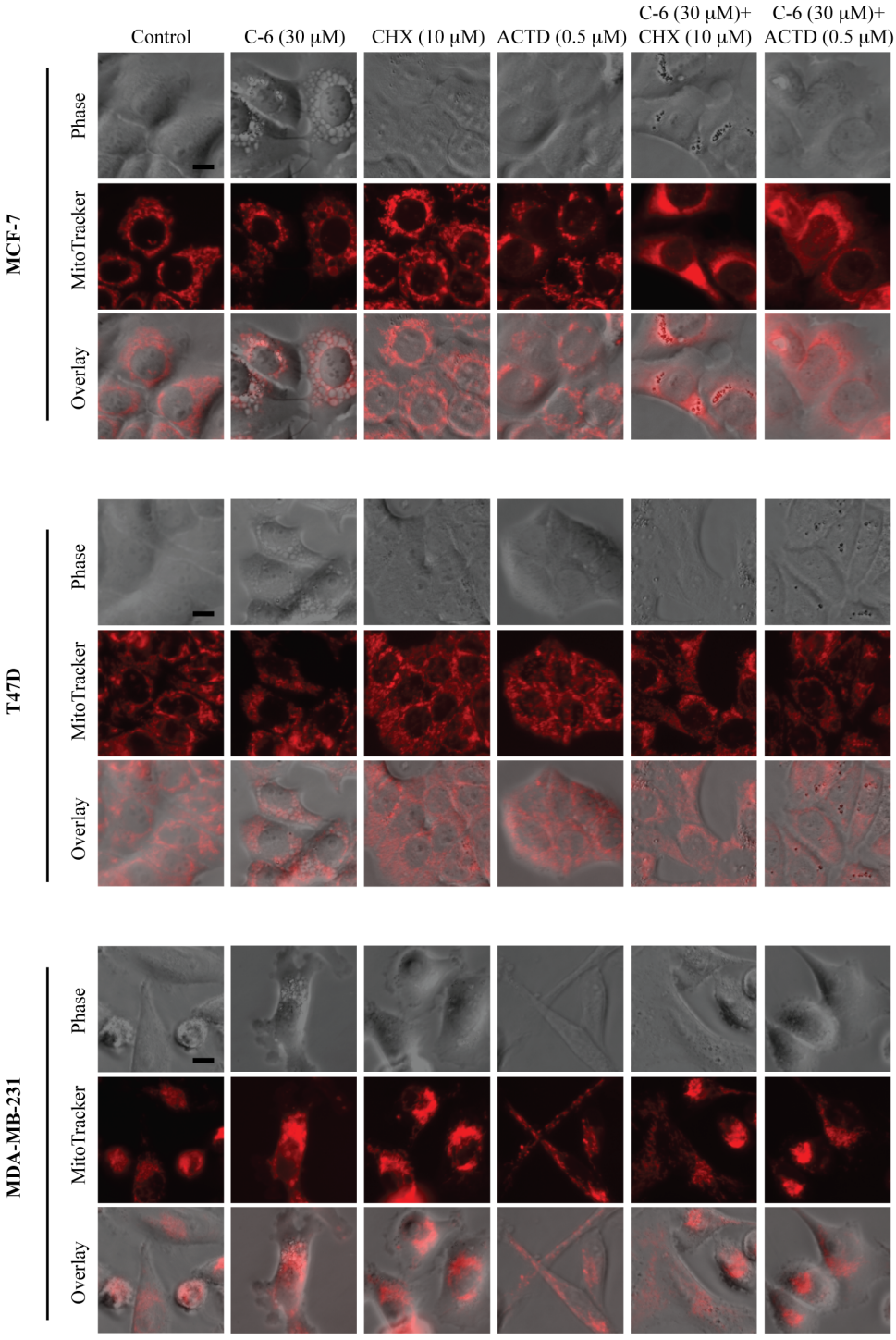
Control
C-6 (30 μM)
CHX (10 μM)
ACTD (0.5 μM)
C-6 (30 μM)+ CHX (10 μM)
C-6 (30 μM)+ ACTD (0.5 μM)
MCF-7
T47D
MDA-MB-231
Phase
MitoTracker
Overlay

cancer cells and MCF-10A untransformed mammary epithelial cells as models; the cells were treated with C-6 for three hours, then TCA cycle intermediates quantified by gas chromatography-mass spectrometry analysis. The results of these experiments revealed that MCF-10A cells exhibited decreases in NADPH, acetyl-CoA, and succinyl-CoA and increases in NADH; MCF-7 cells exhibited increases in AMP and decreases in succinyl-CoA (Figure 3.9A). These changes in TCA cycle intermediates suggest that cells experience energy imbalances as a result of C-6 treatment. Furthermore, even while C-6-insensitive MCF-10A cells do not develop swollen mitochondria as a result of treatment with the small molecule, these metabolomic data suggest that mitochondrial function is still altered.

The altered metabolomics profile observed in C-6-treated cells prompted us to further examine mitochondrial function. Using three breast cancer cell lines and one untransformed mammary epithelial cell line, experiments were conducted to measure cellular oxygen consumption since functional mitochondria consume oxygen in a manner that can be directly correlated to cellular energy production. Cells were treated with C-6 for 3, 6, 12, or 24 hours; then oxygen consumption was measured using a Seahorse Bioscience XF24 analyzer and exogenous small molecule mitochondrial stressors were added sequentially to the cells to assess the function of the electron transport chain. Interestingly, the experiments revealed that both C-6 sensitive and insensitive cells had decreases in oxygen consumption following treatment. Furthermore, after 24 hours of treatment with C-6, oxygen consumption was completely abolished in all cell types tested (Figure 3.9B). Further examining the fidelity of the electron transport chain as measured by cellular responses to the exogenously added mitochondrial stressors (i.e., oligomycin, a complex IV inhibitor, FCCP, an uncoupling agent, and rotenone/myxothiazol, complex

Figure 3.9. Mitochondrial function is perturbed by treatment with C-6. (A) A metabolomics analysis of an untransformed cell line (MCF-10A) and a breast cancer cell line (MCF-7) was conducted to measure levels of metabolites associated with the tricarboxylic acid cycle following treatment with 30 μM C-6 for three hours. The experiment was conducted in triplicate and the reported values are the average of the replicates. Metabolites whose levels were increased (i.e., p-value ≤ 0.05) are denoted in green; those whose levels were decreased are denoted in red. (B) Cellular oxygen consumption was measured in cells treated with C-6 for either 3, 6, 12, or 24 hours. Mitochondrial stressors oligomycin (oligo), carbonyl cyanide 4-(trifluoromethoxy) phenylhydrazone (FCCP), rotenone (rot), and myxothiazol (myx) were added sequentially during the measurement procedure to assess the function of the electron transport chain. Values plotted represent to average of three replicates whose values were normalized to total protein; error bars represent the standard deviation. (C) C-6 was added to MCF-7 cells while measuring oxygen consumption. Values plotted represent the average of three replicates whose values were normalized to total protein; error bars represent the standard deviation.

A

MCF-10A

	Fold change over control	p-value
NADPH	0.43	0.0151
NADH	2.28	0.0003
NADP	0.61	0.1376
NAD	0.61	0.1011
AMP	1.25	0.1078
ADP	0.89	0.4478
ATP	0.49	0.1307
Acetyl-CoA	0.56	0.0061
Succinyl-CoA	0.28	0.0121
GDP	0.89	0.5345
GTP	0.44	0.0629
Coenzyme A	1.09	0.7056

MCF-7

	Fold change over control	p-value
NADPH	1.57	0.1906
NADH	2.07	0.0680
NADP	0.99	0.9553
NAD	0.96	0.6186
AMP	1.52	0.0000
ADP	1.13	0.1957
ATP	0.90	0.2831
Acetyl-CoA	1.41	0.0822
Succinyl-CoA	0.31	0.0001
GDP	0.93	0.4370
GTP	0.83	0.3665
Coenzyme A	0.57	0.3675

B

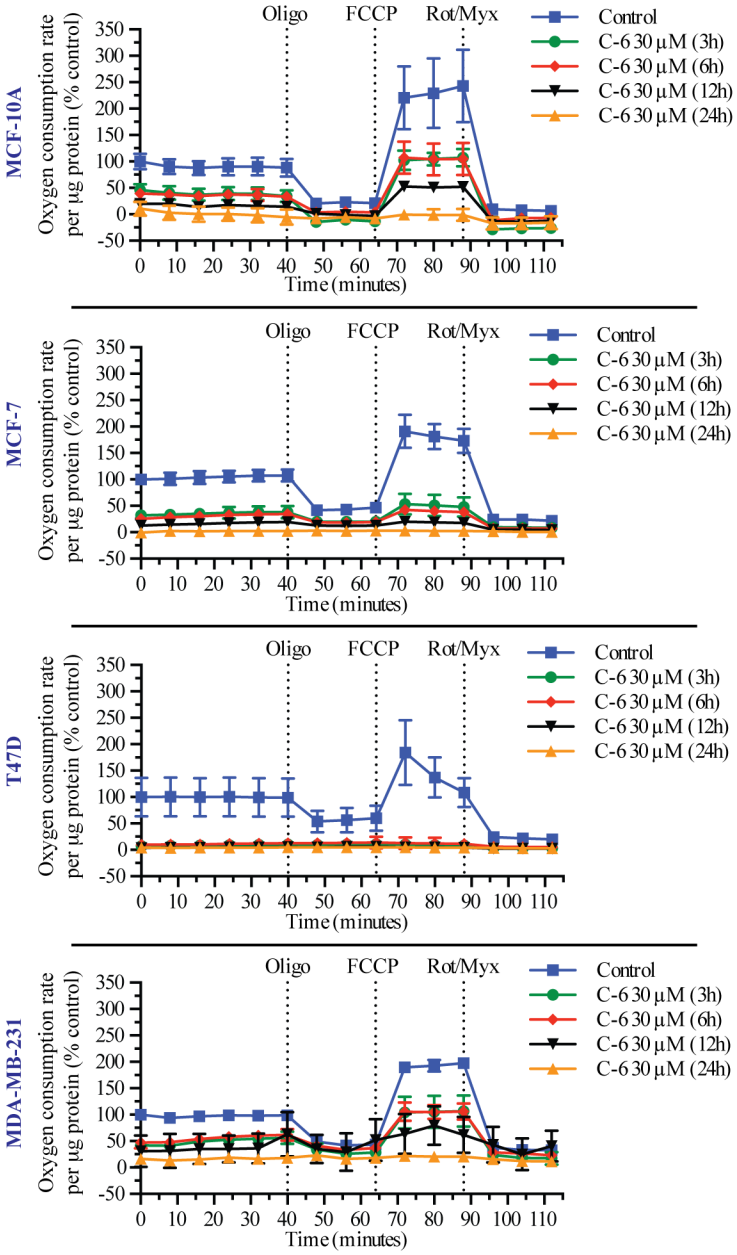

C

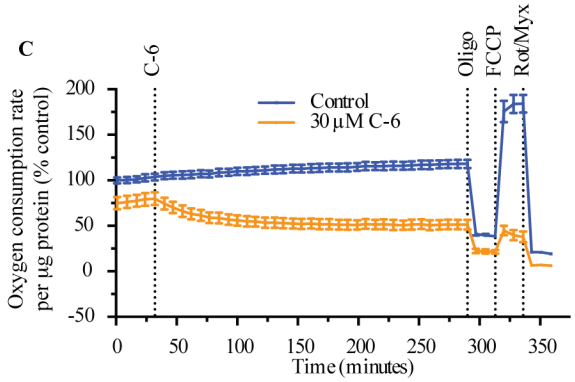

I and III inhibitors, respectively), no apparent defects were observed (22). In an effort to elucidate the kinetics of C-6's effect, an experiment was conducted with MCF-7 cells wherein the small molecule was added to untreated cells simultaneously while measuring oxygen consumption. Interestingly, C-6 was found to immediately reduce cellular respiration upon its addition to cells (Figure 3.9C). Collectively, the results of these studies revealed that C-6 dramatically affects cellular oxygen consumption. Also, these results indicate that the presence of mitochondrial swelling, as was observed in cancer cells by TEM imaging, is not a sole predictor of respiratory defect.

Mitochondrial defects and respiratory dysfunction have been reported to be associated with the production of reactive oxygen species (ROS) and general oxidative imbalance (23, 24). Considering this, experiments to establish whether C-6 induced oxidative imbalances were employed. Four cells types, including both malignant and nonmalignant types, were treated with C-6 in a time course experiment. Utilizing the indicator 2',7'-dichlorodihydrofluorescein diacetate (H_2DCFDA), whose intracellular oxidation to the fluorescent 2',7'-dichlorofluorescein (DCF) can be measured by flow cytometry, the cells were stained following the completion of treatment and fluorescence measured (Figure 3.10A). A significant increase in intracellular fluorescence was observed in three breast cancer cell lines following a time course treatment with C-6 while no increases were observed in an untransformed mammary epithelial cell line. Considering the possibility that oxidative imbalances or ROS may be responsible for C-6's cytotoxic effect in cancer cells, experiments were designed wherein cells were treated in combination with C-6 and exogenously added antioxidants; the ability of the antioxidants to rescue cell death was then assessed by measuring cell viability using an ATPlite assay. Using MCF-7 cells as a model, antioxidants *N*-acetylcysteine (NAC), *N*-

Figure 3.10. C-6-treatment alters redox homeostasis preferentially in tumor cells. (A) A mammary epithelial cell line (MCF-10A) and three breast cancer cell lines (MCF-7, T47D, and MDA-MB-231) were treated with C-6 for up to 48 hours. The cells were then stained with 2',7'-dichlorodihydrofluorescein diacetate (H_2DCFDA) whose intracellular oxidation generates the fluorescent molecule 2',7'-dichlorofluorescein (DCF); quantification of fluorescence was accomplished by flow cytometry. Values plotted represent the mean of three independent replicates whose values were normalized to a vehicle-treated control; error bars represent standard deviation. Statistical significance is annotated with one (p-value ≤ 0.05) or two (p-value ≤ 0.01) asterisk(s). (B) Twelve-point dose response analyses were conducted with MCF-7 cells; cells were treated with increasing concentrations of C-6 alone or in combination with *N*-acetylcysteine (NAC), *N*-(2-mercaptopropionyl)-glycine (NMPG), butylated hydroxyanisole (BHA), or ascorbate. Values plotted represent the average of three replicates whose values were normalized to a vehicle-treated control; error bars represent standard deviation.

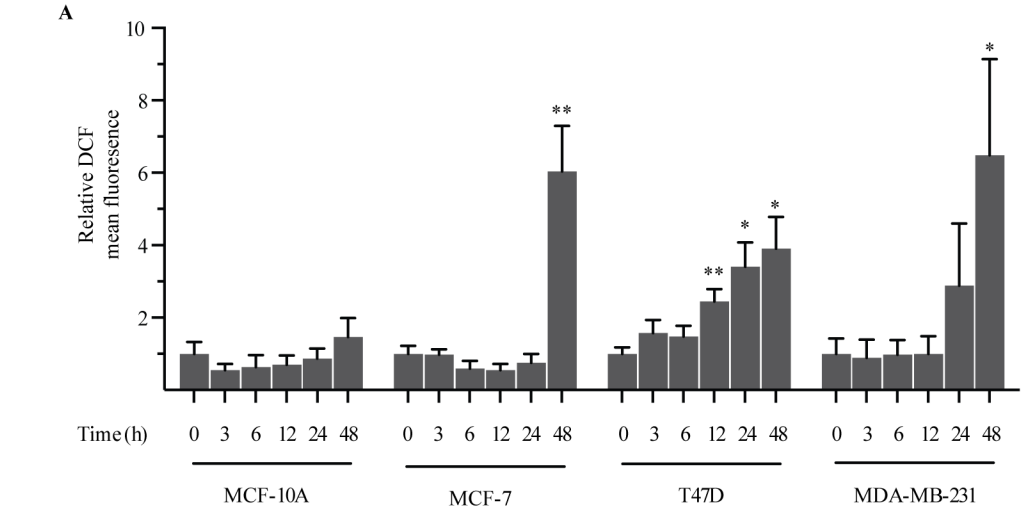
A
Relative DCF mean fluorescence
10
8
6
4
2
**
*
**
*
*
Time (h)
0 3 6 12 24 48
MCF-10A
MCF-7
T47D
MDA-MB-231

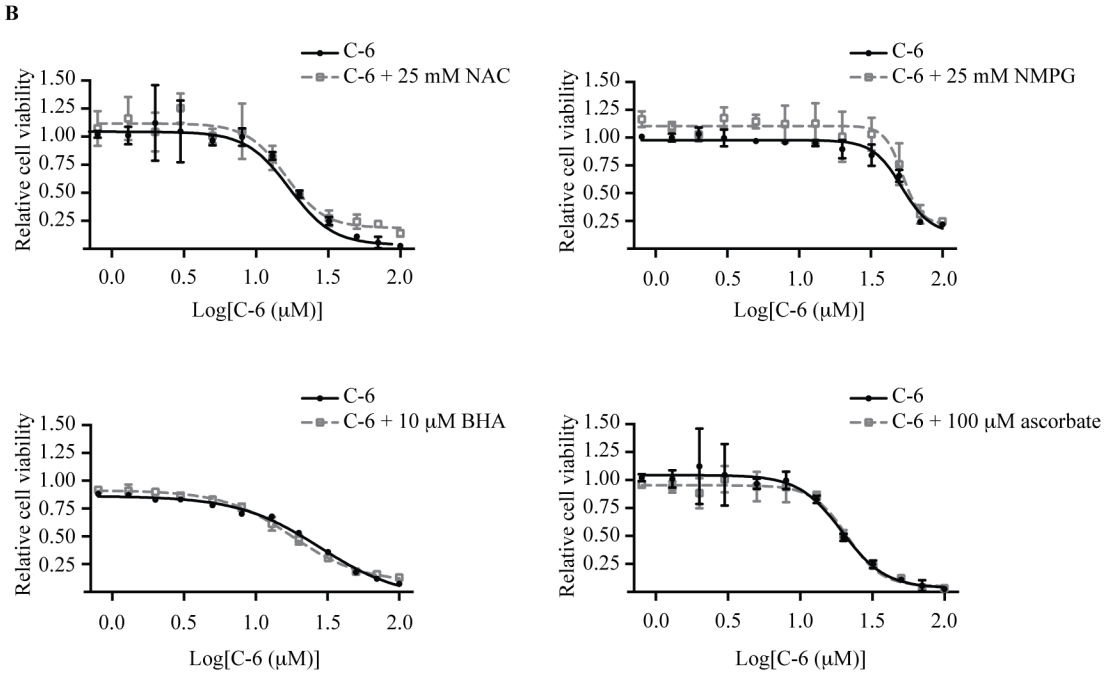
B
C-6
C-6 + 25 mM NAC
C-6 + 25 mM NMPG
C-6 + 10 μM BHA
C-6 + 100 μM ascorbate
Relative cell viability
1.50
1.25
1.00
0.75
0.50
0.25
0.0 0.5 1.0 1.5 2.0
Log[C-6 (μM)]

(2-mercaptopropionyl)-glycine (NMPG), butylated hydroxyanisole (BHA), and ascorbate were evaluated for their ability to reduce cell death. Unfortunately, no antioxidant co-treatment condition resulted in a rescue of C-6-induced cell death (Figure 3.10B). Collectively, these results suggest that C-6 induces oxidative imbalances but this induction is not compulsory for C-6's cytotoxicity.

Discussion

The chemical biology approach to the study of complex biological systems has and continues to be an effective method for understanding molecular processes and disease states. Small molecules have been used to characterize protein-protein interactions, detail cellular signaling pathways, and define new therapeutic targets in disease (25). Overall, the structural diversity that can be achieved with small molecules allows for their adaptation to many facets of life science. One focus of the Sigman and Welm labs has been to identify vulnerabilities of cancer cells that can be targeted pharmacologically. Utilizing a chemical biology approach, molecules that modulate signaling pathways specific to cancer cells have been identified. The work presented here explores the biological activity of one of these molecules and aims to increase our understanding of cancer cell biology while providing insight into tumor cell vulnerabilities and dependencies.

Previously, our labs reported the development of a small molecule screen that utilizes patient-derived malignant pleural effusion cells; these cells were derived from breast cancer patients who had developed metastatic and treatment-refractory disease (5). The screen was designed to identify small molecules capable of eradicating tumor cells

preferentially over nonmalignant cells and the resulting molecules could then be used as molecular tools to mechanistically study the biological processes affected. One such molecule, C-6, was chosen from the screen for its cytotoxicity against patient-derived malignant pleural effusion cells while being nearly inert against untransformed mammary epithelial cells. Validation studies with other cell types revealed the generality of C-6's effect: malignant cells were sensitive to treatment with the small molecule while untransformed cells were not. Prompted by this finding, and even more so the finding that C-6 was active against chemoresistant cells, an investigation was initiated to understand the basis for C-6's biological activity in tumor cells.

Based on the design of the initial small molecule screen wherein C-6 was identified, it was expected that only molecules with cytotoxic phenotypes would be identified. Molecules that induced cytostatic effects exclusively would not elicit a detectable response in the slowly proliferating malignant pleural effusion cells after only four days of treatment. However, initial mode of action studies with a variety of cell types revealed that in tumor cells, the small molecule could promote both phenotypes, with each resulting in a decrease in cell viability overall. Importantly though, untransformed cells were neither killed nor growth arrested following exposure to the small molecule.

Further studies aimed to understand C-6's mode of action in tumor cells revealed that the small molecule could induce caspase independent cell death. Cellular programs of caspase independent cell death have been characterized and reported by others although the field has received less attention than classical caspase-mediated apoptosis. Autophagy, necroptosis, paraptosis, and necrosis are the most frequently reported forms of caspase independent cell death but other types not conforming to these modes have

been described (26-29). Based upon the data presented here, necroptosis and necrosis cannot be excluded as possible mechanisms of C-6-induced tumor cells death. More evidence (i.e., mitochondrial swelling and ER dysfunction) does support the idea that paraptotic programs are responsible for cell death promoted by exposure to the small molecule though. Collectively though, caspase inactivity is a defining feature of C-6's mode of action in cell types sensitive to the small molecule's cytotoxic effects.

Another defining characteristic of C-6's biological activity is its profound effect on cellular energy homeostasis. Tumor cells, but not untransformed cells, exposed to the small molecule develop prominent cytoplasmic vacuoles and the results of TEM imaging experiments clearly implicate enlarged mitochondria as the source of these features. We were therefore surprised to find that both cell types, transformed and untransformed, experienced dramatic decreases in cellular oxygen consumption following treatment with C-6. Taken together, these results indicate that mitochondrial swelling is not the source of respiratory disruption, but is likely a response to the disturbance. Alternative energy production pathways (i.e., glycolysis outside of the mitochondria) are significantly less efficient in the production of ATP; oxidative phosphorylation within a mitochondrion can produce a maximum of 36 molecules of ATP while cytoplasmic glycolysis can produce a maximum of only 2 molecules of ATP (30). Since even cells that are insensitive to the cytotoxic effects of C-6 experience decreases in oxygen consumption, it is expected then that their survival and continued proliferation is dependent upon aerobic and glycolytic pathways for the production of ATP. The idea that transformed cells do not possess the glycolytic capacity to survive disruptions in oxidative phosphorylation, however, is in opposition to the observation that tumor cells utilize the glycolytic pathway as their main energy producing pathway, a phenomenon known as the Warburg effect (31, 32). In

summary, it is unlikely that C-6's affect on mitochondrial respiration is the sole predictor of sensitivity to the molecule's cytotoxic effects, although energetic dyshomeostasis is still likely to contribute to cell death via the induction of general cell stress.

Considering the sum of the results presented herein, the presence of mitochondrial swelling and disruptions in cellular redox homeostasis are the strongest indicators of a cell's response to C-6-treatment. That is, C-6's ability to reduce cell viability in tumor cells but not untransformed cells can be predicted based on the occurrence of these two characteristics. Considering the redox dyshomeostasis, the imbalance is likely more complex then simply the production of ROS. The oxidation of nonfluorescent H_2DCFDA to florescent DCF, which was used to measure changes in cellular redox states, can occur via a variety of intracellular (33). For example, probe oxidation has been reported to occur in the presence of cytochrome C or H_2O_2 in conjunction with redox-active metal activation (34). Others have reported that intracellular iron distribution significantly affects probe oxidation (35). In all, probe oxidation can still be interpreted as an indicator of changes in cellular redox states, although the exact molecular basis for the imbalance cannot be inferred. With C-6-treatment, the failure of antioxidants to significantly rescue C-6 induced cell death may be an indicator of a metal-based mechanism by which the redox imbalance occurs.

In conclusion, the results of the studies presented herein identify disruptions in several key biological processes following exposure to C-6. Specifically, disruptions in cell cycle progression, mitochondrial respiration, and cellular redox homeostasis were discovered. Considering these findings in the context of the original goal to identify vulnerabilities in drug-refractory tumor cells, insight into the development of new treatment strategies can be gained. Specifically, perturbations in cellular redox

homeostasis may prove to be a generalizable mechanism to target chemoresistant tumor cells. Further work to delineate the specific mechanism by which C-6 induces redox imbalances will be a necessary next step towards determining this, but the results presented here establish the foundation for future work defining new therapeutic targets for drug resistant cancers.

Methods

Detailed descriptions of the materials and methods used for the study presented herein have been reported previously (36). For statistical analyses of the data herein, the student's t-test (unpaired) was used to assess statistical significance and a $p \leq 0.05$ was considered statistically significant. The following p-values were used to annotate statistical significance: $p \leq 0.05$ = *; $p \leq 0.01$ = **; $p \leq 0.001$ = ***.

References

1. Brown EJ*, et al.* (1994) A mammalian protein targeted by G1-arresting rapamycin-receptor complex. *Nature* 369(6483):756-758.

2. Sabatini DM, Erdjument-Bromage H, Lui M, Tempst P, & Snyder SH (1994) RAFT1: a mammalian protein that binds to FKBP12 in a rapamycin-dependent fashion and is homologous to yeast TORs. *Cell* 78(1):35-43.

3. Weisenberg RC, Broisy GG, & Taylor EW (1968) Colchicine-binding protein of mammalian brain and its relation to microtubules. *Biochemistry* 7(12):4466-4479.

4. Rosen ED, Walkey CJ, Puigserver P, & Spiegelman BM (2000) Transcriptional regulation of adipogenesis. *Genes Dev* 14(11):1293-1307.

5. Gligorich K*, et al.* (2013) Development of a screen to identify selective small molecules active against patient-derived metastatic and chemoresistant breast

cancer cells. *Breast Cancer Res* 15(4):R58.

6. Rabinovitch PS, Kubbies M, Chen YC, Schindler D, & Hoehn H (1988) BrdU—Hoechst flow cytometry: a unique tool for quantitative cell cycle analysis. *Exp Cell Res* 174(2):309-318.

7. Rixe O & Fojo T (2007) Is cell death a critical end point for anticancer therapies or is cytostasis sufficient? *Clin Cancer Res* 13(24):7280-7287.

8. Elmore S (2007) Apoptosis: a review of programmed cell death. *Toxicol Pathol* 35(4):495-516.

9. He C & Klionsky DJ (2009) Regulation mechanisms and signaling pathways of autophagy. *Annu Rev Genet* 43(1):67-93.

10. Kabeya Y*, et al.* (2000) LC3, a mammalian homologue of yeast Apg8p, is localized in autophagosome membranes after processing. *EMBO J* 19(21):5720-5728.

11. Walter P & Ron D (2011) The unfolded protein response: from stress pathway to homeostatic regulation. *Science* 334(6059):1081-1086.

12. Oyadomari S & Mori M (2003) Roles of CHOP//GADD153 in endoplasmic reticulum stress. *Cell Death Differ* 11(4):381-389.

13. Rao RV*, et al.* (2002) Coupling endoplasmic reticulum stress to the cell death program: role of the ER chaperone GRP78. *FEBS Letters* 514(2–3):122-128.

14. Prostko C, Brostrom M, & Brostrom C (1993) Reversible phosphorylation of eukaryotic initiation factor 2α in response to endoplasmic reticular signaling. *Reversible Protein Phosphorylation in Cell Regulation,* Developments in Molecular and Cellular Biochemistry, eds Khandelwal RL & Wang JH (Springer, US), Vol 11, pp 255-265.

15. Kyriakis JM*, et al.* (1994) The stress-activated protein kinase subfamily of c-Jun kinases. *Nature* 369(6476):156-160.

16. Srivastava RK*, et al.* (1999) Bcl-2 and Bcl-XL block thapsigargin-induced nitric oxide generation, c-Jun NH2-terminal kinase activity, and apoptosis. *Mol Cell Biol* 19(8):5659-5674.

17. Urano F*, et al.* (2000) Coupling of stress in the ER to activation of JNK protein kinases by transmembrane potein kinase IRE1. *Science* 287(5453):664-666.

18. Shen H-M & Liu Z-g (2006) JNK signaling pathway is a key modulator in cell death mediated by reactive oxygen and nitrogen species. *Free Radic Biol Med* 40(6):928-939.

19. Sperandio S, de Belle I, & Bredesen DE (2000) An alternative, nonapoptotic form of programmed cell death. *Proc Natl Acad Sci USA* 97(26):14376-14381.

20. Wang Y*, et al.* (2004) An alternative form of paraptosis-like cell death, triggered by TAJ/TROY and enhanced by PDCD5 overexpression. *J Cell Sci* 117(8):1525-1532.

21. Gandin V*, et al.* (2012) A novel copper complex induces paraptosis in colon cancer cells via the activation of ER stress signalling. *J Cell Mol Med* 16(1):142-151.

22. Dranka BP*, et al.* (2011) Assessing bioenergetic function in response to oxidative stress by metabolic profiling. *Free Radic Biol Med* 51(9):1621-1635.

23. Schumacker PT (2006) Reactive oxygen species in cancer cells: live by the sword, die by the sword. *Cancer Cell* 10(3):175-176.

24. Sena LA & Chandel NS (2012) Physiological roles of mitochondrial reactive oxygen species. *Mol Cell* 48(2):158-167.

25. Schreiber SL (2003) The small-molecule approach to biology. *C&EN* 81(9):51-61.

26. Tait SWG & Green DR (0000) Caspase-independent cell death: leaving the set without the final cut. *Oncogene* 27(50):6452-6461.

27. Bröker LE, Kruyt FAE, & Giaccone G (2005) Cell death independent of caspases: a review. *Clin Cancer Res* 11(9):3155-3162.

28. Kroemer G & Martin SJ (2005) Caspase-independent cell death. *Nat Med* 11(7):725-730.

29. Vandenabeele P, Galluzzi L, Vanden Berghe T, & Kroemer G (2010) Molecular mechanisms of necroptosis: an ordered cellular explosion. *Nat Rev Mol Cell Biol* 11(10):700-714.

30. Vander Heiden MG, Cantley LC, & Thompson CB (2009) Understanding the warburg effect: the metabolic requirements of cell proliferation. *Science* 324(5930):1029-1033.

31. Pelicano H, Martin DS, Xu RH, & Huang P (0000) Glycolysis inhibition for anticancer treatment. *Oncogene* 25(34):4633-4646.

32. Kim J-w & Dang CV (2006) Cancer's molecular sweet tooth and the warburg effect. *Cancer Res* 66(18):8927-8930.

33. Halliwell B & Whiteman M (2004) Measuring reactive species and oxidative

damage in vivo and in cell culture: how should you do it and what do the results mean? *Br J Pharmacol* 142(2):231-255.

34. Karlsson M, Kurz T, Brunk UT, Nilsson SE, & Frennesson CI (2010) What does the commonly used DCF test for oxidative stress really show? *Biochemical Journal* 428(2):183-190.

35. Tampo Y*, et al.* (2003) Oxidative stress–induced iron signaling is responsible for peroxide-dependent oxidation of dichlorodihydrofluorescein in endothelial cells: role of transferrin receptor–dependent iron uptake in apoptosis. *Circ Res* 92(1):56-63.

36. Vaden RM, Gligorich KM, Jana R, Sigman MS, & Welm BE (2014) The small molecule C-6 is selectively cytotoxic against breast cancer cells and its biological action is characterized by mitochondrial defects and endoplasmic reticulum stress. *Breast Cancer Res* (DOI: 10.1186/s13058-014-0472-0).

CHAPTER 4

EFFORTS TOWARDS THE IDENTIFICATION OF THE BIOLOGICAL TARGET OF THE ANTICANCER SMALL MOLECULE C-6

Abstract

The application of small molecules to biological systems can provide significant insight into the complex cellular signaling mechanisms of both normal cellular function and disease states. Beyond the identification of phenotypes of interest, defining the biological target of a small molecule represents a challenging but immensely informative step in the scientific process. We previously reported the identification of a small molecule, C-6, which was identified from a phenotype screen utilizing malignant pleural effusion cells derived directly from drug refractory breast cancer patients. The small molecule was found to kill cancer cells selectively over untransformed cells types in a caspase independent manner. With the overall goal of identifying vulnerabilities of drug resistant neoplastic cells, experiments were conducted to identify C-6's biological target and delineate the small molecule's mode of action. Two independent strategies were implemented to identify C-6-interacting proteins: an affinity based strategy and a genetic mutagenesis screen. A C-6 variant containing a photoaffinity moiety was generated and used for protein crosslinking studies. While the results of these studies suggest that C-6 binds the protein TMEM109, the implications of this binding interaction on cell death processes remains unclear. The results of the genetic mutagenesis screen using randomly genetrapped near-haploid cells were also inconclusive. Presented herein are the results of these studies and experimental design modifications that may be useful for future studies aimed at identifying the biological targets of other small molecules.

Introduction

Elucidating the biological targets of small molecules identified from phenotype screens is frequently referred to as the "bottleneck" of drug discovery (1-4). The complexity of biological signaling pathways and the sheer number of proteins whose functions have not been fully characterize consistently confound efforts to understand how small molecules operate in the cellular milieu. Even with these challenges, a wealth of knowledge can be gained by understanding the mechanistic basis for a small molecule's activity. Furthermore, using molecular tools to define novel signaling pathways has broad implications outside of disease research and can provide information about normal and developmental processes as well. Several approaches have been developed for the identification of small molecule binding partners including functional genetic, bioinformatic, and affinity-based strategies (5-8).

Previously, we reported the identification of a small molecule, C-6, with unique anticancer activity (9, 10). The small molecule was found to selectively kill patient-derived malignant pleural effusion cells, leaving untransformed cells largely unaffected. Importantly, these malignant pleural effusion cells were obtained from breast cancer patients who had developed drug refractory disease. The discovery that C-6 was active against these particularly aggressive cell types prompted further investigations into its mechanism of action with the overall goal of identifying vulnerabilities of chemoresistant cells. Considering the valuable insight that could be gained by understanding the specific biological pathways modulated by C-6, we initiated a series of experiments to identify proteins that interact with the small molecule. Herein are presented the results of these studies in addition to technical insights gained during the project's development that may facilitate future target identification successes.

Results

C-6 analogs with cytotoxic profiles comparable to the parent molecule can be generated

As a first step towards our goal of identifying proteins that interact with the anticancer molecule C-6, we undertook an investigation to characterize how the structural components of the small molecule influenced potency and cancer-selectivity in whole cell viability assays. A series of analogs that contained structural modifications to both the A-ring and B-ring of C-6 and also to the diarylmethine position were designed (Figure 4.1A). The synthetic route to access the analogs was developed by Dr. Ranjan Jana, a colleague in the Sigman lab, and utilized scaffold precursors that were inexpensive and could be easily modified to incorporate a variety of functional moieties (Figure 4.1B). Exploration of the chemical space included modifications such as exchange of the carbamate group on the A-ring for sulfonamide variants, removal of B-ring arylmethoxy groups, and incorporation of functionality at the diarylmethine position, among other changes (Table 4.1).

In all, twenty-six analogs of C-6 were prepared; with these molecules in hand, experiments were next conducted to assess the effects of the analogs on cell viability of untransformed and transformed cell types. Specifically, we sought to evaluate the potencies and cancer-selectivity profiles of the analogs as compared to the parent molecule C-6. As such, 12-point dose response analyses were conducted with each of the molecules and cell viability was subsequently measured using a [3-(4,5-dimethylthiazol-2-yl)-5- (3-carboxymethoxyphenyl)-2- (4-sulfophenyl)-2H-tetrazolium salt (MTS) assay; MCF-10A mammary epithelial cells and MCF-7 breast cancer cells were used to measure responses in untransformed and transformed cell types, respectively. From these results

Figure 4.1 The anticancer small molecule C-6 can be easily accessed. (A) Chemical structure of the small molecule C-6. (B) Synthetic route to access C-6.

A

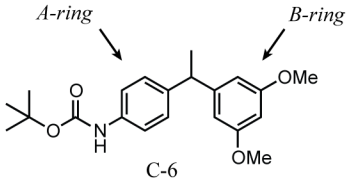

C-6

B

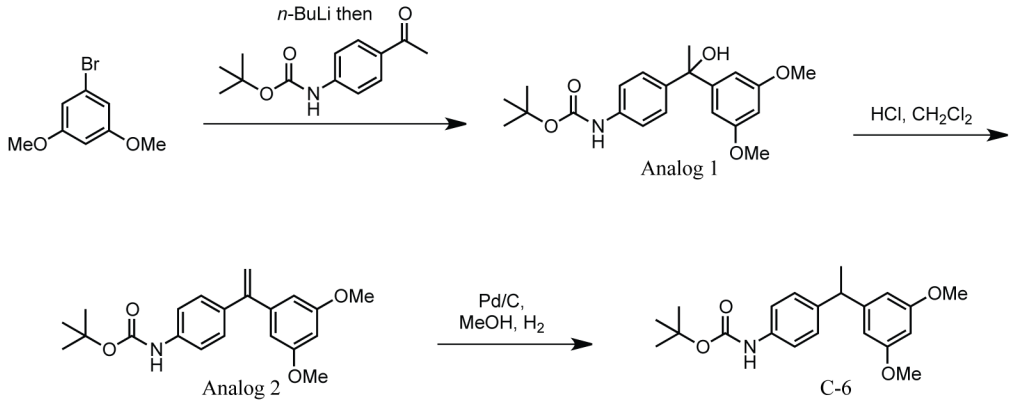

Analog 1

Analog 2

C-6

Table 4.1. Effects of C-6 derivatives on MCF-10A and MCF-7 cell viability

Chemical structure	Identifier	EC_{50} MCF-10A untransformed mammary epithelial cells	EC_{50} MCF-7 breast cancer cells
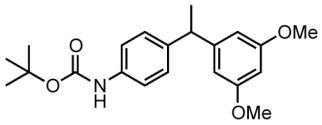	C-6	N/A	10 μM
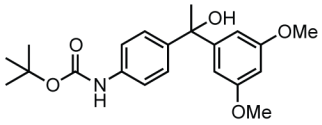	analog 1	61 μM	18 μM
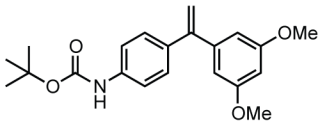	analog 2	11 μM	6.6 μM
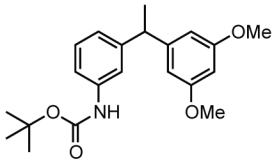	analog 3	N/A	8.4 μM
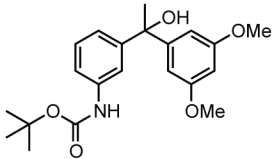	analog 4	N/A	17 μM
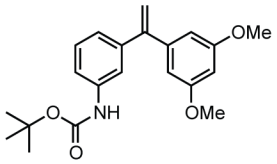	analog 5	N/A	11 μM
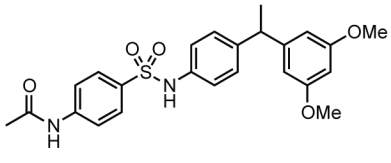	analog 6	8.3 μM	8.0 μM

Table 4.1 ***(continued)***

(continued) Chemical structure	*(continued)* Identifier	*(continued)* EC_{50} MCF-10A untransformed mammary epithelial cells	*(continued)* EC_{50} MCF-7 breast cancer cells
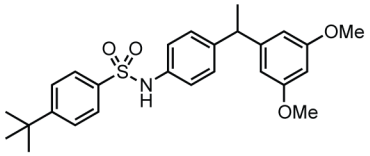	analog 7	8.1 μM	10 μM
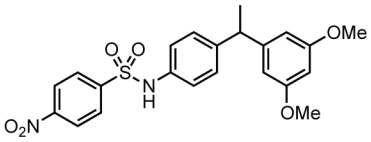	analog 8	13 μM	11 μM
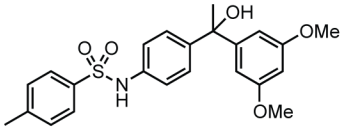	analog 9	30 μM	11 μM
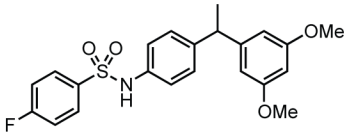	analog 10	8.2 μM	10 μM
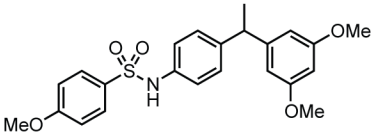	analog 11	12 μM	8.8 μM
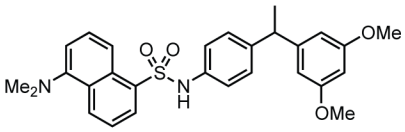	analog 12	9.6 μM	14 μM
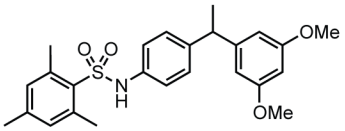	analog 13	23 μM	17 μM

Table 4.1 ***(continued)***

(continued) Chemical structure	*(continued)* Identifier	*(continued)* EC_{50} MCF-10A untransformed mammary epithelial cells	*(continued)* EC_{50} MCF-7 breast cancer cells
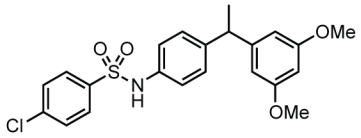	analog 14	8.6 μM	10 μM
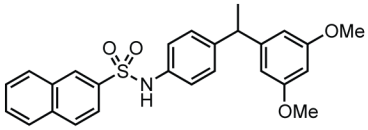	analog 15	10 μM	12 μM
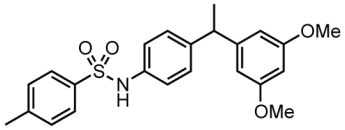	analog 16	10 μM	9.4 μM
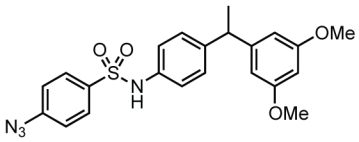	analog 17	10 μM	13 μM
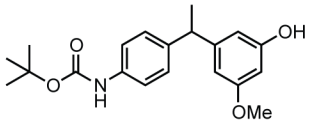	analog 18	31 μM	10 μM
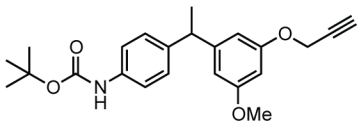	analog 19	N/A	6.7μM
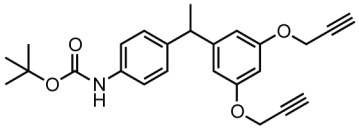	analog 20	N/A	8.9 μM

Table 4.1 ***(continued)***

(continued) Chemical structure	*(continued)* Identifier	*(continued)* EC_{50} MCF-10A untransformed mammary epithelial cells	*(continued)* EC_{50} MCF-7 breast cancer cells
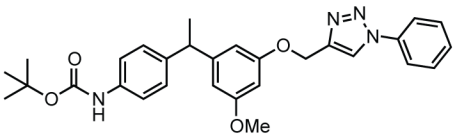	analog 21	22 μM	3.7 μM
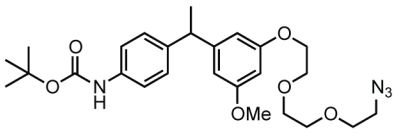	analog 22	N/A	4.9 μM
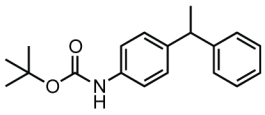	analog 23	38 μM	23 μM
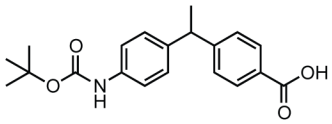	analog 24	N/A	N/A
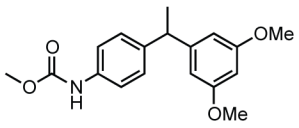	analog 25	N/A	15 μM
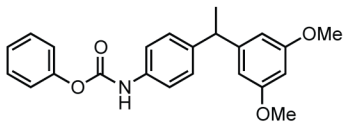	analog 26	9.0 μM	12 μM

a variety of cell responses was observed (Table 4.1). First, conversion of the carbamate group to an arylsulfonamide derivative abolished the cancer-selective phenotype of the parent molecule with every sulfonamide analog examined. Considering that analog 26 contains an aryl group pendant to the A-ring in a manner similar to the sulfonamide analogs and that its cancer-selective profile is also altered, the reduction in cancer-selectivity in both cases can likely be attributed to the presence of pendant aryl substitution. Direct alterations to the B-ring of C-6 generated a variety of profiles in the dose response assay. The efficacies of analogs 19 and 20 were comparable to C-6 while analog 24 had reduced potency overall, possibly a reflection of the compound's solubility; a decrease in cancer selectivity was observed with analog 18, suggesting that, in general, substitution on the A-ring is necessary for cancer-selectivity. In all, these results provided the preliminary information necessary for implementing additional experiments aimed at designing functional probes for the identification of proteins that interact with C-6 in the cellular milieu.

C-6 analogs activate stress pathways in a manner similar to the parent molecule

Upon establishing the efficacies of the C-6 analogs in whole cell dose response assays, focused studies were conducted to assess biological processes affected by small molecule treatment; specifically, experiments were conducted to evaluate the degree of similarity between C-6's mode of action and those of the analogs. Five defining characteristics of C-6's biological activity were chosen and analogs were evaluated against these criteria. Analogs were evaluated for their propensity to induce cytoplasmic

vacuoles, ability to induce gene expression of the endoplasmic reticulum stress protein CHOP, effect on caspase activity, effect on oxygen consumption, and impact on cellular redox homeostasis. In all, three analogs whose dose response profiles most resembled C-6's were chosen for mechanistic assessment and T47D cells were used throughout for the experimental studies. The results of these experiments collectively revealed that each analog's mode of action consistently mirrored C-6's mode of action (Figures 4.2 and 4.3). As such, analogs whose dose response profiles match that of the parent molecule likely modulate similar signaling pathways and induce comparable forms of cellular stress. These results suggest that with C-6, dose response analyses can be used to inform the design of molecular probes for the study of molecule-protein interactions.

A photoaffinity-labeled C-6 variant can be used to identify molecular binding partners

Using the knowledge gained from our analog studies, a variant of C-6 was designed that contained both a trifluoromethyl phenyldiazirine photophore and an alkyne in scaffold positions that were expected to minimally impact C-6's biological activity (Figure 4.4A). It was envisioned that the light-activated photophore could generate a covalent bond with nearby proteins and Click chemistry could subsequently be used to append a modified biotin moiety; after streptavidin protein isolation and purification, the covalently bound proteins could be identified by mass spectrometry analysis. To begin, a synthetic route was developed to generate the molecule and its synthesis accomplished (Figure 4.4B). With the C-6 variant in hand, an assessment of it effects against untransformed MCF-10A cells and MCF-7 breast cancer cells was conducted. Cell

Figure 4.2. Treatment with analogs of C-6 produce cytoplasmic vacuoles and mitochondrial swelling similar to C-6. T47D breast cancer cells were treated for 24 hours with C-6, analog 3, analog 20, or analog 5. Mitochondria were subsequently stained with MitoTracker and the cells live-imaged. Scale bar represents 10 μm.

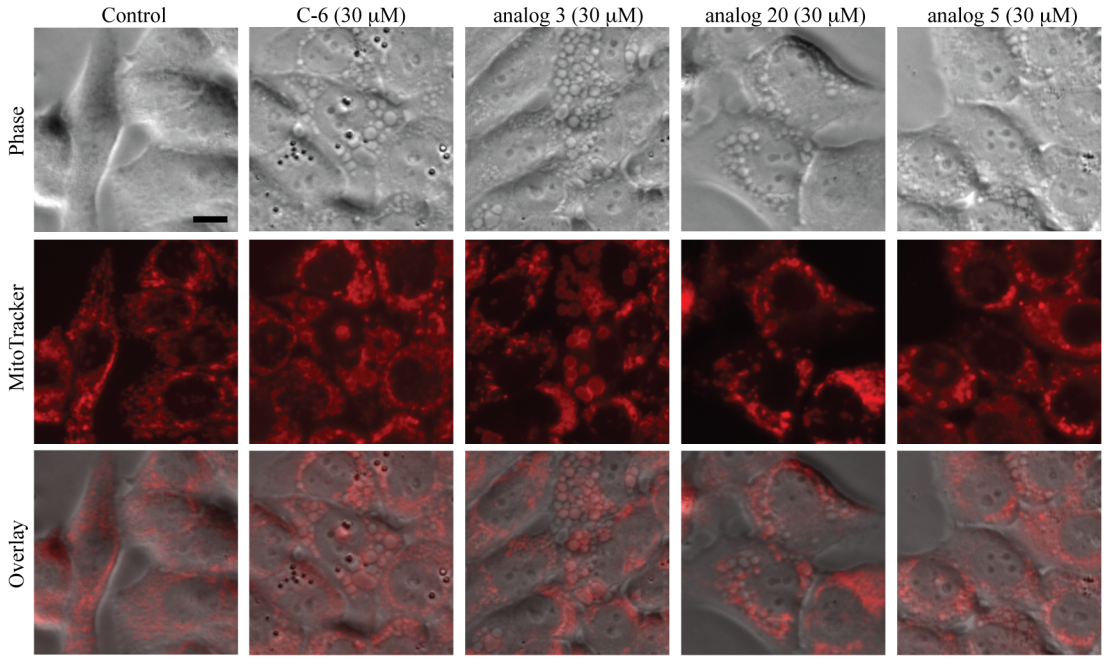
Control
C-6 (30 μM)
analog 3 (30 μM)
analog 20 (30 μM)
analog 5 (30 μM)
Phase
MitoTracker
Overlay

Figure 4.3. Analogs of C-6 modulate biological pathways in a manner similar to the parent molecule. Each experiment was conducted with T47D breast cancer cells and utilized 30 μM of either C-6, analog 3, analog 20, or analog 5; experiments conducted with staurosporine utilized a 1 μm treatment concentration. (A) Real-time polymerase chain reaction (RT-PCR) measurements of CHOP gene expression following 24 hours of treatment with either C-6 or the analogs. Error bars represent the standard deviation of four measurement replicates. Expression was internally normalized to a control gene, GAPDH. (B) Measurements of caspases 3/7, 8, and 9 activities were obtained following 72 hours of treatment with the small molecules using a Caspase-Glo assay. Values plotted represent the mean of three independent replicates and error bars represent the standard deviation. (C) Oxygen consumption measurements following a 24 hour treatment with the small molecules were obtained using a Seahorse XF24 analyzer. Values plotted represent the mean of three independent replicates and error bars represent the standard deviation. Each condition was normalized internally to total protein. (D) To assess changes in oxidative homeostasis, cells were treated for 48 hours, then stained with 2',7'-dichlorodihydrofluorescein diacetate (H2DCFDA). The oxidation of H2DCFDA to 2',7'-dichlorofluorescein (DCF) was then measured by flow cytometry. Values plotted represent the mean of three independent replicates and error bars represent the standard error of the mean.

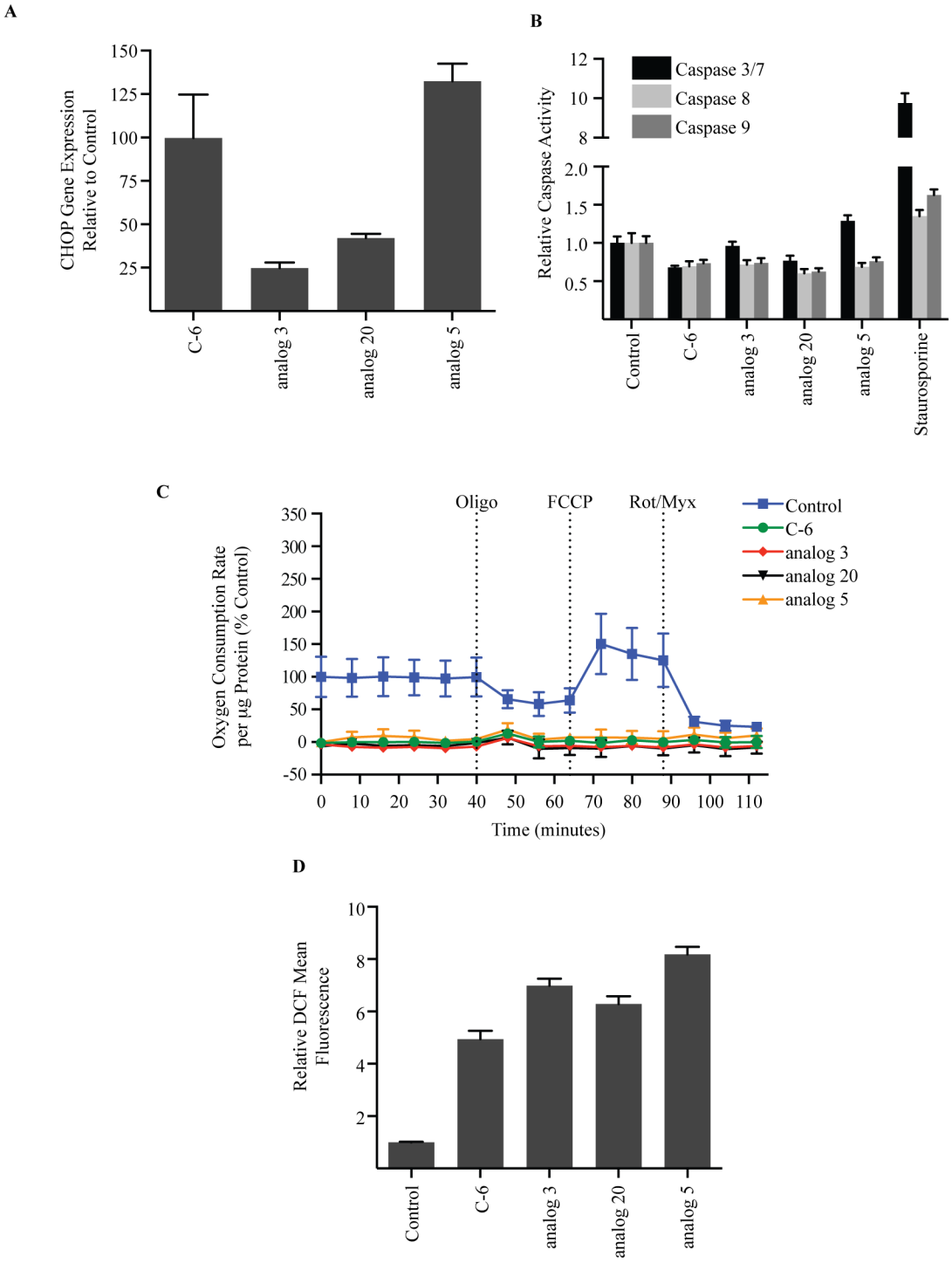
A
CHOP Gene Expression
Relative to Control
150
125
100
75
50
25
C-6
analog 3
analog 20
analog 5
B
Relative Caspase Activity
12
10
8
2.0
1.5
1.0
0.5
Caspase 3/7
Caspase 8
Caspase 9
Control
C-6
analog 3
analog 20
analog 5
Staurosporine
C
Oligo
FCCP
Rot/Myx
Control
C-6
analog 3
analog 20
analog 5
Oxygen Consumption Rate
per µg Protein (% Control)
350
300
250
200
150
100
50
0
-50
0
10
20
30
40
50
60
70
80
90
100
110
Time (minutes)
D
Relative DCF Mean
Fluorescence
10
8
6
4
2
Control
C-6
analog 3
analog 20
analog 5

Figure 4.4. The C-6-photoaffinity derivative activates cellular response pathways in a manner similar to C-6. (A) Chemical structure of C-6-photoaffinity, an analog that incorporates a diazarine photophore functional group. (B) Synthetic route to access C-6-photoaffinity. (C) Dose response analysis C-6-photoaffinity against MCF-10A mammary epithelial cells and MCF-7 breast cancer cells measuring changes in cell viability. (D) Immunoblot analysis of CHOP expression in MCF-10A and MCF-7 cells treated for 24 hours with C-6, C-6-photoaffinity, or thapsigargin as a positive control.

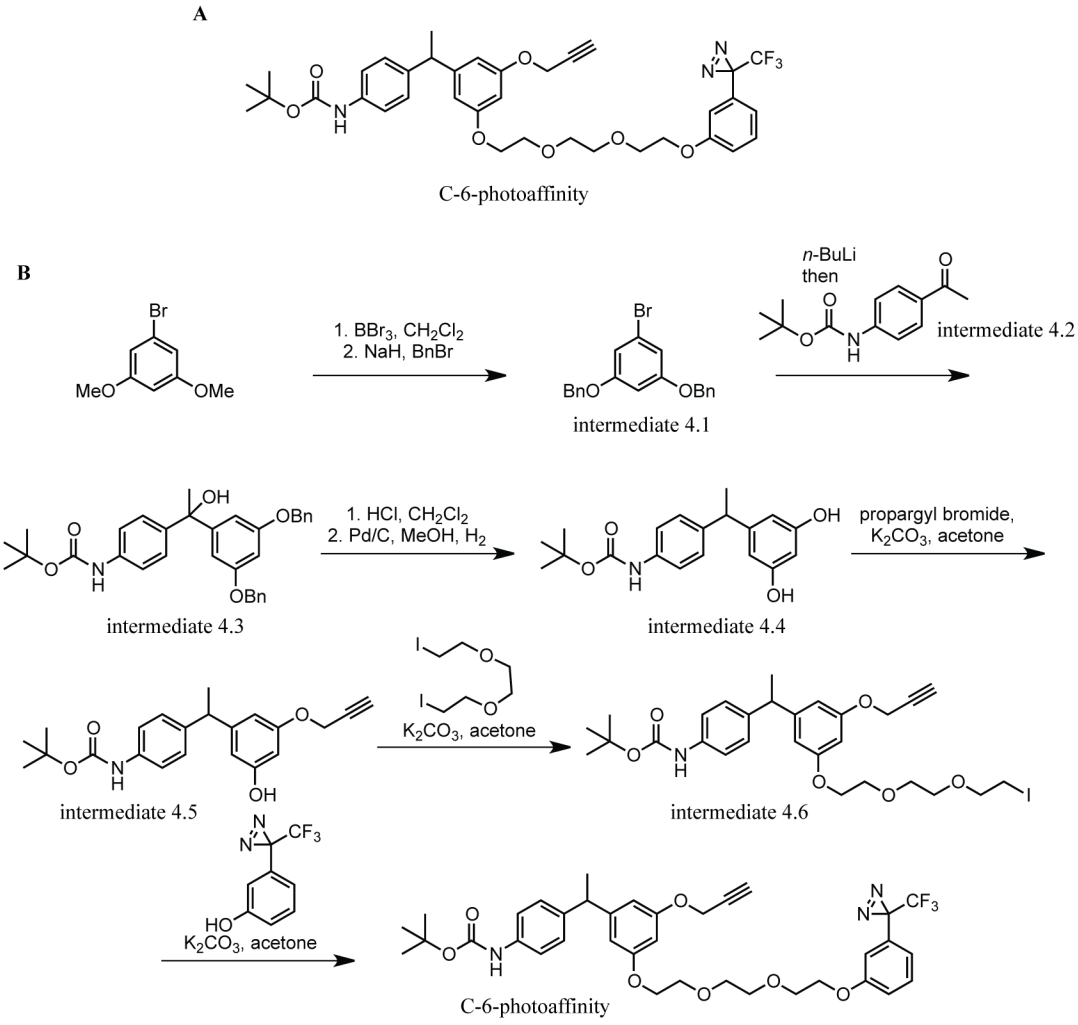
A
C-6-photoaffinity
B
1. BBr3, CH2Cl2
2. NaH, BnBr
n-BuLi
then
intermediate 4.2
intermediate 4.1
1. HCl, CH2Cl2
2. Pd/C, MeOH, H2
propargyl bromide,
K2CO3, acetone
intermediate 4.3
intermediate 4.4
K2CO3, acetone
intermediate 4.5
intermediate 4.6
K2CO3, acetone
C-6-photoaffinity

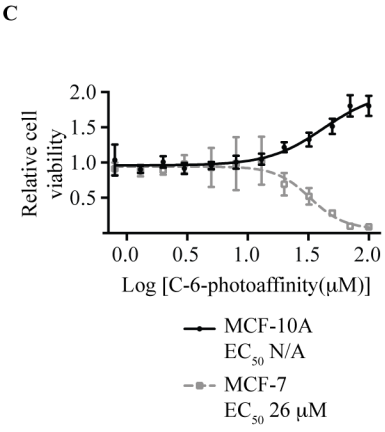
C
Relative cell viability
Log [C-6-photoaffinity(μM)]
MCF-10A
EC50 N/A
MCF-7
EC50 26 μM

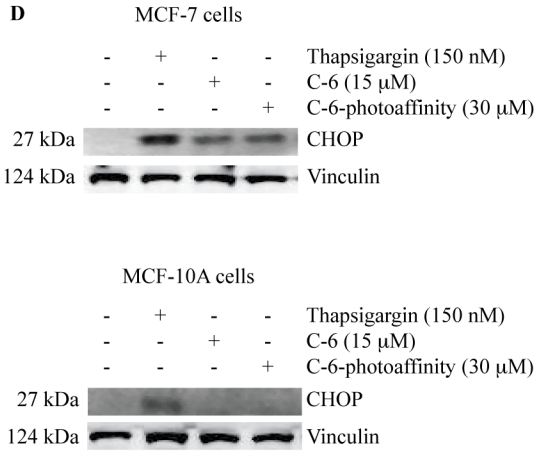
D
MCF-7 cells
Thapsigargin (150 nM)
C-6 (15 μM)
C-6-photoaffinity (30 μM)
27 kDa
CHOP
124 kDa
Vinculin
MCF-10A cells
Thapsigargin (150 nM)
C-6 (15 μM)
C-6-photoaffinity (30 μM)
27 kDa
CHOP
124 kDa
Vinculin

viability was measured following the completion of a dose response assay and the results revealed a potency and cancer-selectivity profile comparable to that of C-6 (Figure 4.4C). Further evaluation of the photoaffinity probe's mode of action was conducted to assess whether the analog stimulated expression of the endoplasmic stress protein CHOP in MCF-7 breast cancer cells; as with the parent molecule, the photoaffinity variant was found to induce expression of CHOP as measured via immunoblot experiments (Figure 4.4D). These results together suggest that photophore and alkyne incorporation do not significantly alter the mode of action of C-6. Furthermore, these data suggest that photoaffinity labeling experiments with the C-6 cognate may be used to provide analogous information about C-6's intracellular binding partners.

Before proceeding forward with cell-based studies, optimizations of the conditions necessary for successful photoactivation of the probe were conducted. For these experiments, a synthetic precursor of the photophore used in the design of the C-6 analog was employed. The photophore precursor was diluted in methanol and subsequently irradiated with varying wavelengths of light. ^{13}C NMR spectra of the resulting products were then analyzed for the incorporation of an alkyl-methoxy group originating from the methanol solvent used during irradiation. Broad spectrum, as opposed to wavelength-selected light was found to be the most effective form of photoactivation and was chosen for implementation in the cell-based assays.

Following the completion of chemical and biological validation studies with the photoaffinity probe, systematic photoaffinity labeling experiments were initiated. A general workflow was designed, beginning with cell lysate preparation and proceeding through trifluoromethyl phenyldiazirine photoactivation, biotinylation, bead purification, and protein resolution via polyacrylamide gel electrophoresis; electrospray ionization

Fourier transform ion cyclotron resonance (ESI-FTIC) mass spectrometry could then be used to identify proteins bound to the crosslinked photophore (Figure 4.5). Implementing this workflow with MCF-7 breast cancer cells, anti-streptavidin immunoblotting was conducted against an aliquot of the biotinylated and bead purified lysate product to measure the efficacy of the labeling process; from these immunoblots, differential protein bands were detected between photoaffinity- and control-treated cell lysates (Figure 4.6). The optimized photoaffinity labeling experiment was conducted in duplicate and the resolved proteins from a single band (~21 kDa) were analyzed by ESI-FTIC mass spectrometry (Table 4.2). One protein, TMEM109, was identified from both independent experiments, suggesting against a nonspecific binding interaction with the photoaffinity probe. TMEM09 has been reported by others to be a transmembrane, ion-conducting channel capable of transporting both monovalent and divalent cations (11). Based on our findings, further studies were implemented to probe the importance of TMEM109 in C-6-mediated cancer cell death.

A reduction in TMEM109 protein expression does not confer protection from C-6-induced cell death in breast cancer cells

Before embarking upon experiments aimed at understanding TMEM109's role in C-6's mechanism of action, we first sought to characterize the expression of TMEM109 in a variety of cell types. Breast cancer cell lines, patient-derived malignant pleural effusion cells, a leukemia cell line, and untransformed mammary epithelial cells were assayed by immunoblot for the expression of TMEM109 (Figure 4.7A). All cell types evaluated were found to contain a band at approximately 25 kDa, with MDA-MB-231

Figure 4.5. The general workflow used for protein crosslinking experiments.

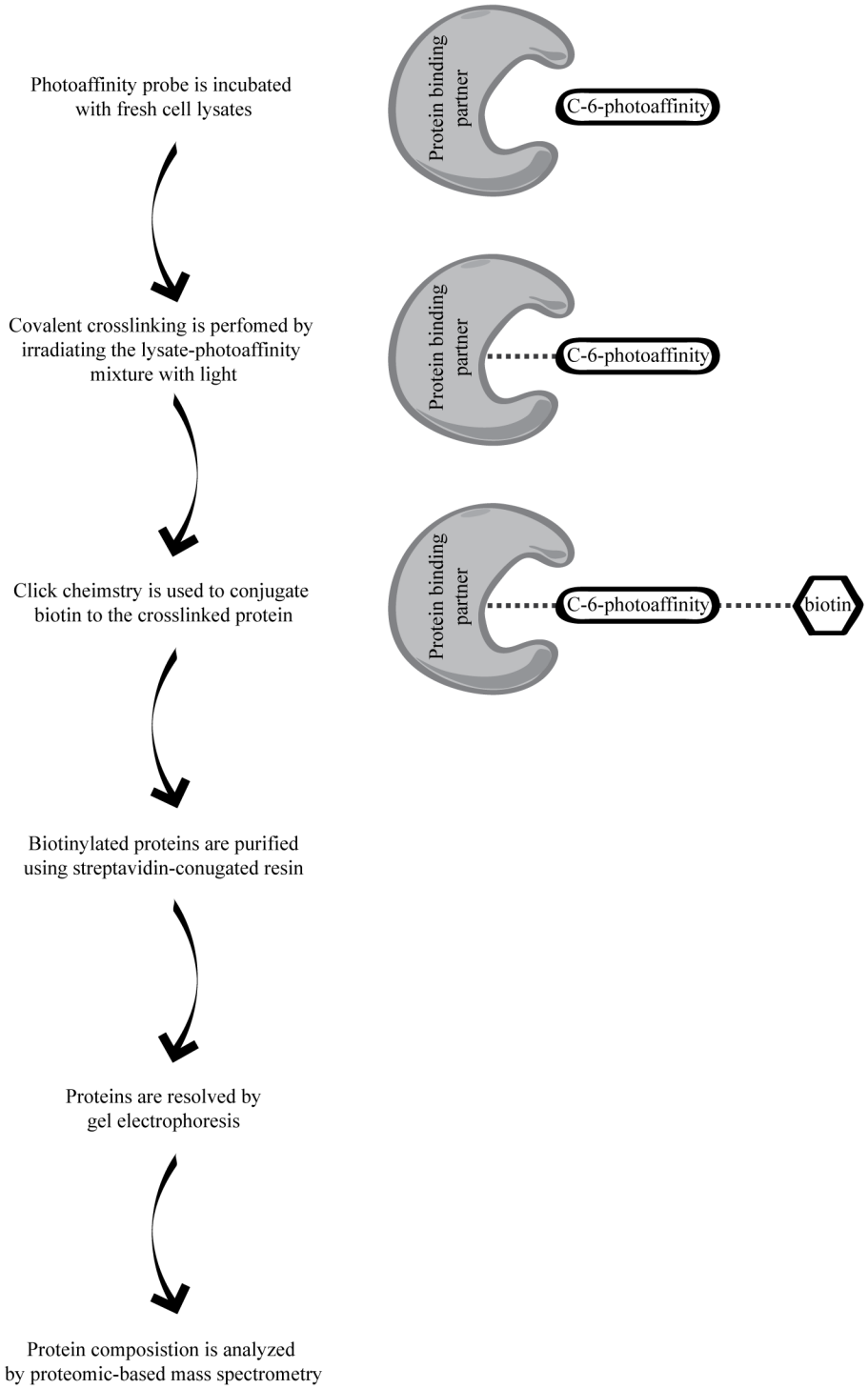
Photoaffinity probe is incubated with fresh cell lysates
Covalent crosslinking is perfomed by irradiating the lysate-photoaffinity mixture with light
Click cheimstry is used to conjugate biotin to the crosslinked protein
Biotinylated proteins are purified using streptavidin-conugated resin
Proteins are resolved by gel electrophoresis
Protein composistion is analyzed by proteomic-based mass spectrometry
Protein binding partner
C-6-photoaffinity
Protein binding partner
C-6-photoaffinity
Protein binding partner
C-6-photoaffinity
biotin

Figure 4.6. Photoaffinity crosslinking experiments result in differentially detected bands in control- versus C-6-photoaffinity-treated samples. (A) Example immunoblot results following crosslinking and protein purification of MCF-7 cell lysates. Arrows denote differentially detected bands. Anti-streptavidin antibody was used to detect crosslinked proteins. (B) Results of a competition crosslinking experiment using C-6 and its photoaffinity analog. Arrows denote differentially detected bands. Anti-streptavidin antibody was used to detect crosslinked proteins.

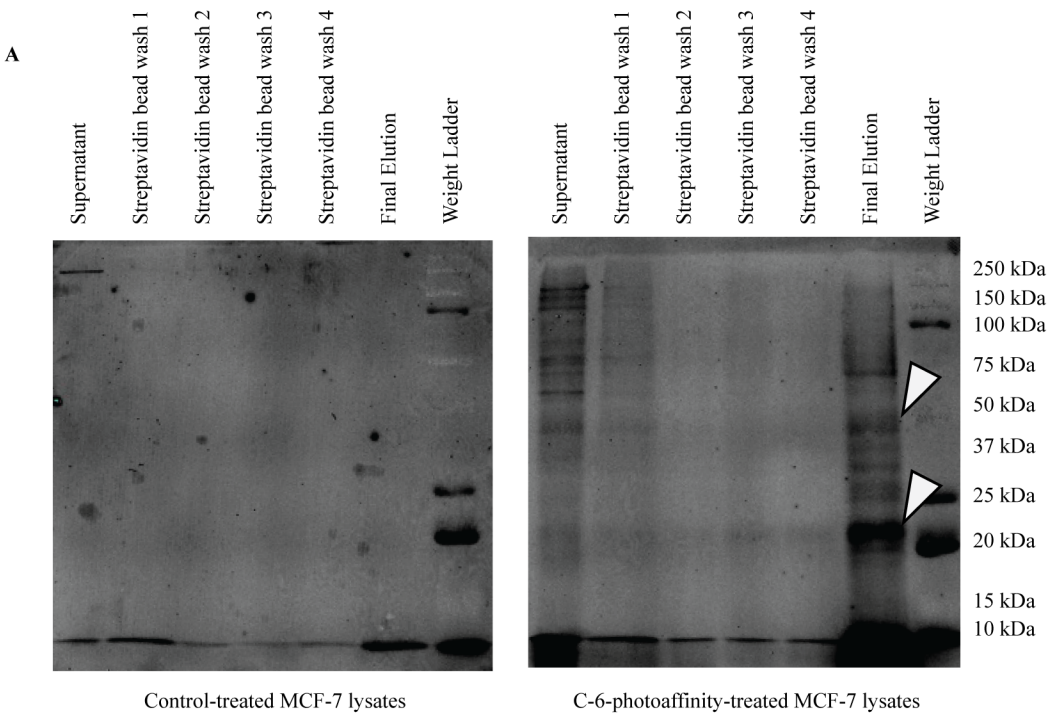
A
Supernatant
Streptavidin bead wash 1
Streptavidin bead wash 2
Streptavidin bead wash 3
Streptavidin bead wash 4
Final Elution
Weight Ladder
Supernatant
Streptavidin bead wash 1
Streptavidin bead wash 2
Streptavidin bead wash 3
Streptavidin bead wash 4
Final Elution
Weight Ladder
250 kDa
150 kDa
100 kDa
75 kDa
50 kDa
37 kDa
25 kDa
20 kDa
15 kDa
10 kDa
Control-treated MCF-7 lysates
C-6-photoaffinity-treated MCF-7 lysates

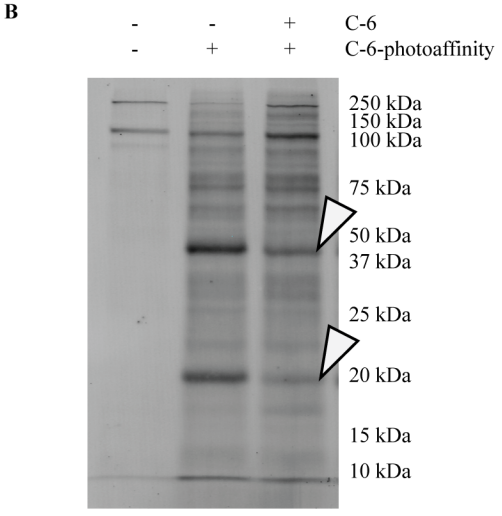
B
- - + C-6
- + + C-6-photoaffinity
250 kDa
150 kDa
100 kDa
75 kDa
50 kDa
37 kDa
25 kDa
20 kDa
15 kDa
10 kDa

Table 4.2. Results of C-6-photoaffinity proteomic analysis

Control-treated MCF-7 cell lysates	C-6-photoaffinity-treated MCF-7 cell lysates
Proteins identified	*Proteins identified*
keratin 1	epidermal cytokeratin 2
cytokeratin 9	keratin 1
unnamed protein product	unnamed protein product
epidermal cytokeratin 2	keratin, type I cytoskeletal 9
Keratin 5	Keratin 5
unnamed protein product	keratin type 16
putative	transmembrane protein 109 precursor
unnamed protein product	ubiquitin
KIAA1481 protein	diablo homolog, mitochondrial isoform 1 precursor
	histone H2A.Z
	thiol-specific antioxidant protein
	tumor protein D53
	mitochondrial ribosomal protein L7L12
	actin-related protein 2/3 complex subunit 5-like protein
	putative
	CD9 antigen
	prefoldin subunit 2
	Bax zeta
	DNA polymerase epsilon p17 subunit
	GTP-binding protein
	transgelin-2
	KIAA1481 protein
	unnamed protein product
	rasGAP-activating-like protein
	unnamed protein product
	KIAA0864 protein
	calmodulin
	cAMP-specific phosphodiesterase 4D

Figure 4.7. Assessment of TMEM109 expression. (A) TMEM109 expression as measured by immunoblotting in eight cells types. (B) Real-time polymerase chain reaction (RT-PCR) measurements of TMEM109 gene expression in MCF-7 cells transduced with one of four different shRNA-TMEM109-targeting lentiviruses. (C) Measurement of TMEM109 expression following lysate preparation with either standard or reducing (Red.) conditions.

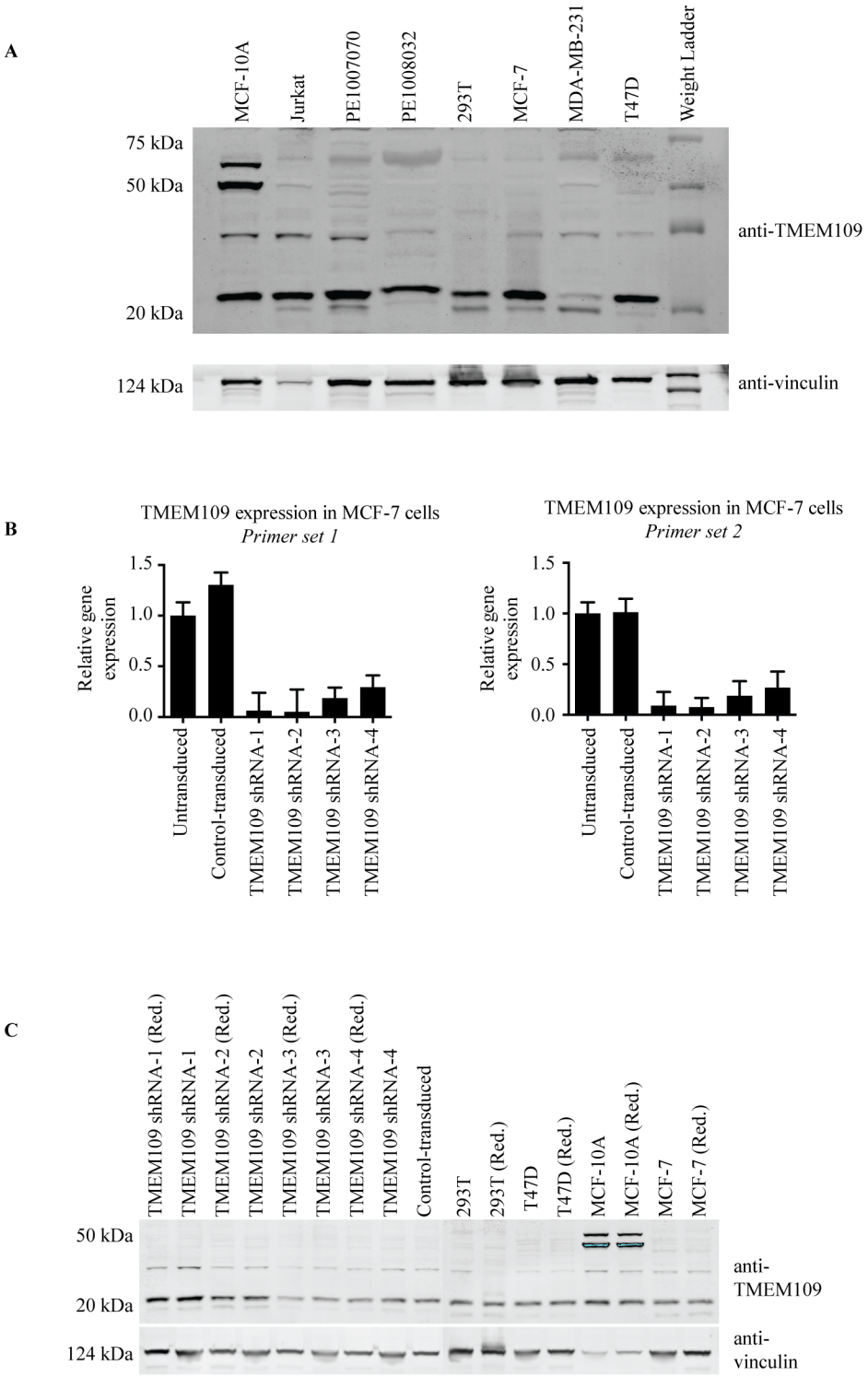
A
MCF-10A
Jurkat
PE1007070
PE1008032
293T
MCF-7
MDA-MB-231
T47D
Weight Ladder
75 kDa
50 kDa
20 kDa
anti-TMEM109
124 kDa
anti-vinculin
B
TMEM109 expression in MCF-7 cells
Primer set 1
Relative gene expression
1.5
1.0
0.5
0.0
Untransduced
Control-transduced
TMEM109 shRNA-1
TMEM109 shRNA-2
TMEM109 shRNA-3
TMEM109 shRNA-4
TMEM109 expression in MCF-7 cells
Primer set 2
C
TMEM109 shRNA-1 (Red.)
TMEM109 shRNA-1
TMEM109 shRNA-2 (Red.)
TMEM109 shRNA-2
TMEM109 shRNA-3 (Red.)
TMEM109 shRNA-3
TMEM109 shRNA-4 (Red.)
TMEM109 shRNA-4
Control-transduced
293T
293T (Red.)
T47D
T47D (Red.)
MCF-10A
MCF-10A (Red.)
MCF-7
MCF-7 (Red.)
50 kDa
20 kDa
anti-TMEM109
124 kDa
anti-vinculin

breast cancer cells displaying the lowest levels. Particularly interesting though was the observation that prominent, higher molecular weight bands reacting with the anti-TMEM109 antibody between 50 and 75 kDa were detected only in MCF-10A cells, which are C-6 insensitive. The results of these characterization studies suggested that TMEM109 was expressed ubiquitously in the cell types frequently employed in our studies of C-6 and also that the protein may function differently in C-6-insensitive cell types, perhaps providing an explanation for the small molecule's cancer-selective phenotype.

To understand the role of TMEM109 in C-6's mode of action, shRNA-mediated knockdown of protein expression in MCF-7 cells was conducted using a lentiviral delivery system; it was hypothesized that a reduction in the expression of the C-6's biological target would alter cellular sensitivity to the small molecule's cytotoxic effects. One control construct and four constructs targeting expression of TMEM109, each with antibiotic selection markers, were employed for the experiment; following transduction, antibiotic selection was conducted to select for those cells expressing the expression construct. Upon generation of the stably expressing lines, quantitative real-time polymerase chain reaction (RT-PCR) was performed to measure relative mRNA levels of TMEM109. Based on the results of two primer sets used against TMEM109, each of the four shRNA constructs significantly reduced the mRNA expression of the gene compared to untransduced and control-transduced MCF-7 cells (Figure 4.7B). Further analysis of protein expression knockdown efficiency by immunoblot revealed results consistent with the RT-PCR experiments and further indicated that the cells expressed lower levels of TMEM109 than the parental or control-transduced lines (Figure 4.7C). Using two of the four TMEM109-shRNA lines in addition to control-transduced and untransduced MCF-7

cells, 12-point dose response assays were conducted with C-6 to measure changes in cell viability resulting from C-6 treatment (Table 4.3). Unfortunately, no significant changes in the EC_{50} values between the four lines were observed. These data suggest that reductions in the expression of the protein TMEM109 do not alter C-6's efficacy in whole-cell assays.

Genetrap knockout of TMEM109 does not alter the cytotoxicity profile of C-6 in KBM-7 chronic myelogenous leukemia cells

Even while our shRNA experiments targeting expression of TMEM109 successfully reduced the levels of proteins, we also considered the possibility that residual protein, even at low levels, may be sufficient to produce the cytotoxic effects observed in cells treated with C-6. Therefore, we sought to incorporate knockout cells into our studies as a way to exhaustively explore the role of TMEM109 in C-6-mediated cancer cell death. The KBM-7 cells line was derived from a patient with chronic myelogenous leukemia and upon characterization, was found to be haploid with the exception of chromosome 8. As such, these cells are ideal for gene knockout and ablation studies since genes not residing on chromosome 8 exist as a single copy compared to a diploid system wherein at least two copies are present. Therefore, our labs acquired commercially available KBM-7 and genetrap-TMEM109 KBM-7 cells with which to test the effects of C-6. After conducting preliminary experiments to ensure that C-6 was effective against the parental KBM-7 line, a validation of the genetrap-TMEM109 KBM-7 cells was conducted by assessing TMEM109 protein levels by immunoblot (Figure 4.8A). After completion of these experiments, a 12-point dose

Table 4.3. Measurement of cell viability following C-6 treatment in shRNA-mediated TMEM109 knockdown MCF-7 cells

Cell type	EC_{50}
MCF-7	21 μM
Control-transduced MCF-7	20 μM
shRNA TMEM109-3	23 μM
shRNA TMEM109-4	21 μM

Figure 4.8. Genetrap-TMEM09 KBM-7 cells are not protected from C-6's cytotoxic effects compared to control KBM-7 cells. (A) KBM-7 and genetrap-TMEM109 KBM-7 cells were assessed for TMEM109 expression by immunoblotting. (B) Dose response analysis of C-6 against KBM-7 and genetrap-TMEM109 KBM-7 cells measuring changes in cell viability. Values represent the mean of three measurements and error bars represent the standard deviation. (C) Effects of 48 hour C-6-treatment as measured by propidium iodide staining and flow cytometry measurement. Values represent the mean of three measurements and error bars represent the standard error of the mean.

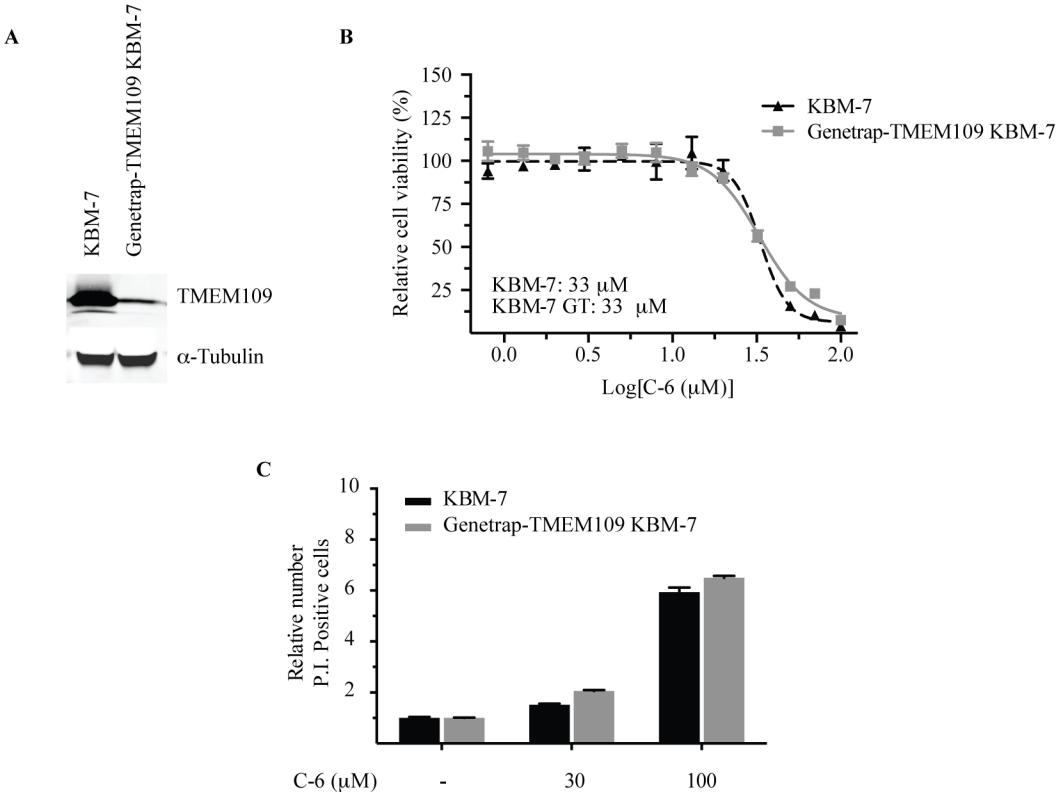
A
KBM-7
Genetrap-TMEM109 KBM-7
TMEM109
α-Tubulin
B
Relative cell viability (%)
150
125
100
75
50
25
KBM-7
Genetrap-TMEM109 KBM-7
KBM-7: 33 μM
KBM-7 GT: 33 μM
0.0
0.5
1.0
1.5
2.0
Log[C-6 (μM)]
C
Relative number
P.I. Positive cells
10
8
6
4
2
KBM-7
Genetrap-TMEM109 KBM-7
C-6 (μM)
-
30
100

response assay was conducted with C-6 to measure the effects of C-6 treatment on cell viability (Figure 4.8B). Additionally, cell viability was also measured by propidium iodide staining and flow cytometry in order to assess potential growth arrest phenotypes (Figure 4.8C). Unfortunately, as with the shRNA experiments, no significant difference was noted between the parental line and the genetrap-TMEM109 line. In all, these data fail to implicate TMEM109's direct involvement in C-6's mechanism of action; however, it is still possible that TMEM109 contributes to C-6's biological activity but its contribution is complex and beyond the readout of the assays used herein.

A haploid genetic screen was implemented to identify the biological target of C-6

Considering an alternative strategy to our affinity-based target identification approach, a genetic mutagenesis screen was designed using near-haploid KBM-7 cells to identify the target of C-6. Utilizing an approach reported by Brummelkamp and coworkers, the near-haploid cells were infected independently with retroviral and lentiviral genetrap constructs (12). Upon transduction, near-random viral integration of the genetrap construct into the genome produced clones with single or multiple gene disruptions. Importantly, since near-haploid cells were utilized, most genetrap integrations produced dominant phenotypes, an effect that could not be achieved in diploid systems. The genetrap-mutagenized cells were treated with C-6 for four weeks and surviving clones were analyzed for shared gene disruption features. It was expected that disruption of genes important for C-6's mechanism of action would produce a knockout effect and promote survival in the presence of C-6; the viral insertion sites of

surviving clones could then be analyzed and the null genes identified. However, after analyzing the clones of cells surviving C-6 treatment, no consistent trends were observed in viral integration patterns, suggesting the cells survived long-term C-6 treatment by adaptation to the treatment and not by a survival advantage imparted by a genetrap insertion.

Discussion

The data presented here details our efforts towards defining C-6's protein binding partners using photoaffinity labeling and functional genetic strategies. With the affinity-based strategy, analogs of the small molecule were generated and tested against untransformed and transformed mammary epithelial cells to assess their effects on cell viability before synthesizing a photophore-containing variant of C-6. This study was designed to better understand the relationship between C-6's structure and its biological activity and the results ultimately provided the necessary insight for photophore incorporation. After synthesizing the photoaffinity derivative, validation studies were conducted to ensure that the parent molecule and the analog modulated similar biological pathways. The results of dose response studies and experiments designed to measure endoplasmic reticulum stress, a characteristic feature of C-6's biological activity, suggested that the photoaffinity derivative elicited cellular phenotypes in a manner similar to C-6. As such, labeling experiments were initiated and the resulting crosslinked proteins analyzed by mass spectrometry. In two experimental replicates, a single protein, TMEM109, was detected in C-6-photoaffinity-treated samples but not control-treated samples. As such, experiments were designed to better understand the role of TMEM109

in C-6-mediated cancer cell death.

As a first step towards this goal, eight cell types including primary patient-derived malignant pleural effusion cells, breast cancer cell lines, and untransformed mammary epithelial cells were evaluated for endogenous TMEM109 protein expression by immunoblot; a band corresponding to ~23 kDa was detected in all samples with variation in relative levels observed between the different cell types. Next, an shRNA-mediated knockdown of TMEM109 was performed in MCF-7 cells to determine whether reduced protein expression could alter cellular responses to C-6. Unfortunately, TMEM109 knockdown did not afford a survival advantage against C-6 treatment and no differences were observed between shRNA-TMEM109, control-transduced, and untransduced lines. C-6 was also evaluated against genetrap-TMEM109 KBM-7 cells, but as with the shRNA-TMEM109 experiment, no difference in viability was observed when compared to control cells.

In all, our investigation into TMEM109's involvement in C-6's mechanism of action produced results that may support several hypotheses. While nonspecific-binding interactions can lead to false discoveries in photoaffinity labeling studies, TMEM109 was identified from two independent experiments, which suggests a preferential binding interaction with the protein. However, this interaction could be an off-target effect. That is, small molecule-protein binding may occur but the protein is ultimately uninvolved in the small molecule's mechanism of action. Alternative to this hypothesis is that TMEM109 does contribute to C-6's phenotype, but that other protein family members can carry out redundant functions and are also affected by the molecule. With this hypothesis, shRNA-mediated knockdown and genetrap knockout experiments would prove ineffective. Overall, the data suggest that C-6 does bind TMEM109, but the

experiments conducted do not distinguish between redundant protein effects and off-target binding, which ultimately confounds the results obtained.

Considering all aspects of our photoaffinity-based target identification strategy and the work as a whole, several modifications could be made to improve the success of future experiments implementing this strategy. First, an inactivated photoaffinity analog could be immensely useful as a control for delineating nonspecific interactions of the photoaffinity probe itself. Second, experimental reproduction will be helpful for identifying low-abundance proteins that may only appear as mass spectrometry hits in, for example, two out of every five experimental runs; considering this possibility, identifying trends over a larger data set could prove beneficial. Third, significant advancements have been made in the field of proteomic mass spectrometry analysis. Application of more advanced analysis techniques could reveal trends that are otherwise hidden using standard analysis techniques. Finally, the use of more sensitive instrumentation could allow for the identification of small molecule-protein complexes in total cell lysate. Omitting gel electrophoresis and trypsin digest steps would significantly expand the number of proteins analyzed and would also negate the requirement for band visualization, a step that limits detection to highly abundant proteins.

The data presented herein describe our work towards identifying the biological target of C-6. Considering C-6's unique, cancer-selective phenotype, identifying its binding partners is necessary to fully elucidate its mechanism of action. Although our results suggest that C-6 binds TMEM109, the experiments failed to identify its role in C-6-induced cancer cell death processes. Since TMEM109's endogenous function has not been clearly defined, further investigations into its role in normal cellular function could provide information useful for tailoring future experiments aimed at defining its

interaction with C-6.

Methods

Materials and methods for chemical synthesis

General considerations. Tetrahydrofuran (THF), dichloromethane (DCM), diethyl ether, and toluene were used from an alumina column solvent system (Innovative Technology, Inc.). Triethylamine (TEA) was distilled over calcium hydride. Dimethylformamide (DMF) was stored over activated 3Å molecular sieves. Unless otherwise noted all chemicals were purchased from Aldrich, Acros, TCI, EMD, or Mallinckrodt and used without further purification. Also, all reactions were performed under a nitrogen atmosphere unless otherwise noted. ^{1}H NMR spectra were obtained at 300 MHz, 400 MHz or 500 MHz using Varian spectrometers. ^{1}H chemical shifts are reported in ppm and referenced to $CHCl_3$ at 7.26 ppm, CD_2Cl_2 at 5.32 ppm, or acetone-D6 at 2.05 ppm. ^{13}C NMR spectra were obtained at 75 MHz, 100 MHz or 125 MHz using Varian spectrometers. ^{13}C chemical shifts are reported in ppm and referenced to $CHCl_3$ at 77.16 ppm, CD_2Cl_2 at 53.84 ppm, or acetone-D6 at 29.84 ppm. High resolution mass spectrometry (HRMS) data were obtained on a Waters LCP Premier XE instrument by ESI/TOF. Infrared (IR) spectra were recorded using a Thermo Nicolet FT-IR. All melting points (MP) are uncorrected and recorded on Thomas Hoover Unimelt capillary melting point apparatus. The following abbreviations are used: EtOAc (ethyl acetate), TLC (thin layer chromatography).

Preparation of C-6 and analogs 1-17. The general route used to access C-6 and analogs 1-17 has been reported previously (10).

Preparation of analog 21. A mixture of analog 18 (11 mg, 0.29 mmol, 1.0 equiv.), phenyl azide (8.7 mg, 0.73 mmol, 2.5 equiv.), $CuSO_4$ (0.3 mg, 0.02 mmol, 0.075 equiv.), and freshly prepared 1M sodium ascorbate (0.004 mmol, 0.15 eq.) were combined in 2 mL of a 1:3 H_2O:THF solution. The reaction was stirred for 12 hours at room temperature. THF was then removed by rotary evaporation, 5 mL of H_2O was added, and the product extracted with EtOAc (3 x 5 mL). The combined organic layers were dried over Na_2SO_4 and concentrated. The product was purified by silica gel flash chromatography (30:70 EtOAc:hexanes) to afford analog 21. Yield 76%.

Preparation of analog 22. For the synthesis of analog 22, 1-azido-2-(2-(2-chloroethoxy)ethoxy)ethane was first prepared according to a previously published procedure (13). A mixture of analog 18 (0.025 g, 0.073 mmol, 1.0 equiv.), 1-azido-2-(2-(2-chloroethoxy)ethoxy)ethane (0.0857 g) and K_2CO_3 (0.03014 g, 0.22 mmol, 3.0 eq.) in 1.5 mL of DMF was heated to 70 °C for 48 hours. After cooling, the mixture was diluted with NH_4Cl (10 mL) and extracted with EtOAc (2 x 10 mL), dried over Na_2SO_4, and concentrated. The product was purified by flash chromatography (30:70 EtOAc:hexanes) on silica gel to afford analog 22. Yield 28%.

Preparation of intermediate 4.1. 5-bromobenzene-1,3-diol was prepared following a previously published literature procedure (14). NaH (60% in mineral oil, 33mmol) was added to 50 mL of DMF and stirred under an N_2 atmosphere. The reaction was cooled to 0 °C and 5-bromobenzene-1,3-diol (3.1 g, 16.6 mmol, 1.0 equiv.) in 5 mL of DMF was added to the stirring mixture. The reaction was stirred for 20 minutes. To the mixture was added benzyl bromide (33 mmol, 2.0 equiv.). The reaction was allowed to warm to room temperature and stirring continued for 3 hours. The reaction was quenched with saturated ammonium chloride solution and diluted with diethyl ether. The

organic layer was dried and concentrated and the crude product purified by silica gel flash column chromatography (5:95 EtOAc:hexanes). Yield 91%.

Preparation of intermediate 4.2. Compound 4.2 was prepared following published literature procedure and purity assessed using ^{1}H NMR (15).

Preparation of intermediate 4.3. An oven-dried round bottom flask fitted with a magnetic stirbar and a rubber septum was charged with compound 4.1 (3.9 mmol, 3.3 equiv.). The flask was purged with N_2 and 10 mL of THF added via cannula. After the solid was allowed to dissolve, the flask was cooled to -78 °C. Dropwise while stirring, previously titrated *n*-BuLi (3.9 mmol, 3.3 equiv.) was slowly added. The reaction was stirred for 1 hour at -78 °C before a solution of compound 4.2 (310 mg, 1.3 mmol, 1.0 equiv.) in THF (10 mL) was added to the stirring mixture dropwise over 10 minutes. The reaction continued to stir at -78 °C for 2 hours. The reaction was then quenched with H_2O and allowed to slowly warm to room temperature. The product was extracted into EtOAc (2 x 10 mL), washed with brine (2 x 10 mL), dried over Na_2SO_4, and concentrated under reduced pressure. The product, compound 4.3, was purified using silica gel flash column chromatography and 30:70 acetone:hexanes. Yield 51%.

Preparation of intermediate 4.4. To a flask charged with compound 4.3 (353 mg, 0.7 mmol) in 20 mL of dry DCM, 1 drop of concentrated HCl was added and the reaction stirred at room temperature until TLC indicated consumption of the starting material. The mixture was then dried over Na_2SO_4, and concentrated. The final product was used immediately for the next step and was combined (210 mg, 0.4 mmol) with 10% Pd/C (0.08 mmol, 20 mol%) and 2.0 mL of MeOH. The flask was fitted with a balloon of H_2 and the reaction stirred for 12 hours. Then, the reaction mixture was passed through a plug of silica and concentrated to provide compound 4.4.

Preparation of intermediate 4.5. Propargyl bromide (26 mg, 0.2 mmol, 1.0 equiv.) was added to a stirring mixture of compound 4.4 (73 mg, 0.2 mmol, 1.0 equiv.), acetone (15 mL) and K_2CO_3 (183 mg, 1.3 mmol, 6.0 equiv.). The reaction was heated to reflux and stirred for 16 hours. Then, the mixture was allowed to cool to room temperature, filtered, and concentrated. The product was purified by silica gel flash column chromatography (30:70 EtOAc:hexanes). Yield 32%.

Preparation of intermediate 4.6. Before preparation of intermediate 4.6, 1,2-bis(2-iodoethoxy)ethane was first prepared following a previously published procedure (16). Then, compound 4.5 (13 mg, 0.03 mmol, 1.0 equiv.), 1,2-bis(2-iodoethoxy)ethane (130 mg, 0.3 mmol, 10.0 equiv.), and K_2CO_3 (49 mg, 0.3 mmol, 10.0 equiv.) were combined with acetone (5 mL) in a vial equipped with a magnetic stirbar. The reaction was heated to reflux and stirred for 18 hours when TLC indicated complete consumption of starting material. The mixture was filtered, concentrated, and purified using silica gel flash column chromatography (30:70 acetone:hexanes). Yield 97%.

Preparation of C-6-photoaffinity analog. The trifluoromethyl phenyldiazirine photophore was prepared in good yield following a previous report (17). Intermediate 4.6 (12.1 mg, 0.02 mmol, 1.0 equiv.), the freshly prepared trifluoromethyl phenyldiazirine photophore phenol (40 mg, 0.2 mmol, 10.0 equiv.), and K_2CO_3 (54 mg, 0.4 mmol, 20.0 equiv.) were combined with acetone (1 mL) in a vial equipped with a magnetic stirbar. The reaction was heated to reflux and stirred for 18 hours. The mixture was filtered, concentrated, and purified using silica gel flash column chromatography (30:70 acetone:hexanes). Yield >99%.

Preparation of analogs 23-26. Analogs 23-26 have been synthesized previously and their general routes reported (18).

Characterization of previously unreported compounds

Characterization of analog 7. TLC (30:70 EtOAc:hexanes) R_f=0.20; ^{1}H NMR (300 MHz, $CDCl_3$): δ 1.30 (s, 9H), 1.54 (d, *J* = 7.14 Hz, 3H), 3.74 (s, 6H), 4.00 (q, *J* = 7.28 Hz, 1H), 6.27-6.31 (m, 3H), 6.57 (s, 1H), 6.97 (*J* = 8.51, 2H), 7.09 (*J* = 8.51, 2H), 7.43 (*J* = 8.79, 2H), 7.68 (*J* = 8.79, 2H); ^{13}C NMR (75 MHz, $CDCl_3$): δ 21.8, 31.1, 35.2, 44.4, 55.3, 97.6, 106.0, 121.8, 126.1, 127.1, 128.5, 134.6, 136.4, 143.3, 148.7, 156.8, 160.8; IR: 548, 569, 625, 642, 696, 733, 754, 834, 924, 1018, 1042, 1086, 1112, 1158, 1203, 1223, 1291, 1339, 1397, 1427, 1459, 1510, 1594, 2837, 2963, 3256 cm^{-1}; HRMS $(M+Na)^+$: calcd. 476.1872, obsvd. 476.1870.

Characterization of analog 8. TLC (30:70 EtOAc:hexanes) R_f=0.24; ^{1}H NMR (300 MHz, $CDCl_3$): δ 1.55 (d, *J* = 7.14 Hz, 3H); 1.63 (s, 1H), 3.74 (s, 6H), 4.01 (q, *J* = 7.26 Hz, 1H), 6.26-6.30 (m, 2H), 6.74 (s, 1H), 6.98 (d, *J* = 8.64 Hz, 2H), 7.13 (d, *J* = 8.37 Hz, 2H), 7.89 (d, *J* = 9.06 Hz, 2H), 9.06 (d, *J* = 8.27 Hz, 2H); ^{13}C NMR (75 MHz, $CDCl_3$): δ 21.6, 44.4, 55.4, 97.5, 106.1, 122.8, 124.4, 128.7, 128.9, 133.4, 144.6, 144.7, 148.4, 150.3, 160.9; IR: 552, 607, 667, 684, 737, 853, 926, 1018, 1090, 1155, 1204, 1311, 1348, 1458, 1530, 1594, 2934, 2966, 3265 cm^{-1}; HRMS $(M+Na)^+$: calcd. 465.1096, obsvd. 465.1082.

Characterization of analog 9. TLC (30:70 EtOAc:hexanes) R_f=0.22; ^{1}H NMR (300 MHz, $CDCl_3$): δ 1.54 (d, *J* = 7.14 Hz, 3H), 2.38 (s, 3H), 3.74 (s, 6H), 3.99 (q, *J* = 7.26 Hz, 1H), 6.29 (s, 3H), 6.58 (s, 1H), 6.95 (d, *J* = 8.65 Hz, 2H), 7.08 (d, *J* = 8.37 Hz, 2H), 7.21 (d, *J* = 7.96 Hz, 2H), 7.63 (d, *J* = 8.37 Hz, 2H); ^{13}C NMR (75 MHz, $CDCl_3$): δ 21.7, 21.8, 44.4, 54.4, 97.7, 106.1, 122.1, 127.4, 128.5, 128.5, 129.8, 134.5, 136.3, 143.4, 143.9, 148.7, 160.8; IR: 544, 561, 667, 693, 811, 835, 912, 1042, 1068, 1090, 1155, 1204, 1290, 1324, 1397, 1427, 1456, 1508, 1593, 3232 cm^{-1}; HRMS $(M+Na)^+$: calcd.

434.1402, obsvd. 434.1409.

Characterization of analog 10. TLC (30:70 EtOAc:hexanes) R_f=0.20; ^{1}H NMR (300 MHz, $CDCl_3$): δ 1.55 (d, J = 7.14 Hz, 3H), 1.60 (s, 1H), 3.82 (s, 1H), 3.74 (s, 6H), 4.00 (q, J = 7.26 Hz, 1H), 6.28 (s, 2H), 6.58 (s, 1H), 6.94 (2, 1H), 6.97 (s, 1H), 7.07-7.12 (m, 4H), 7.47 (q, J = 3.98 Hz, 2H); ^{13}C NMR (75 MHz, $CDCl_3$): δ 21.7, 44.4, 57.4, 97.6, 106.1, 116.4 (d, J_{CF} = 22.5), 122.4, 128.7, 130.0, 130.2, 134.1, 135.2, 143.9, 148.6, 160.9, 163.6, 167; IR: 542, 559, 637, 668, 694, 709, 834, 924, 1018, 1041, 1089, 1149, 1203, 1236, 1291, 1340, 1395, 1427, 1456, 1493, 1508, 1590, 2967, 3256 cm^{-1}; HRMS $(M+Na)^+$: calcd. 438.1151, obsvd. 438.1150.

Characterization of analog 11. TLC (30:70 EtOAc:hexanes) R_f=0.20; ^{1}H NMR (300 MHz, $CDCl_3$): δ 1.54 (d, J = 7.14 Hz, 3H), 3.74 (s, 6H), 3.82 (s, 3H), 3.99 (q, J = 7.26 Hz, 1H), 6.29 (s, 3H), 6.59 (s, 1H), 6.88 (d, J = 9.06 Hz, 2H), 6.96 (d, J = 8.72 Hz, 2H), 7.09 (d, J = 8.39 Hz, 2H), 7.68 (d, J = 9.06 Hz, 2H); ^{13}C NMR (75 MHz, $CDCl_3$): δ 21.8, 44.4, 54.4, 55.7, 97.7, 106.1, 114.3, 122.1, 128.5, 129.5, 130.8, 134.6, 143.4, 148.7, 160.8, 163.2; IR: 549, 565, 667, 835, 1092, 1143, 1260, 1336, 1393, 1427, 1456, 1497, 1594, 2869, 2988, 3231 cm^{-1}; HRMS $(M+Na)^+$: calcd. 450.1351, obsvd. 450.1360.

Characterization of analog 12. TLC (30:70 EtOAc:hexanes) R_f=0.20; ^{1}H NMR (300 MHz, $CDCl_3$): δ 1.48 (d, J = 7.00 Hz, 3H), 2.86 (s, 6H), 3.71 (s, 6H), 3.92 (q, J = 7.14 Hz, 1H), 6.23-6.27 (m, 3H), 6.76 (s, 1H), 6.82 (d, J = 8.65 Hz, 2H), 6.97 (d, J = 8.65 Hz, 2H), 7.17 (d, J = 8.69 Hz, 1H), 7.42 (d, J = 8.41 Hz, 1H), 7.53 (d, J = 8.55 Hz, 1H), 8.16 (d, J = 8.28 Hz, 1H), 8.47 (d, J = 8.64 Hz, 1H), 8.49 (d, J = 8.51 Hz, 1H); ^{13}C NMR (75 MHz, $CDCl_3$): δ 21.7, 44.4, 45.5, 55.3, 97.7, 105.9, 115.3, 118.6, 121.9, 123.2, 128.4, 128.6, 129.7, 129.9, 130.4, 130.9, 134.4, 134.5, 143.3, 148.6, 152.1, 160.8; IR: 538, 572, 622, 682, 696, 731, 788, 836911, 1018, 1043, 1143, 1202, 1231, 1316, 1392, 1427, 1454,

1509, 1592, 2788, 2834, 2937, 3272 cm^{-1}; HRMS $(M+Na)^+$: calcd. 513.1824, obsvd. 513.1833.

Characterization of analog 14. TLC (30:70 EtOAc:hexanes) R_f=0.20; ^1H NMR (300 MHz, $CDCl_3$): δ 1.55 (d, *J* = 7.14 Hz, 3H), 3.74 (s, 6H), 4.01(q, *J* = 7.00 Hz, 1H), 6.29 (s, 3H), 6.56 (s, 1H), 6.96 (d, *J* = 8.51 Hz, 2H), 7.11 (d, *J* = 8.37 Hz, 2H), 7.39 (d, *J* = 8.78 Hz, 2H), 7.66 (d, *J* = 7.66 Hz, 2H); ^{13}C NMR (75 MHz $CDCl_3$): δ 21.7, 44.4, 55.3, 97.6, 106.1, 122.4, 128.7, 128.8, 129.4, 133.9, 137.6, 139.6, 144.0, 148.5, 160.8; IR: 553, 616, 667, 696, 730, 754, 827, 910, 1014, 1041, 1092, 1158, 1203, 1288, 1340, 1396, 1427, 1457, 1509, 1593, 2836, 2965, 3259 cm^{-1}; HRMS $(M)^+$: calcd. 454.0586, obsvd. 454.0862.

Characterization of analog 15. TLC (30:70 EtOAc:hexanes) R_f=0.20; ^1H NMR (300 MHz, $CDCl_3$): δ 1.54 (d, *J* = 7.14 Hz, 3H), 3.70 (s, 6H), 3.96 (q, *J* = 7.26 Hz, 1H), 6.27 (s, 3H), 6.90 (s, 1H), 6.97-7.07 (m, 4H), 7.54-7.65 (m, 2H), 7.73 (d, *J* = 1.92 Hz, 1H), 7.76 (d, *J* = 1.79 Hz, 2H), 7.85-7.89 (m, 3H), 8.33 (s, 1H); ^{13}C NMR (75 MHz $CDCl_3$): δ 21.7, 44.3, 55.3, 97.8, 106.0, 122.2, 122.4, 127.6, 128.0, 128.6, 128.9, 129.0, 129.4, 129.5, 132.1, 134.3, 135.0, 136.1, 143.6, 148.6, 160.8; IR: 547, 615, 644, 657, 667, 696, 747, 816, 857, 923, 952, 1018, 1041, 1047, 1131, 1154, 1202, 1319, 1339, 1393, 1428, 1457, 1509, 1593, 2968, 3261 cm^{-1}; HRMS $(M+Na)^+$: calcd. 470.1402, obsvd. 470.1407.

Characterization of analog 16. TLC (30:70 EtOAc:hexanes) R_f=0.22; ^1H NMR (300 MHz, $CDCl_3$): δ 1.54 (d, *J* = 7.14 Hz, 3H), 2.38 (s, 3H), 3.74 (s, 6H), 3.99 (q, *J* = 7.26 Hz, 1H), 6.29 (s, 3H), 6.58 (s, 1H), 6.95 (d, *J* = 8.65 Hz, 2H), 7.08 (d, *J* = 8.37 Hz, 2H), 7.21 (d, *J* = 7.96 Hz, 2H), 7.63 (d, *J* = 8.37 Hz, 2H); ^{13}C NMR (75 MHz, $CDCl_3$): δ 21.7, 21.8, 44.4, 54.4, 97.7, 106.1, 122.1, 127.4, 128.5, 128.5, 129.8, 134.5, 136.3, 143.4,

143.9, 148.7, 160.8; IR: 544, 561, 667, 693, 811, 835, 912, 1042, 1068, 1090, 1155, 1204, 1290, 1324, 1397, 1427, 1456, 1508, 1593, 3232 cm^{-1}; HRMS $(M+Na)^+$: calcd. 434.1402, obsvd. 434.1409.

Characterization of analog 17. TLC (30:70 EtOAc:Hexanes) R_f=0.32; ^1H NMR (300 MHz, $CDCl_3$): δ 1.55 (d, *J* = 7.14 Hz, 3H), 3.74 (s, 6H), 4.00 (q, *J* = 7.26 Hz, 1H), 6.28 (s, 3H), 6.61 (s, 1H), 6.96 (d, *J* = 8.52 Hz, 2H), 7.03 (d, *J* = 8.92 Hz, 2H), 7.10 (d, *J* = 8.37 Hz, 2H), 7.70, (d, *J* = 8.92 Hz, 2H); ^{13}C NMR (75 MHz, $CDCl_3$): δ 21.8, 44.4, 55.4, 97.6, 106.1, 119.5, 122.4, 128.6, 129.3, 134.1, 135.3, 143.8, 145.1, 148.6, 160.8; IR: 555, 668, 714, 832, 924, 1018, 1042, 1090, 1127, 1158, 1203, 1222, 1285, 1341, 1395, 1427, 1459, 1490, 1509, 1581, 2099, 2128, 2929, 2963, 3255 cm^{-1}.

Characterization of analog 21. TLC (30:70 EtOAc:hexanes) R_f=0.39; ^1H NMR (300 MHz, $CDCl_3$): δ 1.50 (s, 9H), 1.58 (d, *J* = 7.14 Hz, 3H), 3.76 (s, 3H), 4.03 (g, *J* = 7.26 Hz, 1H), 5.23 (s, 2H), 6.39-6.45 (m, 4H), 7.14 (d, *J* = 8.31 Hz, 2H), 7.25 (d, *J* = 9.31 Hz, 2H), 7.43-7.46 (m, 1H), 7.53 (t, *J* = 7.81 Hz, 2H), 7.72 (t, *J* = 7.81 Hz, 2H), 7.99 (s, 1H); ^{13}C NMR (75 MHz, $CDCl_3$): δ 21.5, 28.5, 44.5, 55.4, 62.1, 98.6, 106.7, 106.8, 118.8, 120.7, 121.0, 128.2, 128.9, 129.9, 136.5, 137.1, 140.8, 145.1, 149.3, 152.9, 159.4, 160.9; IR: 667, 1049, 1159, 1233, 1456, 1464, 1472, 1506, 1521, 1539, 1558, 1595, 1615, 1652, 1683, 1699, 1716, 1733, 2932, 2970, 3331 cm^{-1}; HRMS $(M)^+$: calcd. 523.2321, obsvd. 523.2319.

Characterization of analog 22. TLC (30:70 EtOAc:hexanes) R_f=0.15; ^1H NMR (500 MHz, $CDCl_3$) δ: 1.51 (s, 9H), 1.50 (d, *J* = 7.14, 3H), 3.60-3.64 (m, 2H), 3.68-3.77 (m, 9H) 3.81-3.84 (m, 2H), 4.00 (q, *J* = 7.26, 1H), 4.04-4.07 (m, 2H), 6.30 (m, 1H), 6.36 (m, 2H), 6.40 (s, 1H), 7.13 (d, J = 8.3 Hz, 2H), 7.25 (d, J = 7.78 Hz, 4H); ^{13}C NMR (100 MHz, $CDCl_3$): δ 21.9, 28.5, 42.9, 44.9, 44.5, 55.4, 67.4, 69.9, 70.8, 70.9, 71.6, 98.4,

106.4, 106.6, 118.8, 128.1, 136.4, 140.9, 160.0, 160.7; IR: 555, 617, 668, 714, 832, 924, 1042, 1090, 1127, 1158, 1203, 1285, 1341, 1459, 1490, 1509, 1588, 2099, 2128, 2930, 2972, 3321 cm^{-1}.

Characterization of intermediate 4.1. TLC (5:95 EtOAc:Hexanes) R_f=0.33; MP=58-60 °C; ^{1}H NMR (300 MHz, $CDCl_3$): δ 5.00 (s, 4H), 6.54 (t, *J* = 2.33 Hz, 1H), 6.77 (d, *J* = 2.19 Hz, 2H), 7.32-7.41 (m, 10H); ^{13}C NMR (75 MHz, $CDCl_3$): δ 70.4, 101.5, 111.2, 123.1, 127.7, 128.3, 128.8, 136.4, 160.5; IR: 630, 674, 695, 733, 816, 907, 1026, 1051, 1080, 1151, 1212, 1278, 1328, 1377, 1436, 1497, 1573, 1594, 2870, 3031 cm^{-1}; HRMS $(M)^+$: calcd. 369.0490, obsvd. 369.0492.

Characterization of intermediate 4.3. TLC (20:80 EtOAc:hexanes) R_f=0.11; ^{1}H NMR (300 MHz, $CDCl_3$): δ 1.49 (s, 9H), 1.83 (s, 3H), 2.43 (s, 1H), 4.93 (s, 4H), 6.47 (s, 1H), 6.63-6.66 (m, 3H), 7.20-7.37 (m, 14H); ^{13}C NMR (75 MHz, $CDCl_3$): δ 28.5, 30.9, 70.2, 76.1, 80.7, 100.4, 105.6, 118.3, 126.6, 127.8, 128.1, 128.7, 136.9, 137.3, 142.4, 150.8, 152.9, 159.8; IR: 647, 667, 696, 732, 836, 907, 1027, 1050, 1105, 1151, 1233, 1289, 1315, 1367, 1404, 1436, 1453, 1498, 1520, 1592, 1652, 1700, 2929, 2975, 3032, 3331 cm^{-1}; HRMS $(M+Na)^+$: calcd. 548.2413, obsvd. 548.2411.

Characterization of intermediate 4.4. TLC (30:70 EtOAc:Hexanes) R_f=0.17; MP=112-114 °C; ^{1}H NMR (300 MHz, Acetone-d_6): δ 1.47 (s, 9H), 1.52 (d, *J* = 7.3 Hz, 3H), 3.94 (q, *J* = 7.1, 1H), 6.15-6.16 (m, 1H), 6.21 (m, 2H), 7.15 (d, *J* = 8.6 Hz, 2H), 7.45 (d, *J* = 8.6 Hz, 2H), 8.0 (s, 2H), 8.27 (bs, 1H); ^{13}C NMR (75 MHz, Acetone-d_6): δ 22.1, 28.5, 44.8, 79.8, 101.2, 107.0, 119.1, 128.5, 138.5, 141.3, 150.2, 153.8, 159.3; IR: 651, 667, 695, 773, 835, 921, 990, 1017, 1064, 1098, 1156, 1249, 1312, 1367, 1392, 1411, 1450, 1520, 1599, 1694, 2874, 2931, 2975, 3325 cm^{-1}; HRMS $(M+Na)^+$: calcd. 352.1525, obsvd. 352.1526.

Characterization of intermediate 4.5. TLC (30:70 EtOAc:hexanes) R_f=0.31; ^{1}H NMR (400 MHz, $CDCl_3$): δ 1.51 (s, 9H), 1.55 (d, *J* = 7.1 Hz, 3H), 2.49-2.50 (m, 1H), 3.98 (q, *J* = 7.1 Hz, 1H), 4.60 (d, *J* = 2.3 Hz, 2H), 5.17 (bs, 1H), 6.27-6.31 (m, 2H), 6.42-6.45 (m, 2H), 7.10-7.16 (m, 2H), 7.23-7.26 (m, 2H); ^{13}C NMR (125 MHz, $CDCl_3$): δ 21.7, 28.5, 44.2, 55.94, 75.7, 78.6, 80.72, 99.9, 107.2, 108.2, 119.0, 128.2, 136.4, 140.8, 149.5, 156.7, 158.9, 173.2; IR: 648, 667, 695, 731, 774, 834, 906, 963, 1016, 1044, 1155, 1236, 1314, 1367, 1392, 1410, 1455, 1521, 1595, 1695, 2928, 2972, 3289 cm^{-1}; HRMS $(M+Na)^+$: calcd. 390.1681, obsvd. 390.1679.

Characterization of intermediate 4.6. TLC (30:70 EtOAc:hexanes) R_f=0.30; ^{1}H NMR (300 MHz, $CDCl_3$): δ 1.50 (s, 9H), 1.56 (d, *J* = 7.1 Hz, 3H), 2.50 (t, *J* = 2.3 Hz, 1H), 3.25 (t, *J* = 6.7 Hz, 2H), 3.65-3.85 (m, 8H), 3.97-4.08 (m, 3H), 4.61 (d, *J* = 2.3 Hz, 2H), 6.36-6.44 (m, 4H), 7.12 (d, *J* = 8.6 Hz, 2H), 7.25 (d, *J* = 6.7 Hz, 2H); ^{13}C NMR (75 MHz, $CDCl_3$): δ 3.1, 21.9, 28.5, 44.4, 56.0, 67.5, 70.0, 70.4, 71.0, 72.2, 75.7, 78.7, 80.6, 99.4, 107.2, 107.7, 118.9, 128.2, 136.5, 140.8, 149.2, 153.0, 158.7, 160.0; IR: 553, 625, 667, 701, 749, 781, 824, 979, 1035, 1149, 1204, 1362, 1456, 1506, 1538, 2921, 3375 cm^{-1}; HRMS $(M)^+$: calcd. 632.1485, obsvd. 632.1487.

Characterization of C-6-photoaffinity analog. TLC (30:70 acetone:hexanes) R_f=0.30; ^{1}H NMR (300 MHz, $CDCl_3$): δ 1.50 (s, 9H), 1.56 (d, *J* = 7.1 Hz, 3H), 2.49 (t, *J* = 2.7 Hz, 1H), 3.73 (s, 4H), 3.80-3.87 (m, 4H), 3.96-4.12 (m, 5H), 4.60 (d, *J* = 2.3 Hz, 2H), 6.36-6.43 (m, 4H), 6.71-6.78 (m, 2H), 6.91-6.93 (m, 1H), 7.10-7.13 (m, 2H), 7.23-7.29 (m, 2H); ^{13}C NMR (100 MHz, $CDCl_3$): δ 21.9, 28.5, 44.5, 56.0, 67.5, 67.8, 69.8, 70.0, 71.0, 71.1, 75.6, 78.7, 80.5, 99.4, 107.2, 107.7, 113.3, 115.9, 118.8, 119.1, 128.2, 130.2, 130.7, 136.5, 140.8, 149.2, 153.0, 158.7, 159.2, 160.0; IR: 553, 623, 674, 699, 781, 831, 915, 993, 1069, 1149, 1203, 1361, 1442, 1471, 1506, 1539, 1558, 1590, 1635,

1760, 1733, 2950, 3341 cm^{-1}; HRMS $(M+Na)^+$: calcd. 706.2716, obsvd. 706.2716.

Materials and methods for biological studies

General considerations. General methods for the biological studies presented herein have been reported previously (9, 10).

Photoaffinity labeling studies. To prepare the buffer for photoaffinity labeling, radioimmunoprecipitation assay (RIPA) buffer was made using 50 mM Tris HCl, 150 mM NaCl, 0.1 % sodium dodecyl sulfate (SDS), 0.5 % sodium deoxycholate, 1% Triton X100; an aliquot containing protease and phosphatase inhibitor cocktails and DTT was freshly prepared prior to each experiment. Release buffer was prepared as follows: 2% SDS, 30 mM Biotin, 100 mM NaCl, 6 M Urea, 2 M Thiourea, 1x Phosphate buffered saline (PBS). $CuSO_4$ solution was prepared as follows: 0.01 M $CuSO_4$ pentahydrate and 0.1 M sodium ascorbate in dH_20.

Streptavidin-conjugated Sepharose beads were obtained from GE Healthcare (Pittsburg, PA, USA). Endogenously biotinylated proteins were removed prior to the photoaffinity experiment using 75 μL of bead slurry/2 mg protein. For each condition to be examined, 150 μL bead slurry/1 mg protein was utilized. Before use, the beads were washed 4 x 300 μL of 1x PBS, centrifuging the beads at 50g for 30 seconds between each wash. After the final wash, the beads were kept on ice until use.

To prepare cell lysates, the media was decanted from a 10-cm plate of 70-80% confluent MCF-7 cells and the cells washed with 1x PBS. To the plate, 1 mL of cold 1x PBS was added and the cells scraped off the plate. The cell lysates were stored on ice throughout the remaining procedure. The suspension was aspirated and transferred to a

microcentrifuge tube and the cells pelleted for 3 minutes at 3000 RPM at 4 °C. The liquid was aspirated from the pellet and 50 μL of cold RIPA buffer was added. The tube was vortexed until the pellet loosened then the lysates were sonicated for 20 seconds to ensure complete disruption of the cell membrane. The lysates were pelleted again for 3 minutes at 3000 RPM at 4 °C. The soluble fraction was used for the remaining procedure. A BCA assay was used to determine the concentration of protein and 50 μL of 20 μg/μL MCF-7 lysate was used for each condition to be examined in the photoaffinity experiment.

Photoactivation and click chemistry was conducted as follows: The appropriate amount of photoaffinity probe or DMSO was added to each tube/condition (generally between 100 and 500 μM). The tube was vortexed to mix well and then incubated on ice for 5 minutes. Using the EXFO light source, each tube was irradiated for 2 minutes at 4 cm distance. The corresponding amount of biotin-azide derivative (at 100 μM concentration in DMSO) was added to the appropriate tubes and the tube vortexed to mix. The freshly prepared copper master mix was added to the tube such that the final ratio was 100:100:1:10 of alkyne:azide:$CuSO_4$:sodium ascorbate. The tube was again vortexed then incubated at 36 ºC. After 10 minutes, the tubes were vortexed again. After an additional 15 minutes incubating at 36 ºC, 0.5 M EDTA was added to quench the reaction such that there was 1:1 copper:EDTA. The lysates were then filtered through a 7k Zeba spin column according to the manufacturer's protocol.

Using washed streptavidin beads, the protein lysate was added to the beads and diluted with 1 x PBS such that there was ~1 mg protein/150 μL beads/400 μL total liquid volume. The suspension was placed on ice and rocked slowly for 30 minutes. The beads were then pelleted at 50 RCF for 30 seconds and the supernatant transferred to a new

tube. The beads were then washed as follows, pelleting the beads between washes: 1 x PBS (100 μL), 1 x PBS (100 μL), RIPA buffer (50 μL), RIPA buffer (50 μL), Release buffer (50 μL). To the supernatant and each wash was added 4x Laemmli load buffer (3 volumes protein solution :1 volume 4x Laemmli buffer). The samples were boiled at 95 ºC for 5 minutes then stored at -20 ºC until resolution by gel electrophoresis.

Gel electrophoresis and immunoblotting was carried out as follows: Generally, experiments were conducted using 10%, 1.5 mm hand-cast polyacrylamide gels with 4% stacking. For samples to be submitted for mass spectrometry analysis, precast BioRad gradient gels (4-15%, 1.0 mm) were used. After electrophoresis, proteins were transferred to MilliPore low fluorescence membranes using a wet transfer system at 95V for 90 minutes on ice. The membranes were washed with TBS and blocked with Odyssey blocking buffer for 1 hour at room temperature. After blocking, the membranes were probed with Streptavidin IRDye 800CW (1:2000) in Odyssey blocking buffer for 1 hour at room temperature. The membranes were washed with TBST and imaged using the Li-Cor odyssey imaging system.

Generation of shRNA TMEM109 knockdown cell lines by lentiviral transduction

shRNA constructs TMEM109 expression and a control construct were obtained from GE Healthcare Dharmacon (Lafayette, Colorado, USA). High titer lentivirus was produced as described previously; MCF-7 cells were transduced at an MOI of 10. Antibiotic selection was conducted for 5 days post-transduction and selection was validated by GFP analysis and flow cytometry (19). Immunoblot measurements of

TMEM109 expression were conducted using an anti-TMEM109 antibody from Sigma Aldrich.

RT-PCR primers

Two primer sets were used for RT-PCR analysis of TMEM109 expression. Set 1: 5'-TTTGGTGGCGCGTTTCAGCG-3' and 5'-ATTCAGCAGCTGTGCGGCGA-3'; Set 2: 5'-AGGCCGGCTAGTCTCCGAGC-3' and 5'-GGCTGCCATGACTGGGTCTTTCT-3'. GAPDH was used as an internal control: 5'-AAATTCCATGGCACCGTC-3'and 5'-GATGGTGATGGGATTTCCA-3'. RT-PCR was conducted as described previously (10).

KBM-7 haploid cell studies

KBM-7 and genetrap-TMEM109 KBM-7 cells were obtained from Haplogen (Vienna, Austria). Cells were cultured in suspension flasks in IMDM containing 10% FBS with penicillin and streptomycin antibiotics. Retroviral genetrap constructs were generously provided by Thijn Brummelkamp at the Netherlands Cancer Institute and the details of their construction have been previously reported (12).

References

1. Strittmatter SM (2014) Overcoming drug development bottlenecks with repurposing: old drugs learn new tricks. *Nat Med* 20(6):590-591.

2. Lomenick B, Olsen RW, & Huang J (2010) Identification of direct protein targets of small molecules. *ACS Chem Biol* 6(1):34-46.

3. Wang S, Sim TB, Kim Y-S, & Chang Y-T (2004) Tools for target identification and validation. *Curr Opin Chem Biol* 8(4):371-377.

4. Cong F, Cheung AK, & Huang S-MA (2012) Chemical genetics–based target identification in drug discovery. *Annu Rev Pharmacol Toxicol* 52(1):57-78.

5. Leslie BJ & Hergenrother PJ (2008) Identification of the cellular targets of bioactive small organic molecules using affinity reagents. *Chem Soc Rev* 37(7):1347-1360.

6. Lamb J*, et al.* (2006) The Connectivity Map: using gene-expression signatures to connect small molecules, genes, and disease. *Science* 313(5795):1929-1935.

7. Lamb J (2007) The Connectivity Map: a new tool for biomedical research. *Nat Rev Cancer* 7(1):54-60.

8. Schenone M, Dancik V, Wagner BK, & Clemons PA (2013) Target identification and mechanism of action in chemical biology and drug discovery. *Nat Chem Biol* 9(4):232-240.

9. Gligorich K*, et al.* (2013) Development of a screen to identify selective small molecules active against patient-derived metastatic and chemoresistant breast cancer cells. *Breast Cancer Res* 15(4):R58.

10. Vaden RM, Gligorich KM, Jana R, Sigman MS, & Welm BE (2014) The small molecule C-6 is selectively cytotoxic against breast cancer cells and its biological action is characterized by mitochondrial defects and endoplasmic reticulum stress. *Breast Cancer Res* (DOI: 10.1186/s13058-014-0472-0).

11. Venturi E*, et al.* (2011) Mitsugumin 23 forms a massive bowl-shaped assembly and cation-conducting channel. *Biochemistry* 50(13):2623-2632.

12. Carette JE*, et al.* (2009) Haploid genetic screens in human cells identify host factors used by pathogens. *Science* 326(5957):1231-1235.

13. Amaral SP, Fernandez-Villamarin M, Correa J, Riguera R, & Fernandez-Megia E (2011) Efficient multigram synthesis of the repeating unit of gallic acid-triethylene glycol dendrimers. *Org Lett* 13(17):4522-4525.

14. Azagarsamy MA, Sokkalingam P, & Thayumanavan S (2009) Enzyme-triggered disassembly of dendrimer-based amphiphilic nanocontainers. *J Am Chem Soc* 131(40):14184-14185.

15. Li JJ*, et al.* (2008) A synthesis of n-bridged 5,6-bicylic pyridines via a mild

cyclodehydration using the burgess reagent and discovery of a novel carbamylsulfonylation reaction. *Org Lett* 10(13):2897-2900.

16. Gatto VJ*, et al.* (1986) Syntheses and binding properties of bibrachial lariat ethers (BiBLEs): survey of synthetic methods and cation selectivities. *J Org Chem* 51(26):5373-5384.

17. Mayer T & Maier ME (2007) Design and synthesis of a tag-free chemical probe for photoaffinity labeling. *European J Org Chem* 2007(28):4711-4720.

18. Gligorich K, M. (2009) Development of palladium-catalyzed alkene functionalization reactions with applications to the synthesis of novel anti-cancer compounds. Ph. D. Thesis (University of Utah, Salt Lake City, UT).

19. Smith BA*, et al.* (2013) Targeting the pymt oncogene to diverse mammary cell populations enhances tumor heterogeneity and generates rare breast cancer subtypes. *Genes Cancer*.

CHAPTER 5

THE SMALL MOLECULE ZINAAMIDOLE INDUCES ZINC DYSHOMEOSTASIS AND IS SELECTIVELY CYTOTOXIC AGAINST CANCER CELLS

Results of the studies presented herein have been submitted for publication: Vaden RM, *et al.* (2014) The novel small molecule zinaamidole induces Zn2+ dyshomeostasis and promotes cancer-specific cell death in patient-derived breast cancer cells.

Abstract

The small molecule zinaamidole (ZNA) was identified from a screen utilizing malignant pleural effusion cells derived from drug refractory breast cancer patients. Follow-up studies with the small molecule revealed that it was cytotoxic against a variety of breast cancer cell types but not against untransformed mammary epithelial cells. ZNA's ability to decrease the viability of drug insensitive cancer cells coupled with its innocuous effects in untransformed cells prompted further evaluation of its molecular mode of action. Next-generation RNA sequencing experiments revealed that ZNA induced the transcription of metal trafficking genes MT1F, MT1X, MT2A, SLC30A2, and SLC30A1. Further exploring the functional effects of ZNA on metal trafficking, $CuSO_4$ and $ZnSO_4$ were each found to modulate ZNA's biological activity, with $ZnSO_4$ potentiating ZNA's cytotoxicity selectively in malignant cells. ZNA and ZNA/$ZnSO_4$-treatment were found to induce caspase independent cell death in cancer cells concomitantly with increases in LC3 expression. Mouse mammary tumor studies revealed that ZNA and ZNA/$ZnSO_4$ attenuated tumor burden and significantly increased animal survival. Studies aimed at identifying the biological target of ZNA suggested a possible role for transient receptor potential (TRP) channel proteins and experiments to examine their function in ZNA-induced cancer cell death are ongoing.

Introduction

Treatment-refractory cancers represent the largest obstacle to improving patient survival and decreasing disease mortality. While initial responses to clinical cancer treatments are initially robust, most cancers will relapse with altered drug sensitivity

profiles. As such, our labs sought to define biological pathways in drug insensitive malignant cells that can be targeted therapeutically. To accomplish this goal, a chemical biology approach was implemented and a small molecule library screen was conducted using malignant pleural effusion cells derived from treatment refractory breast cancer patients (1). With this screen, novel small molecules with cytotoxic phenotypes could be identified and subsequently used as tools to explore the biological pathways perturbed. Considering that many chemotherapeutics employed in the clinic are indiscriminately cytotoxic and often adversely affect healthy, nonmalignant cells, immortalized human mammary epithelial cells were included in the screen so that small molecules with cancer-selective phenotypes could be identified. Fourteen candidate molecules were identified from the screen for follow-up studies. Herein are described the results of experiments aimed at understanding the molecular mode of action of one of these candidate molecules.

Results

The novel small molecule zinaamidole is selectively cytotoxic against cancer cells and induces the transcription of metal trafficking genes

We previously reported the development of a unique small molecule screen aimed at identifying novel molecules with cytotoxic, cancer-selective phenotypes (1). One of these small molecules, zinaamidole (ZNA), was chosen for further investigation to elucidate the underlying mechanisms of its biological activity (Figure 5.1A). Ultimately, the knowledge gained would be used to inform new therapeutic development strategies and also define the molecular features of drug insensitive cancers. As such, initial

Figure 5.1. The small molecule zinaamidole (ZNA) is selectively cytotoxic against malignant cells. (A) Structure of ZNA. (B) Twelve-point dose response analyses of ZNA against immortalized human mammary epithelial cells (hTERT-HMEC) and malignant pleural effusion cells (PE1005339) derived from a drug refractory breast cancer patient. Values plotted represent the mean of three replicates and the standard deviation. (C) Twelve-point dose response analyses of ZNA against an untransformed mammary epithelial cell line (MCF-10A) and three breast cancer cell lines (MCF-7, T47D, MDA-MB-231). Values plotted represent the mean of three replicates and the standard deviation. (D) Clonogenic cell survival assay. Cells were seeded in quadruplicate, exposed to ZNA for 24 hours, then cultured without the small molecule for 21 days. Colonies were stained with crystal violet then quantified. Values plotted represent the mean of four replicates and the standard deviation. (E) Representative images of the clonogenic cell survival assay.

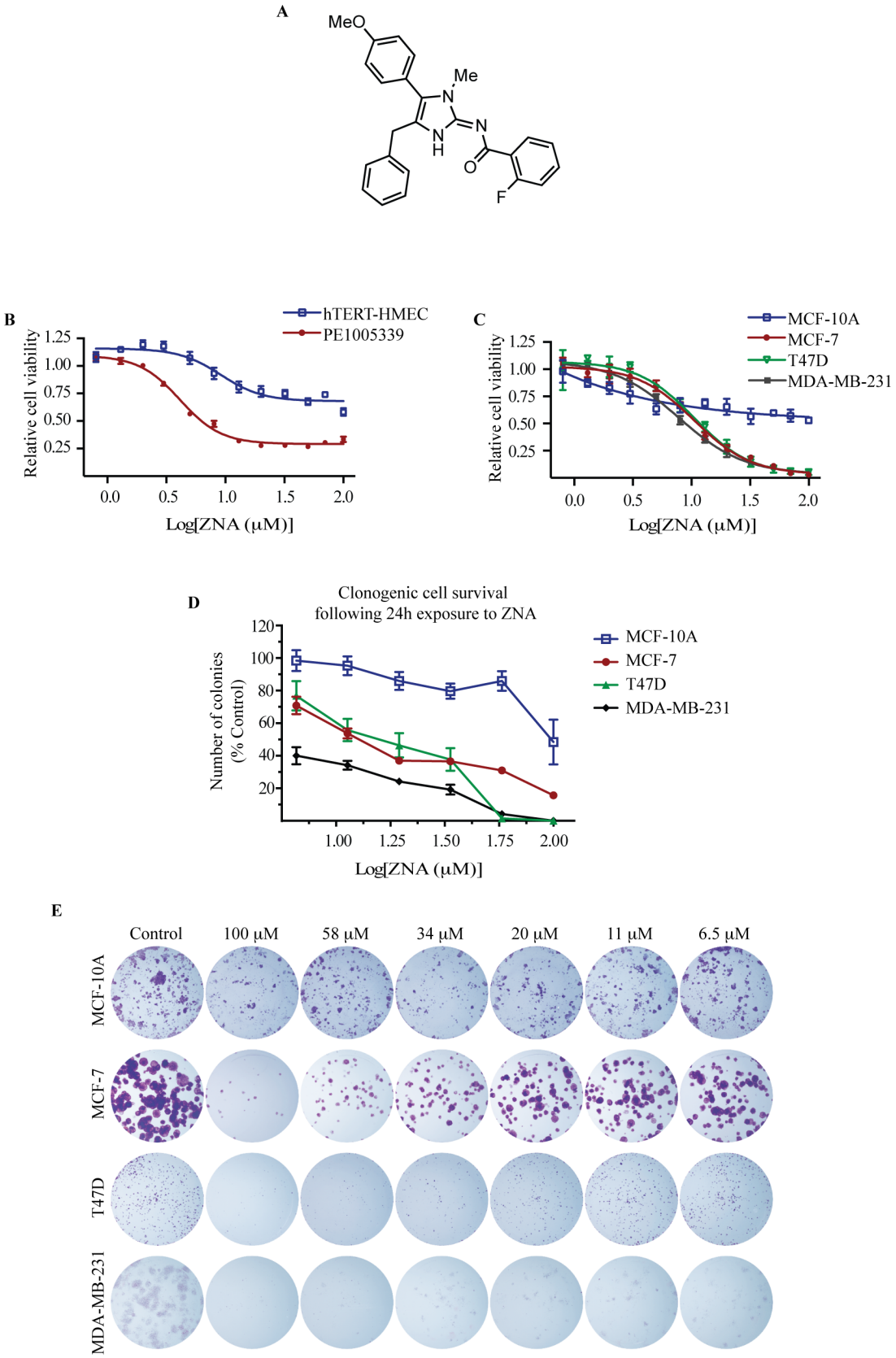
A
MeO
Me
N
N
H
N
O
F
B
hTERT-HMEC
PE1005339
Relative cell viability
1.25
1.00
0.75
0.50
0.25
0.0
0.5
1.0
1.5
2.0
Log[ZNA (μM)]
C
MCF-10A
MCF-7
T47D
MDA-MB-231
Relative cell viability
Log[ZNA (μM)]
D
Clonogenic cell survival
following 24h exposure to ZNA
Number of colonies
(% Control)
120
100
80
60
40
20
1.00
1.25
1.50
1.75
2.00
Log[ZNA (μM)]
MCF-10A
MCF-7
T47D
MDA-MB-231
E
Control
100 μM
58 μM
34 μM
20 μM
11 μM
6.5 μM
MCF-10A
MCF-7
T47D
MDA-MB-231

experiments were designed to assess the generality of ZNA's affect on a variety of cell types. Twelve-point dose response assays were conducted using malignant pleural effusion cells derived from a second breast cancer patient and viability was measured following the completion of treatment. As with the initial small molecule screen, the results of the dose response assay revealed that ZNA was cytotoxic against the malignant cells (PE1005339) but did not significantly affect the untransformed mammary epithelial cells (hTERT-HMEC) (Figure 5.1B). Further evaluating ZNA's effects in different cell types, three breast cancer cell lines and one mammary epithelial cell line were treated with the small molecule. Consistent with the findings of the previous experiments utilizing primary cells, ZNA was found to have a cancer-selective phenotype (Figure 5.1B). Additionally, comparable EC_{50} values were observed in all of the malignant cell types tested, suggesting a common mechanism of action. Upon evaluating the generality of ZNA's biological activity in different cell types, we next sought to establish whether ZNA induced long-term effects on cell survival and proliferation after a short treatment with the small molecule. A clonogenic cell survival assay was employed and cells were treated with ZNA for a sublethal exposure time of 24 hours. The cells were then allowed to grow in drug-free media for 21 days and resulting colonies were stained with crystal violet and quantified. Interestingly, even at the lowest concentration of ZNA tested, a decrease in the number of colonies was observed in the three breast cancer cell lines tested; the proliferative capacity of ZNA-insensitive MCF-10A cells, however, was relatively unaffected (Figures 5.1D and 5.1E).

Encouraged by ZNA's activity against a variety of tumor cell types in both short- and long-term assays, experiments were conducted to understand ZNA's molecular mode of action. A next-generation RNA sequencing experiment was employed to assess how

ZNA affected the transcriptome in MCF-7 breast cancer cells. MCF-7 cells were treated for 3 and 12 hours with 30 μM ZNA and the transcriptome was profiled against control-treated MCF-7 cells. Following differential expression analysis, a significant induction of metal trafficking genes was observed at both time points (Figure 5.2A). MT1F, MT1X, and MT2A were the most upregulated genes following ZNA treatment; these genes encode for members of the metallothionein family, which are small, cysteine-rich proteins capable of binding metals (2). Metallothioneins are thought to play a role in cellular redox homeostasis via their participation in metal sequestration and their function has been studied frequently in the context of metal detoxification (3, 4). In addition to increased metallothionein gene expression, ZNA also stimulated an increase in SLC30A2 and SLC30A1 transcripts. SLC30A2 and SLC30A1, also known as ZNT2 and ZNT1, respectively, function as transmembrane transporters of zinc. More specifically, members of the ZNT protein family have been shown to export Zn^{2+} from the cytoplasm into either the extracellular domain or into cellular compartments and vesicles (5, 6). Collectively, the results of the transcriptome profiling experiment implicate metal dyshomeostasis as a component of ZNA's biological activity, with the changes in SLC30A2 and SLC30A1 further suggesting a specific role for zinc perturbations.

Considering the findings of the next-generation RNA sequencing experiment, we sought next to establish whether the changes in metal trafficking gene transcription were ubiquitous among different types of ZNA-treated cells. Four cell lines were treated with 30 μM ZNA or a vehicle control and the relative gene expressions of MT1F, MT1X, MT2A, SLC30A2, and SLC30A1 were measured by real-time polymerase chain reaction (RT-PCR). Consistent with the results of the RNA-sequencing experiment, the ZNA-treated samples (Figure 5.2B). Furthermore, MCF-10A, MCF-7, and MDA-MB-231

Figure 5.2. ZNA induces the expression of metal trafficking gene transcripts. (A) The most differentially expressed transcripts in 30 μM ZNA-treated MCF-7 cells (compared to control-treated cells) as measured by next-generation RNA sequencing. (B) RT-PCR measurements of gene transcription following exposure to ZNA in four cell types. (C) Flow cytometry quantification of FluoZin-3 fluorescence in four cell types following a time course treatment with ZNA. (D) Flow cytometry quantification of FluoZin-3 fluorescence in four cell types following a 3-hour treatment with ZNA in combination with Actinomycin D (ACTD), an inhibitor of transcription.

A

Log$_2$ Ratio Expression: Control vs. Treated

	3h	12h
MT1F	+3.50	+4.54
MT1X	+3.45	+2.76
MT2A	+3.26	+3.89
DDIT4	+2.06	+2.00
SLC30A2	+1.57	-
CHAC1	+1.52	+1.16
DDIT3	+1.31	-
SLC30A1	+1.28	-
LDLR	-1.14	-
CYP1A1	-1.20	-
CYP1B1	-1.43	-

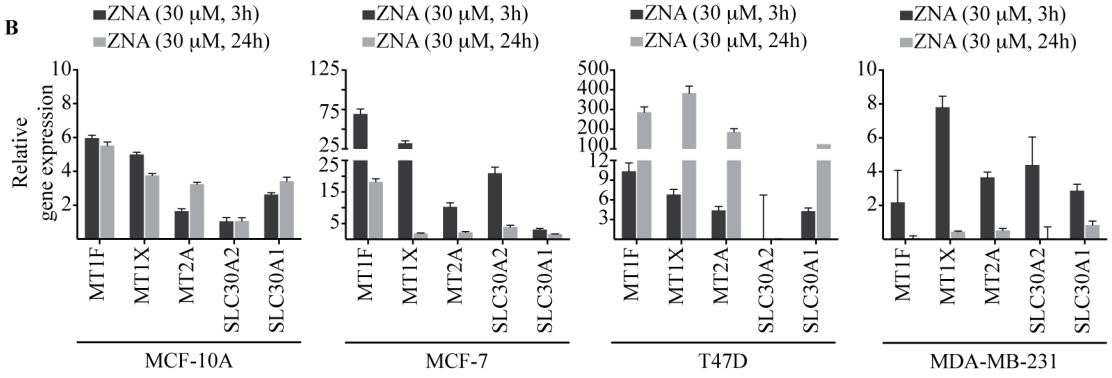

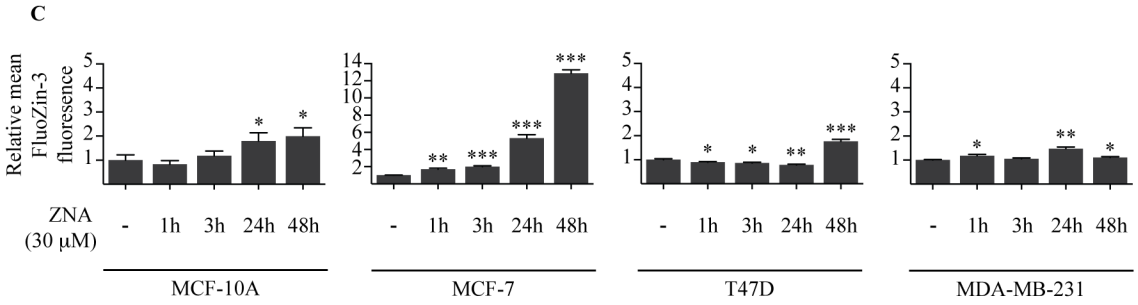

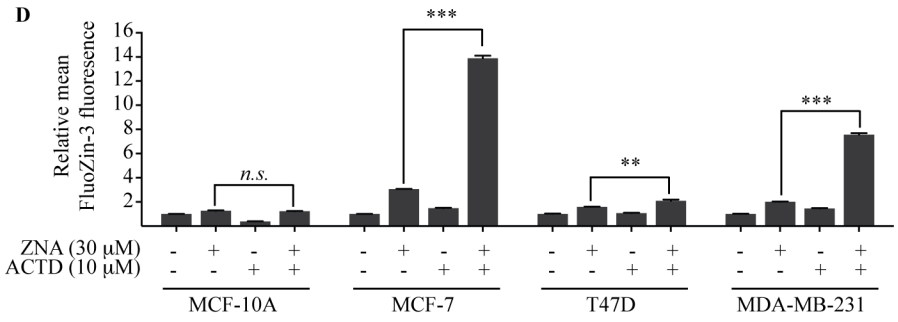

cells presented with similar trends in temporal induction; gene expressions were generally decreased following 24 hours of ZNA-treatment compared to 3 hours, suggesting a dynamic cellular response to ZNA-induced insult.

Upon establishing that metal trafficking genes were significantly upregulated in response to ZNA treatment in a variety of cell types, an investigation to ascertain whether the transcriptional changes reflected significant changes in functional metal trafficking was undertaken. FluoZin-3, a fluorescent Zn^{2+} indicator, was used to measure changes in intracellular Zn^{2+} following a time course treatment with ZNA (Figure 5.2C). MCF-7 breast cancer cells presented with a 13-fold increase in fluorescence following 48 hours of treatment; the three additional cell types tested, however, presented with only modest changes in fluorescence. Considering that the increased metal trafficking gene transcription identified from the RT-PCR experiments might attenuate ZNA-induced changes in intracellular Zn^{2+}, cells were treated with Actinomycin D (ACTD), an inhibitor of transcription, in conjunction with ZNA and FluoZin-3 fluorescence was measured (Figure 5.2D). As hypothesized, the inhibition of transcription resulted in increased levels of FluoZin-3 fluorescence in ZNA/ACTD treated cells as opposed to cells treated with ZNA alone, suggesting that increased gene expression at least partially mitigates the changes in intracellular Zn^{2+}. In all, the results of these initial experiments aimed to understand the basis of ZNA's anticancer activity implicate metal dyshomeostasis as one facet of the small molecule's mode of action.

Zn^{2+} and Cu^{2+} potentiate ZNA's cytotoxic effects

Hypothesizing that ZNA-treatment stimulated increases in intracellular metal concentrations, we next implemented experiments to evaluate the combinatorial effects of ZNA and biologically relevant transition metals added exogenously to cells. Four cell types were supplemented with six different transition metals and treated with 30 μM ZNA. The cells were treated for 48 hours then viability was measured using an ATP quantification assay. Surprisingly, two of the six transition metals were found to dramatically alter cancer cell viability when treated in combination with ZNA (Figure 5.3). $CuSO_4$ and $ZnSO_4$ both strongly potentiated ZNA's cytotoxicity in cancer cells as compared to ZNA treatment alone. In contrast, a differential response was observed in ZNA-insensitive MCF-10A cells: ZNA/$CuSO_4$ resulted in a complete reduction in cell viability while ZNA/$ZnSO_4$ had a minimal effect. To further evaluate the effects of $CuSO_4$ and $ZnSO_4$ on ZNA-treated cells, a propidium iodide uptake assay was employed to measure cell death following 24 hours of treatment (Figure 5.4). The results of the assay were consistent with the results of the transition metal screen—the three breast cancer cell lines tested were sensitive to both ZNA/$CuSO_4$ and ZNA/$ZnSO_4$, but the untransformed mammary epithelial cell line was only sensitive to ZNA/$CuSO_4$. As such, we hypothesized that the underlying mechanism of ZNA's cancer selectivity was founded in zinc dyshomeostasis.

The ability of $CuSO_4$ and $ZnSO_4$ to potentiate ZNA's cell death phenotype in cancer cells was explored further in dose response assays. Twelve-point dose response assays were conducted for 72 hours with ZNA alone, ZNA at varying concentrations with 30 μM $CuSO_4$, or ZNA at varying concentrations with 30 μM $ZnSO_4$. Following the completion of treatment, cell viability was measured using an ATP quantification assay

Figure 5.3. $CuSO_4$ and $ZnSO_4$ potentiate ZNA's affect on cell viability. Four cell types were treated with ZNA alone or in combination with an exogenously added transition metal. The cells were cultured for 48 hours then cell viability was measured using an ATP quantification assay. Values plotted represent the mean of three replicates and the standard deviation.

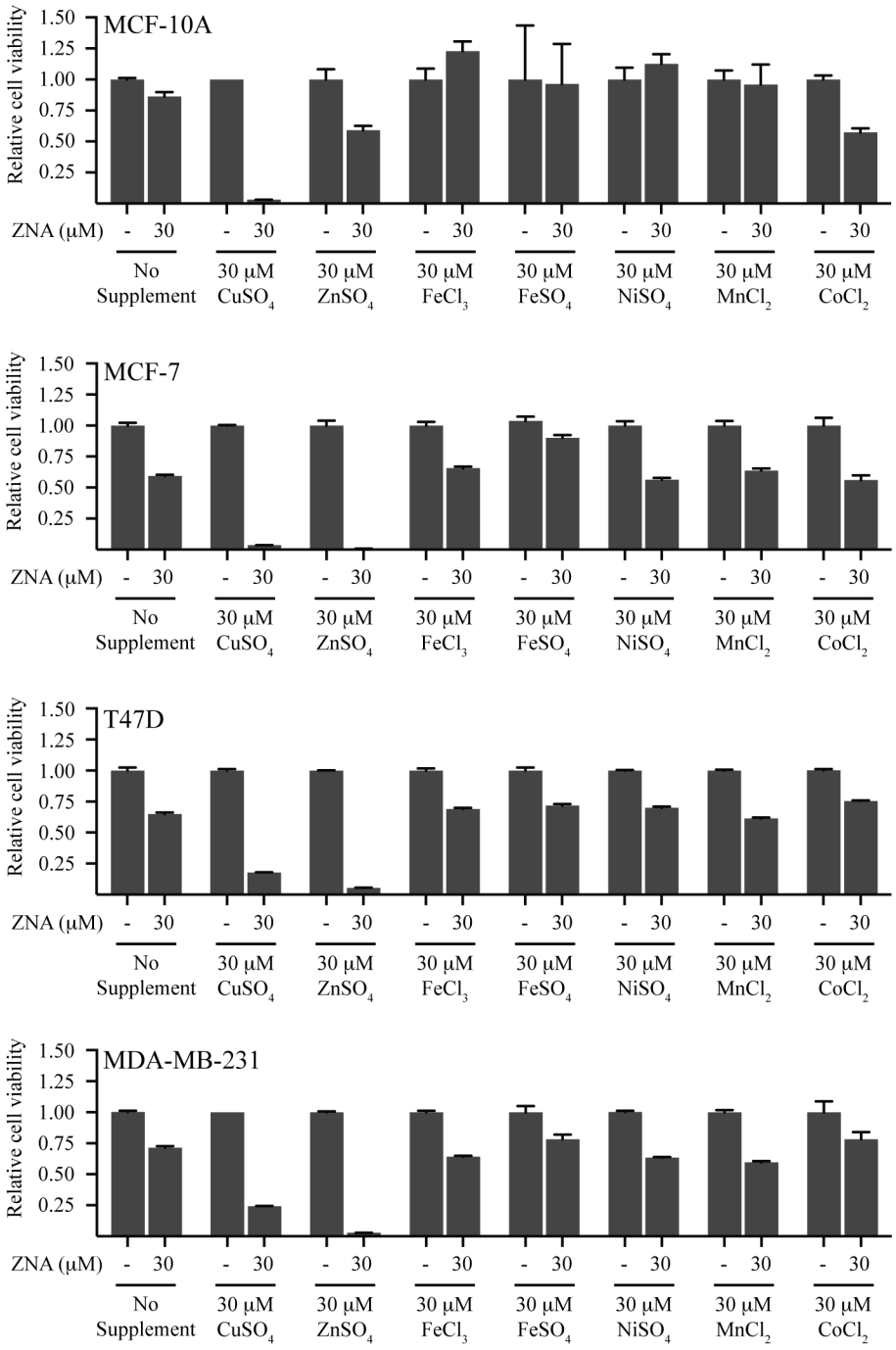
MCF-10A
MCF-7
T47D
MDA-MB-231
Relative cell viability
1.50
1.25
1.00
0.75
0.50
0.25
ZNA (μM) - 30 - 30 - 30 - 30 - 30 - 30 - 30 - 30
No Supplement
30 μM CuSO4
30 μM ZnSO4
30 μM FeCl3
30 μM FeSO4
30 μM NiSO4
30 μM MnCl2
30 μM CoCl2

Figure 5.4. Combinatorial ZNA/$ZnSO_4$ treatment selectively affects the viability of cancer cells. Four cell types were treated with ZNA alone or in combination with $CuSO_4$ or $ZnSO_4$. The cells were cultured for 24 hours then cell viability was measured using a propidium iodide uptake assay and flow cytometry analysis. Values plotted represent the mean of three replicates and the standard error of the mean.

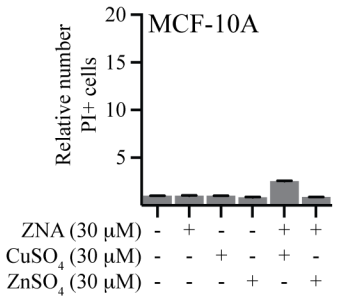
MCF-10A
Relative number PI+ cells
20
15
10
5
ZNA (30 μM) - + - - + +
CuSO4 (30 μM) - - + - + -
ZnSO4 (30 μM) - - - + - +

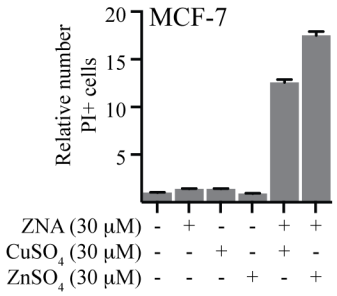
MCF-7
Relative number PI+ cells
20
15
10
5
ZNA (30 μM) - + - - + +
CuSO4 (30 μM) - - + - + -
ZnSO4 (30 μM) - - - + - +

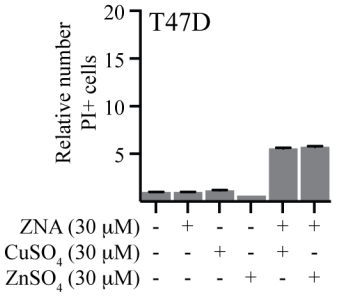
T47D
Relative number PI+ cells
20
15
10
5
ZNA (30 μM) - + - - + +
CuSO4 (30 μM) - - + - + -
ZnSO4 (30 μM) - - - + - +

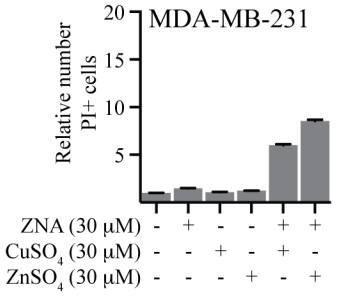
MDA-MB-231
Relative number PI+ cells
20
15
10
5
ZNA (30 μM) - + - - + +
CuSO4 (30 μM) - - + - + -
ZnSO4 (30 μM) - - - + - +

(Figure 5.5). Several notable features were observed from the results of the dose response assay. First, of the four cell types examined, the MCF-10A cells were the most sensitive to ZNA/$CuSO_4$, with $CuSO_4$ potentiating the small molecule's effects at low, nanomolar ZNA concentrations. MCF-10A cells also responded to ZNA/$ZnSO_4$ treatment, but the diminished viability is likely an indicator of growth arrest as opposed to cell death; the nature of dose response assays does not strictly indicate cell death. MCF-7 and MDA-MB-231 cells had similar dose response profiles in each of the three treatment conditions. Interestingly, a bimodal dose curve was observed with ZNA/$ZnSO_4$ wherein very high doses of ZNA were less effective at reducing cell viability than some lower doses; this bimodal effect was not observed in T47D cells. In all, the addition of exogenous $CuSO_4$ and $ZnSO_4$ to ZNA-treated cells significantly alters the potency of the small molecule and the different responses elicited by the two metals on untransformed MCF-10A cells hints at a mechanistic explanation for ZNA's cancer selective nature.

ZNA behaves as an ionophore and promotes Zn^{2+} uptake

Considering the cancer-specific, cytotoxic effects induced by ZNA/$ZnSO_4$-treatment, we next sought to understand how the combination treatment affected intracellular Zn^{2+} levels. Therefore, experiments were conducted with FluoZin-3 to quantify intracellular Zn^{2+} following 3 hours of treatment with either ZNA alone or in combination with $ZnSO_4$ (Figure 5.6A). The results revealed remarkably high levels of intracellular Zn^{2+} in the three breast cancer cell lines evaluated; no less than a 34-fold increase was observed overall and MCF-7 cells presented with a nearly 150-fold increase

Figure 5.5. Combinatorial ZNA/$ZnSO_4$ treatment selectively reduces cancer cell viability. Twelve-point dose response analyses of ZNA against an untransformed mammary epithelial cell line (MCF-10A) and three breast cancer cell lines (MCF-7, T47D, MDA-MB-231). Values plotted represent the mean of three replicates and the standard deviation.

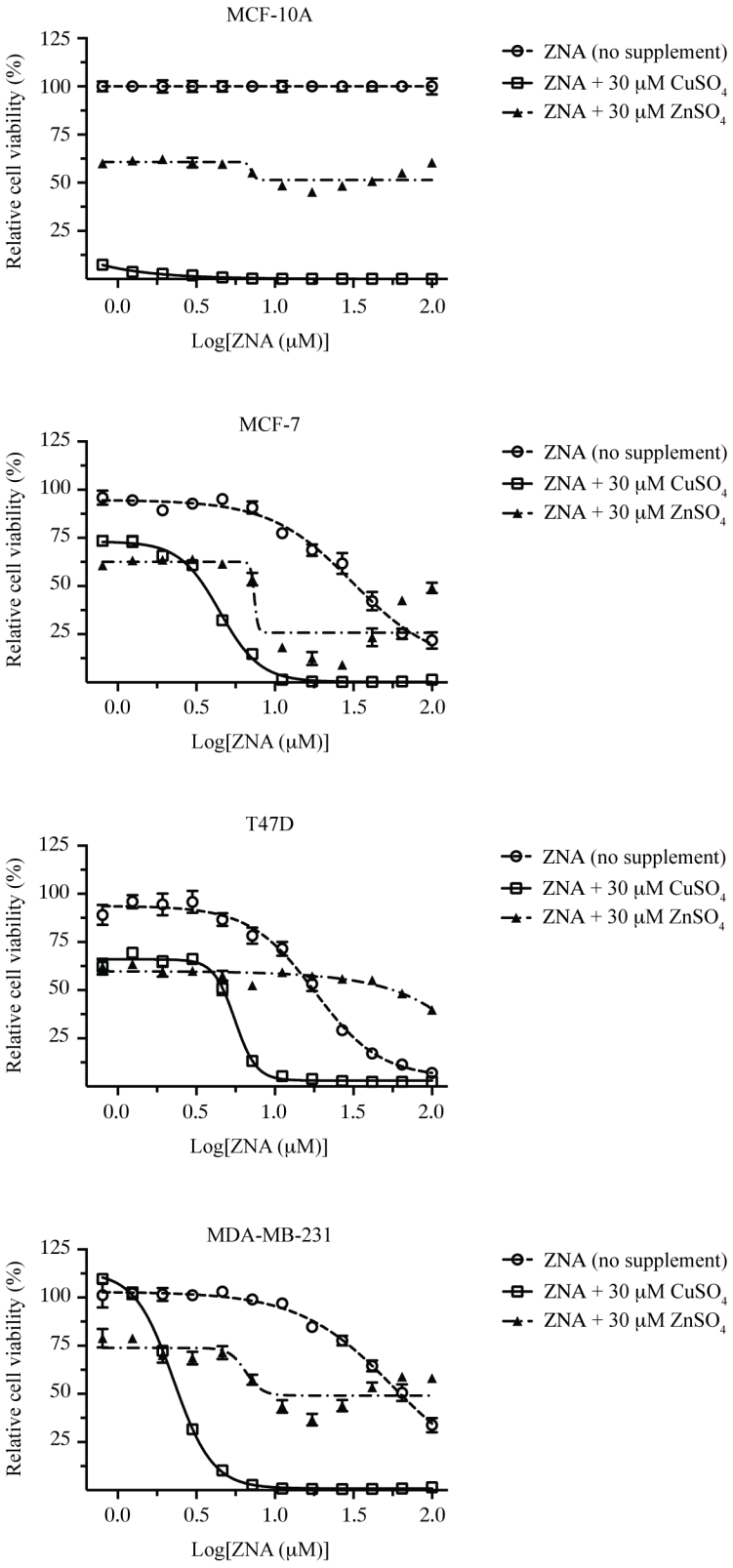
MCF-10A
Relative cell viability (%)
125
100
75
50
25
0.0
0.5
1.0
1.5
2.0
Log[ZNA (μM)]
ZNA (no supplement)
ZNA + 30 μM CuSO4
ZNA + 30 μM ZnSO4
MCF-7
Relative cell viability (%)
125
100
75
50
25
0.0
0.5
1.0
1.5
2.0
Log[ZNA (μM)]
ZNA (no supplement)
ZNA + 30 μM CuSO4
ZNA + 30 μM ZnSO4
T47D
Relative cell viability (%)
125
100
75
50
25
0.0
0.5
1.0
1.5
2.0
Log[ZNA (μM)]
ZNA (no supplement)
ZNA + 30 μM CuSO4
ZNA + 30 μM ZnSO4
MDA-MB-231
Relative cell viability (%)
125
100
75
50
25
0.0
0.5
1.0
1.5
2.0
Log[ZNA (μM)]
ZNA (no supplement)
ZNA + 30 μM CuSO4
ZNA + 30 μM ZnSO4

Figure 5.6. Combinatorial ZNA/$ZnSO_4$ induces significant increase in intracellular zinc. FluoZin-3 was used to quantify ZNA-induced changes in intracellular zinc by flow cytometry analysis following treatment in standard culture media (A) and in zinc-free Hank's balanced salt solution (B).

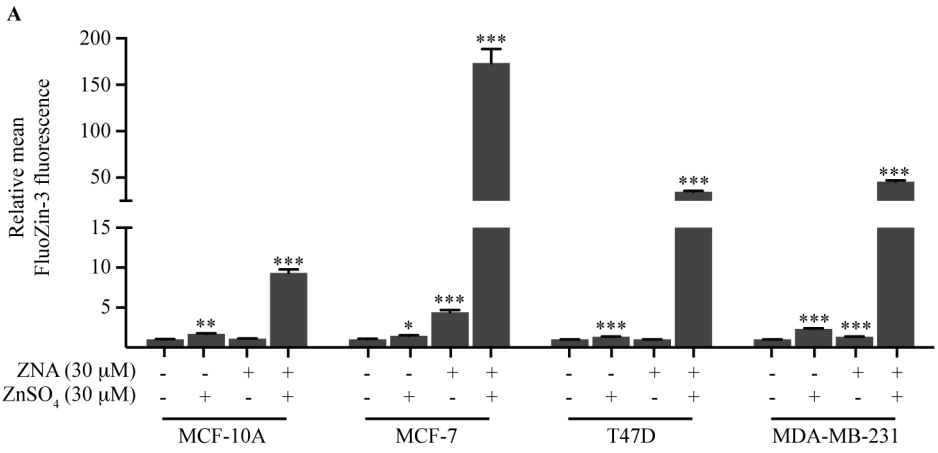
A
Relative mean FluoZin-3 fluorescence
200
150
100
50
15
10
5
***
**
*
***
***
***
***
***
***
ZNA (30 μM) - - + + - - + + - - + + - - + +
ZnSO4 (30 μM) - + - + - + - + - + - + - + - +
MCF-10A
MCF-7
T47D
MDA-MB-231

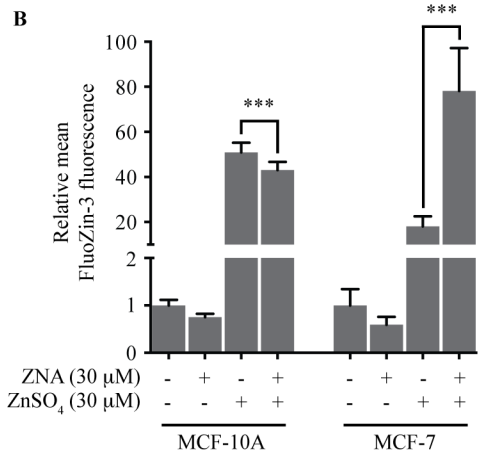
B
Relative mean FluoZin-3 fluorescence
100
80
60
40
20
2
1
0
***
***
ZNA (30 μM) - + - + - + - +
ZnSO4 (30 μM) - - + + - - + +
MCF-10A
MCF-7

in fluorescence. In contrast, the MCF-10A cells presented with only a 9-fold increase, a result that further suggests a role for Zn^{2+} in ZNA's cancer-selective mode of action.

Further probing the ionophore-like affect of ZNA on cells, an experiment was designed to test how ZNA affected cells in Zn^{2+}-free media. Cells were treated for 3 hours in Hank's balanced salt solution with either ZNA or ZNA/$ZnSO_4$, then stained with FluoZin-3 to measure intracellular zinc levels (Figure 5.6B). In MCF-10A cells, combinatorial treatment induced a 43-fold increase while MCF-7 cells presented with a 78-fold increase in fluorescence under the same conditions. With both cell types though, no increase was observed with ZNA-treatment alone. These findings suggest that intracellular Zn^{2+} stores are unlikely to be responsible for providing the high levels of cytosolic Zn^{2+} observed following treatment with ZNA. As such, ZNA-stimulated plasma membrane permeation to extracellular zinc, via protein mediated transport or otherwise, is likely the source of the initial ion imbalance.

Experiments were next conducted to validate the results of the FluoZin-3 experiments and to further assess the specificity of the probe for Zn^{2+}. Inductively coupled plasma-atomic emission spectroscopy (ICP-AES) was used to quantify Zn^{2+} levels in four cell types treated with either ZNA or ZNA/$ZnSO_4$; the relative ion concentrations were normalized to total protein following ICP-AES analysis. The concentration of Zn^{2+} in MCF-7, T47D, and MDA-MB-231 cells was found to be 1.35, 0.52, and 0.82 nanogram of Zn^{2+} per microgram of protein, respectively, following treatment with ZNA/$ZnSO_4$ (Table 5.1). With ZNA-insensitive MCF-10A cells, however, Zn^{2+} levels fell below the detection limit of 1.00 mg/L and the ion was not measured despite protein levels comparable to the three breast cancer cell lines. Overall, while the values obtained from the ICP-AES experiment do not reproduce the absolute

Table 5.1. Total zinc concentration following treatment with ZNA as determined by inductively coupled plasma atomic emission spectroscopy

	MCF-10A	MCF-7	T47D	MDA-MB-231
Control	ND	ND	ND	ND
ZNA (30 μM)	ND	ND	ND	ND
$ZnSO_4$ (30 μM)	ND	0.47 +/- 0.26[a]	0.31 +/- 0.07	ND
ZNA + $ZnSO_4$	ND	1.35 +/-0.06	0.52 +/-0.06	0.82 +/-0.08

Values reported as ng Zn^{2+}/mg of protein.
Values represent mean of three independent replicates; ND=not detected/level below instrument threshold
[a]average of only two replicates

magnitudes of the values obtained from the FluoZin-3 experiments, comparable trends are readily apparent and suggest that Zn^{2+} dyshomeostasis is a specific contributor to ZNA's phenotype.

Considering the significant increases observed in ZNA/$ZnSO_4$-treated cancer cells, we next initiated an experiment to investigate how the excess Zn^{2+} might be stored or contained in cells. Four cell types were treated for 3 hours with ZNA or ZNA/$ZnSO_4$, then fixed and stained with Zinquin, a fluorescent zinc indicator (Figure 5.7) (7). Interestingly, MCF-10A cells treated with ZNA/$ZnSO_4$ presented with increased nuclear Zinquin staining, whereas MCF-7 cells presented with strong, punctate cytoplasmic Zinquin staining under the same treatment conditions. In contrast, no changes in fluorescent intensity or cellular localization were observed in T47D and MDA-MB-231 cells. In all, the results of the staining experiment suggest that varied, cell-type dependent mechanisms of ion sequestration and efflux may be employed following ZNA-stimulated Zn^{2+} influx.

Caspase independent cell death is induced in cancer cells treated with ZNA

With the overall goal of defining biological pathways in drug resistant tumor cells that can be targeted therapeutically, we continued our efforts to fully characterize the anticancer effects of ZNA. Employing a 5-ethynyl-2'-deoxyuridine (EdU) incorporation assay, the effects of ZNA and ZNA/$ZnSO_4$ on cellular proliferation were assessed in four cell types; the incorporation of the nucleoside analog EdU into genomic DNA was measured by flow cytometry following the completion of small molecule treatment

Figure 5.7. Treatment with ZNA/$ZnSO_4$ promotes intracellular Zn^{2+} sequestration. MCF-10A and MCF-7 cells were treated for 3 hours with either ZNA or ZNA/$ZnSO_4$, then fixed and stained with the Zn^{2+} indicator Zinquin.

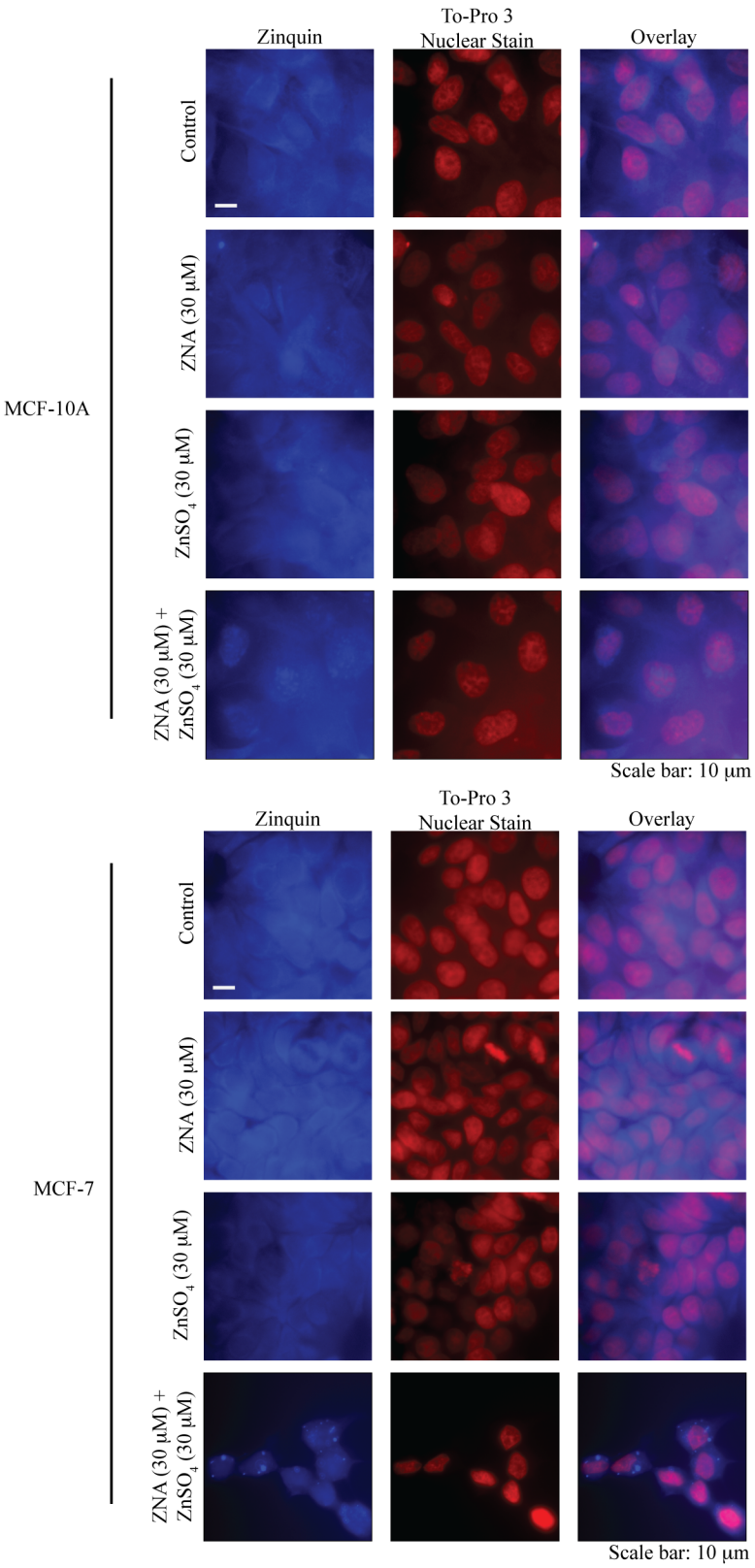
Zinquin
To-Pro 3 Nuclear Stain
Overlay
MCF-10A
Control
ZNA (30 µM)
ZnSO4 (30 µM)
ZNA (30 µM) + ZnSO4 (30 µM)
Scale bar: 10 µm
Zinquin
To-Pro 3 Nuclear Stain
Overlay
MCF-7
Control
ZNA (30 µM)
ZnSO4 (30 µM)
ZNA (30 µM) + ZnSO4 (30 µM)
Scale bar: 10 µm

(Figure 5.8A). After 24 hours of ZNA treatment, a complete cell cycle block was observed in MCF-7 and T47D cells; MCF-10A and MDA-MB-231 cells presented with a 58 and 66% reduction in EdU incorporation, respectively, compared to controls. After only 6 hours of ZNA/$ZnSO_4$ treatment though, all three breast cancer cell lines presented with a complete block in proliferation while ZNA-insensitive MCF-10A cells had only a 27% reduction in EdU incorporation. Together, these data demonstrate the sensitivity of malignant cell types to ZNA/$ZnSO_4$ and further suggest that innate Zn^{2+} trafficking pathways may play a direct role in determining a cell's sensitivity to the small molecule.

In an effort to establish the form of cell death induced by ZNA in cancer cells, experiments were next initiated to determine whether caspases mediated the cell death process. Caspases 3, 7, 8, and 9 are proteases that play direct roles in apoptotic signaling processes in addition to other cell death programs (8, 9). A Caspase-Glo assay was employed to examine the effects of ZNA- and ZNA/$ZnSO_4$-treatment on caspase activation in three different cell types; as a positive control, the small molecule staurosporine, a broad protein kinase inhibitor, was employed. MCF-7 cells were excluded from the assay due to their lack of functional caspase 3 (10). The results of the assay revealed that neither ZNA nor ZNA/$ZnSO_4$ activated caspase activity in any of the cell types tested (Figure 5.8B). As such, the mechanism of ZNA-induced cell death likely proceeds through nonapoptotic pathways.

Upon finding that ZNA induced cell death independent of caspase activation, ZNA-treated cells were evaluated for the induction of necroptosis. Necroptosis, a caspase independent form of programmed cell death, is mediated by receptor interaction protein kinase 1 (RIP1). Inhibition of RIP1 with the small molecule Necrostatin-1 can block cell death and is a defining feature of the cell death program (11). MCF-7 cells

Figure 5.8. ZNA stimulates caspase independent cell death in cancer cells. (A) The affect of ZNA and ZNA/$ZnSO_4$ on proliferation was measured by 5-ethynyl-2'-deoxyuridine (EdU) incorporation and flow cytometry analysis. Values plotted represent the mean of three replicates and the standard error of the mean. (B) A Caspase-Glo enzymatic assay was used to detect caspase activity following ZNA treatment. Staurosporine (STS) was used as a positive control. Values plotted represent the mean of three replicates and the standard deviation.

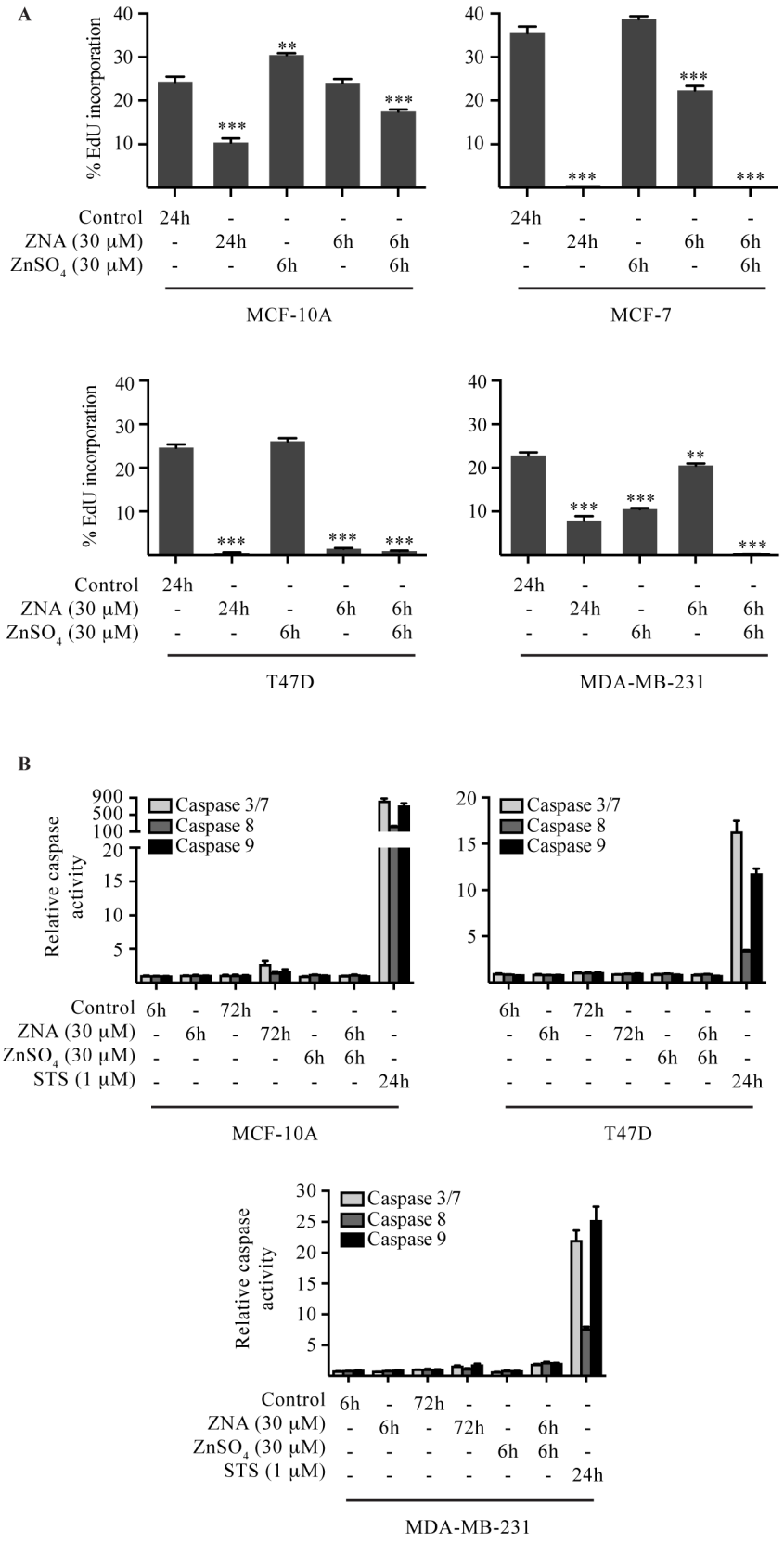
A
% EdU incorporation
40
30
20
10
**
***
Control 24h - - - -
ZNA (30 μM) - 24h - 6h 6h
ZnSO4 (30 μM) - - 6h - 6h
MCF-10A
MCF-7
T47D
MDA-MB-231
B
Relative caspase activity
900
500
100
20
15
10
5
Caspase 3/7
Caspase 8
Caspase 9
Control 6h - 72h - - - -
ZNA (30 μM) - 6h - 72h - 6h -
ZnSO4 (30 μM) - - - - 6h 6h -
STS (1 μM) - - - - - - 24h
MCF-10A
T47D
MDA-MB-231

were treated with ZNA or ZNA/$ZnSO_4$ for 24 hours and cell death was measured by propidium iodide staining; the small molecule shikonin was used as a positive control (Figure 5.9A) (12). The results of the assay revealed that Necrostatin-1 did not significantly inhibit ZNA- or ZNA/$ZnSO_4$-induced cell death, suggesting that the small molecule does not induce necroptosis.

Failing to find evidence in support of apoptosis and necroptosis, we next considered that autophagy might be stimulated by ZNA-treatment. Autophagy is a complex cellular "recycling" process wherein unnecessary cellular components are degraded via lysosomal pathways (reviewed in (13)). To measure autophagic induction by ZNA, the expression of the protein LC3 was monitored by immunoblotting. LC3-I is converted to LC3-II via lipidation and recruited to autophagosome membranes prior to lysosomal-autophagosome fusion (14). Four cell types were treated with either ZNA or ZNA/$ZnSO_4$ and assayed by immunoblotting; the autophagic inhibitor chloroquine, which induces the accumulation of autophagosomes, was used as a positive control (Figure 5.9B) (15). With ZNA treatment alone, LC3-induction was observed only in the small molecule-sensitive cancer cell lines: MCF-7, T47D, and MDA-MB-231 cells. In contrast, no induction was observed in the ZNA-insensitive MCF-10A cells. With combinatorial treatment, T47D cells presented with a significant increase in LC3 protein expression, a slight increase was noted in MDA-MB-231 cells, a reduction was observed in MCF-7 cells, and no induction was observed in MCF-10A cells. Considering that autophagy can stimulate both prodeath and prosurvival pathways, an experiment was next designed to delineate how these observed autophagic processes affected cell outcomes following small molecule treatment. Cells were treated with chloroquine, an inhibitor of autophagy, in combination with ZNA and cell death was quantified by propidium iodide

Figure 5.9. Treatment with ZNA stimulates LC3 expression selectively in cancer cells. (A) The ability of ZNA to induce necroptosis was assessed by treating cells with ZNA in combination with the RIP1 inhibitor Necrostatin-1 (Nec-1). Cell death was assessed 24 hours after treatment initiation by propidium iodide staining and flow cytometry analysis. Shikonin was used as a positive control. Values plotted represent the mean of three replicates and the standard error of the mean. (B) Results of an immunoblot experiment assessing LC3 expression in four cell types following treatment with ZNA. (C) The effects of autophagic inhibition by chloroquine on ZNA-treated cells (72-hour treatment) was assessed by propidium iodide staining and flow cytometry analysis. Values plotted represent the mean of three replicates and the standard error of the mean

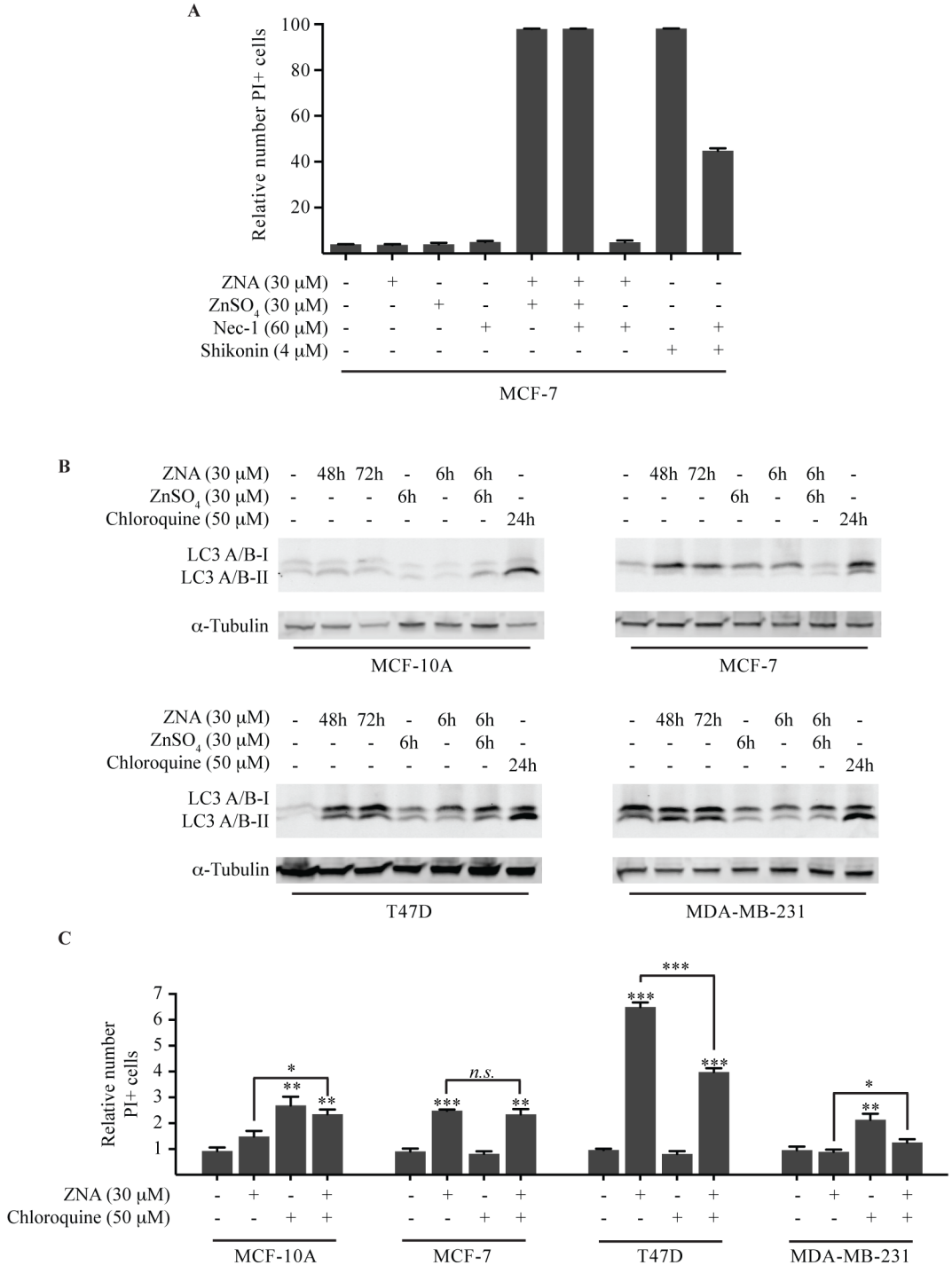
A
Relative number PI+ cells
100
80
60
40
20
ZNA (30 μM) - + - - + + + - -
ZnSO4 (30 μM) - - + - + + - - -
Nec-1 (60 μM) - - - + - + + - +
Shikonin (4 μM) - - - - - - - + +
MCF-7
B
ZNA (30 μM) - 48h 72h - 6h 6h -
ZnSO4 (30 μM) - - - 6h - 6h -
Chloroquine (50 μM) - - - - - - 24h
LC3 A/B-I
LC3 A/B-II
α-Tubulin
MCF-10A
MCF-7
T47D
MDA-MB-231
C
Relative number PI+ cells
7
6
5
4
3
2
1
*
**
**
n.s.
***
**
***
***
***
*
**
ZNA (30 μM) - + - + - + - + - + - + - + - +
Chloroquine (50 μM) - - + + - - + + - - + + - - + +
MCF-10A
MCF-7
T47D
MDA-MB-231

staining. If autophagy contributed to prosurvival phenotypes, the ZNA/chloroquine combination treatment would be expected to result in more cell death than with ZNA alone. Alternatively, if autophagy activated prodeath pathways, the ZNA/chloroquine combination treatment would be expected to result in less cell death than with ZNA alone. The results of the experiment revealed that in T47D breast cancer cells, ZNA/chloroquine treatment attenuated cell death. Differences in the combinatorial treatment condition were observed in the other cell types, but these changes likely reflect the effect of chloroquine treatment alone (Figure 5.9C). As such, these results suggest that autophagic processes contribute to a prodeath phenotype in T47D cells but the role of these processes in other cell types is not immediately clear. Furthermore, the results indicate that the induction of autophagic programs by ZNA may be cell-type dependent.

Several forms of caspase independent cell death have been described to occur concomitantly with redox imbalances and oxidative stress (16-18). To assess whether oxidative imbalances accompanied ZNA-induced phenotypes, cells were treated with ZNA or ZNA/$ZnSO_4$ for up to 48 hours and the oxidation of 2',7'-dichlorodihydrofluorescein diacetate (H2DCFDA, DCF) was used as an indicator of oxidative imbalance; DCF fluorescence was measured by flow cytometry and subsequently normalized to the appropriate vehicle-treated control (Figure 5.10A). The results revealed that ZNA alone stimulated a slight increase in DCF fluorescence; in contrast, combinatorial treatment of ZNA and $ZnSO_4$ resulted in a statistically significant decrease in H2DCFDA oxidation in three breast cancer cell lines compared to their respective controls. The decreased levels of H2DCFDA oxidation observed with ZNA and $ZnSO_4$ combinatorial treatment are consistent with literature reports detailing a connection between increased intracellular Zn^{2+} and perturbations in cellular redox

Figure 5.10. The effects of ZNA-treatment on cellular oxidative homeostasis. (A) Cells were treated with ZNA or ZNA/$ZnSO_4$ then stained with 2',7'-dichlorodihydrofluorescein diacetate (H2DCFDA), which can be oxidized intracellularly to 2',7'-dichlorofluorescein (DCF). DCF fluorescence was measured by flow cytometry. Values plotted represent the mean of three replicates and the standard error of the mean. (B) The effects of *N*-acetylcysteine on ZNA-induced DCF fluorescence was assessed by flow cytometry. Values plotted represent the mean of three replicates and the standard error of the mean. A colleague, Celine Santiago, conducted this experiment.

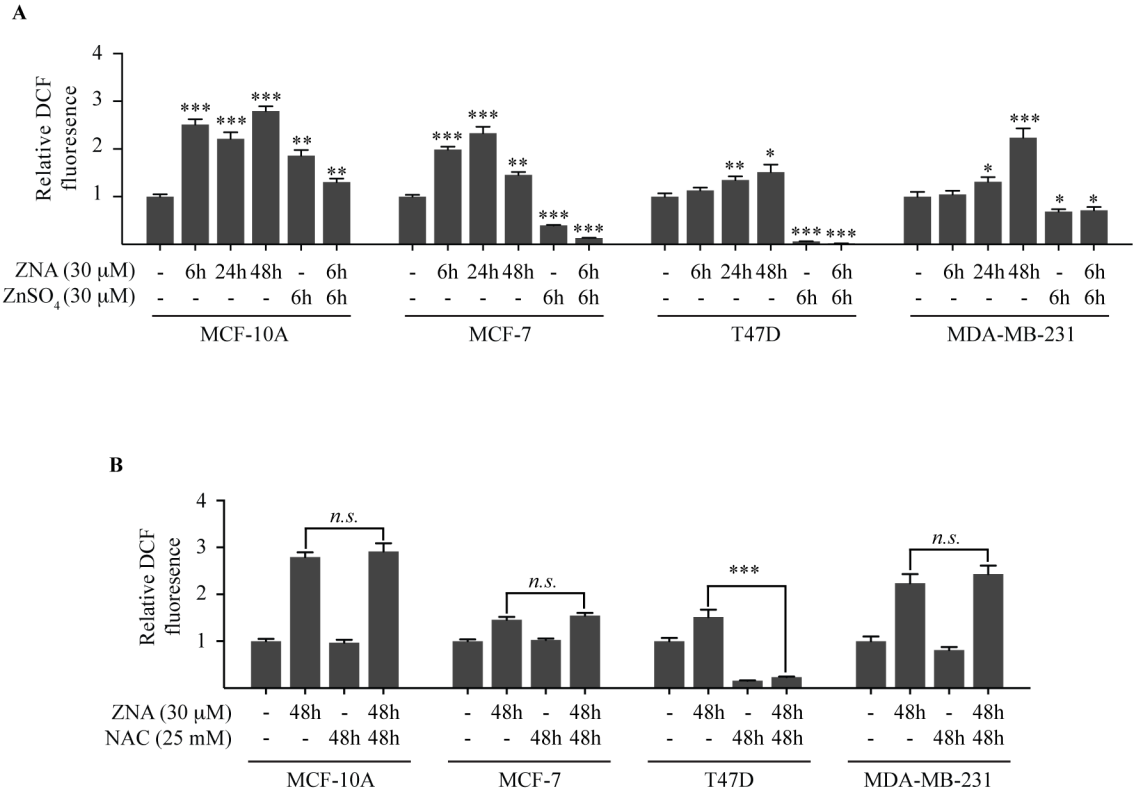
A
Relative DCF fluoresence
4
3
2
1
***
***
***
**
**
***
***
**
***
***
**
*
***
***
*
***
*
*
ZNA (30 μM) - 6h 24h 48h - 6h - 6h 24h 48h - 6h - 6h 24h 48h - 6h - 6h 24h 48h - 6h
ZnSO4 (30 μM) - - - - 6h 6h - - - - 6h 6h - - - - 6h 6h - - - - 6h 6h
MCF-10A
MCF-7
T47D
MDA-MB-231
B
Relative DCF fluoresence
4
3
2
1
n.s.
n.s.
***
n.s.
ZNA (30 μM) - 48h - 48h - 48h - 48h - 48h - 48h - 48h - 48h
NAC (25 mM) - - 48h 48h - - 48h 48h - - 48h 48h - - 48h 48h
MCF-10A
MCF-7
T47D
MDA-MB-231

homeostasis (19-21). Attempts to inhibit this increase with the antioxidant N-acetylcysteine (NAC) were successful only with T47D cells; however, a concomitant decrease in fluorescence was observed in T47D cells treated with NAC alone, confounding its interpretation (Figure 5.10B). Considering that MCF-10A cells treated with ZNA present with increased DCF fluorescence in a manner comparable to breast cancer cells and that NAC did not affect DCF fluorescence in three of the cell types examined, it is unlikely that oxidative imbalances contribute significantly to ZNA's cancer-selective phenotypes.

ZNA effectively decreases tumor burden *in vivo*

With our overall goal of identifying biological pathways in transformed cells that might be targeted for therapeutic intervention, studies implementing whole organism models were implemented to further characterize ZNA's mode of action. We specifically sought to understand whether the metal trafficking pathways perturbed by ZNA in *in vitro* models were similarly modulated in an *in vivo* system. To examine this, nontumor bearing FVB/NJ mice were treated via intraperitoneal injection with ZNA (100 mg/kg) or a matched vehicle control for 3 and 24 hours. Subsequently, metallothionein gene expression was assessed in renal and hepatic tissue by RT-PCR as a measure of perturbations to metal trafficking pathways. The results revealed that MT1 and MT2 expression was increased after 3 hours of treatment in both tissue types but decreased following 24 hours of treatment. Interestingly, this trend mirrors the results of the *in vitro* experiments utilizing cell lines wherein MT gene expression was increased acutely following exposure to ZNA but decreased following longer exposure times (Figure

5.11A). Collectively, these data suggest that ZNA is bioavailable and also that the pathways stimulated by the small molecule *in vitro* are intact and responsive in a whole organism model.

Considering the promising results of the preliminary *in vivo* experiments, a study was designed to assess how ZNA affected tumor growth in a mouse mammary tumor model. PyMT mouse mammary tumors were transplanted into the uncleared mammary fat pads of three-week old female recipient FVB/NJ mice (22). Following three weeks of tumor growth, ZNA treatment was initiated. Mice were treated once a day for 21 days and four treatment conditions were evaluated: ZNA (100 mg/kg administered via intraperitoneal), $ZnSO_4$ (25 mM administered continuously for the duration of treatment via drinking water), a combination of ZNA and $ZnSO_4$, and a control group (PBS administered via intraperitoneal injection). As an endpoint, a tumor diameter greater than 2 cm was established for the study. Following the completion of treatment, the results revealed that both ZNA alone and ZNA/$ZnSO_4$ significantly improved animal survival compared to control- or $ZnSO_4$-treated groups, respectively (Figure 5.11B). Furthermore, no general toxicity, acute toxicological responses, or losses in body weight were observed in the mice treated with ZNA or with the combination of ZNA and $ZnSO_4$. These exciting results suggest that the pathways modulated by ZNA *in vitro* are relevant and functional in *in vivo* models. The lack of general systemic toxicity suggests a relatively wide therapeutic treatment window—a desirable trait for new therapies when considering the significant toxicity of currently used chemotherapeutics.

From the *in vivo* ZNA treatment study, we initiated an experiment to determine whether the tumor tissue from the study displayed altered levels of metallothionein gene expression. As such, tumor tissue from 23-day, treatment time-matched ZNA-,

Figure 5.11. ZNA attenuates tumor growth *in* an *in vivo* mouse mammary tumor model. (A) The expression of metallothioneins 1 and 2 (MT1 and MT2) was assessed by RT-PCR from renal and hepatic tissue in nontumor bearing FVB/NJ mice. Mice were treated for 3 or 24 hours with either ZNA (100 mg/kg, intraperitoneal injection) or a vehicle control. Raw RT-PCR values were internally normalized to β-actin. (B) FVB/NJ mice were transplanted with PyMT tumors, which were allowed to grow for 3 weeks. Then, the following treatments were conducted for 21 days: Control (intraperitoneal PBS injection once per day), ZNA (100 mg/kg, intraperitoneal injection once per day), $ZnSO_4$ (25 mM administered continuously via drinking water), or combinatorial treatment (100 mg/kg ZNA, intraperitoneal injection once per day and 25 mM $ZnSO_4$, administered continuously via drinking water). Statistical significance: Control versus ZNA, ** ($p=0.01$); $ZnSO_4$ versus combinatorial treatment, ** ($p=0.007$). (C) From this *in vivo* tumor study, the expression of metallothioneins 1 and 2 (MT1 and MT2) was assessed by RT-PCR from tumor tissue derived from treatment-matched (23 days) mice.

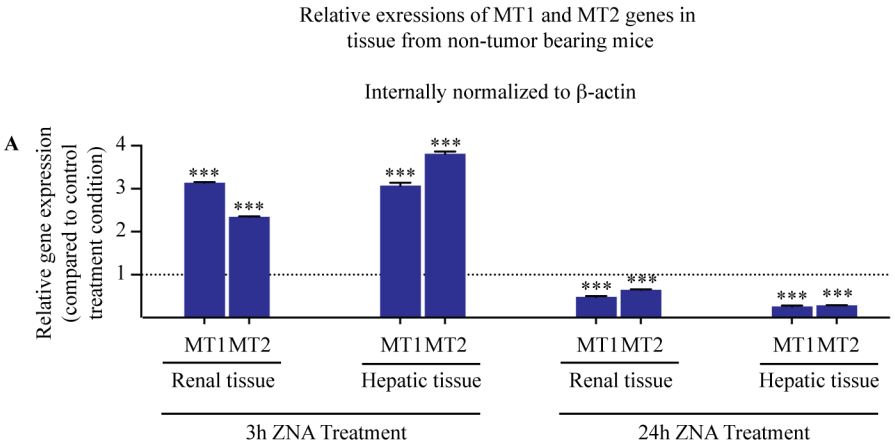
Relative exressions of MT1 and MT2 genes in
tissue from non-tumor bearing mice
Internally normalized to β-actin
A
Relative gene expression
(compared to control
treatment condition)
4
3
2
1
***
MT1 MT2
Renal tissue
Hepatic tissue
3h ZNA Treatment
24h ZNA Treatment

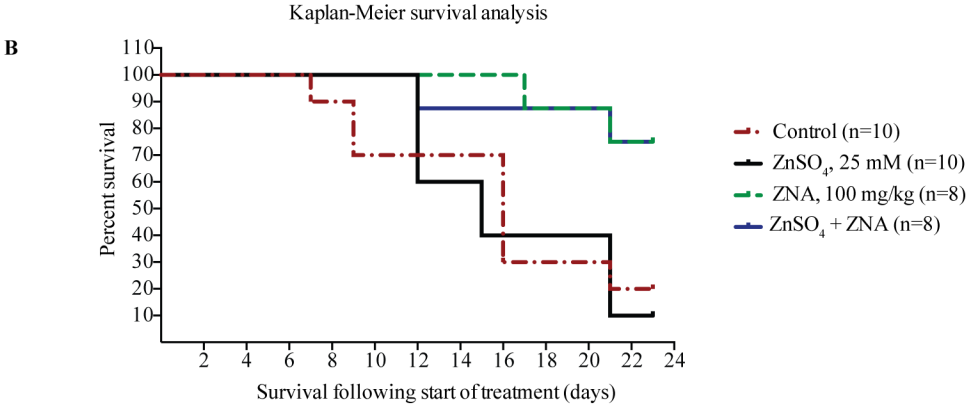
Kaplan-Meier survival analysis
B
Percent survival
110
100
90
80
70
60
50
40
30
20
10
2 4 6 8 10 12 14 16 18 20 22 24
Survival following start of treatment (days)
Control (n=10)
ZnSO4, 25 mM (n=10)
ZNA, 100 mg/kg (n=8)
ZnSO4 + ZNA (n=8)

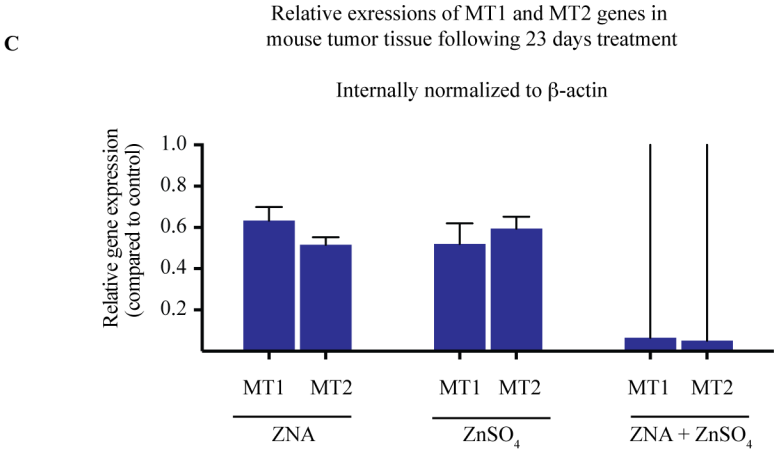
C
Relative exressions of MT1 and MT2 genes in
mouse tumor tissue following 23 days treatment
Internally normalized to β-actin
Relative gene expression
(compared to control)
1.0
0.8
0.6
0.4
0.2
MT1 MT2
ZNA
ZnSO4
ZNA + ZnSO4

ZNA/$ZnSO_4$-, $ZnSO_4$-, and control-treated mice were analyzed for MT1 and MT2 expression by RT-PCR. A reduction in MT1 and MT2 expression was observed in all treatment groups relative to the control, with the ZNA/$ZnSO_4$-treated mouse presenting with nearly undetectable levels (Figure 5.11C). Considering the length of treatment time (23 days) in the context of the previous RT-PCR experiments, the results are consistent with the expectation that longer treatment times result in a depression of metallothionein gene expression. Further validation experiments are needed to fully understand these preliminary *in vivo* gene expression findings though.

Exploring the contribution of ion transport proteins to ZNA's mode of action

Considering ZNA's unique cancer-selective phenotype and its ability to significantly reduce tumor burden in an *in vivo* model of breast cancer, experiments were initiated to identify the target of the small molecule and to further characterize the molecular mechanism of action. Based on the sum of our mechanistic data implicating metal ion dyshomeostasis as a key component of ZNA's mode of action, we hypothesized that ZNA modulated ion channel proteins, which in turn promoted the uptake of extracellular metal ions. Reviewing the literature, we identified three different protein families that were capable of transporting metal ions and could be localized to the plasma membrane, as opposed to strict intracellular localization. Herein are described our efforts to elucidate the contribution, if any, that these protein families might make to ZNA's phenotype.

The ability of zinc and copper to potentiate ZNA's cell death phenotype prompted

first the hypothesis that ZNA directly affected an ion channel capable of transporting both ions. A thorough literature investigation revealed that the protein divalent metal transporter 1 (DMT1) was capable of transporting both zinc and copper (23). If DMT1 played a role in ZNA's mechanism of action, a reduction in its expression would be expected to alter the sensitivity of cells to the small molecule. To implement such an experiment, five lentiviral shRNA constructs targeting DMT1 were used to knockdown DMT1 expression in MCF-7 cells. The efficiency of the knockdown in each line was assessed by RT-PCR (Figure 5.12A). Using 30 μM ZNA, a selection experiment was then conducted with the five stably expressing shRNA-DMT1 lines, one transduction control line, and untransduced MCF-7 cells. Cells were treated with the small molecule for 14 days to select for resistant cells. Unfortunately, no surviving cells were identified in any of the lines, with the exception of the shRNA-DMT1 construct #4 line. This line, however, was senescent following treatment with ZNA and proliferation did not recover even after removal of the small molecule. The same result was obtained upon experimental reproduction with fresh virus and newly transduced cells, suggesting that the senescent phenotype was a result of the construct's expression. While the line did survive treatment, its failure to proliferate even aftqer removing ZNA from the media did not allow for further follow-up experiments to be conducted. As such, the role of DMT1 in ZNA-stimulated phenotypes remains unclear.

The increased expression of zinc efflux proteins ZNT1 and ZNT2 following ZNA treatment, which likely occurs as a means to mediate the acute increase in intracellular zinc, prompted us to next evaluate the importance of zinc-specific influx proteins in ZNA's mechanism of action. In particular, we hypothesized that ZNA-mediated

Figure 5.12. Relative gene expression of DMT1 in shRNA-DMT1 knockdown MCF-7 cells. Five lentiviral constructs were used to knockdown expression of DMT in MCF-7 cells. RT-PCR measurements were conducted to assess the efficiency of knockdown. Raw RT-PCR values were internally normalized to GAPDH.

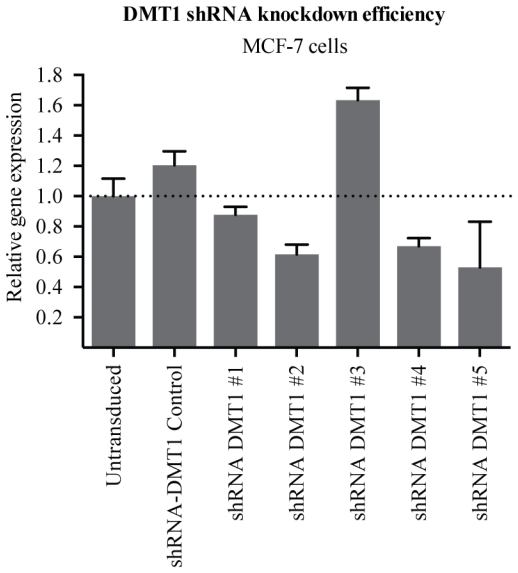
DMT1 shRNA knockdown efficiency
MCF-7 cells
Relative gene expression
1.8
1.6
1.4
1.2
1.0
0.8
0.6
0.4
0.2
Untransduced
shRNA-DMT1 Control
shRNA DMT1 #1
shRNA DMT1 #2
shRNA DMT1 #3
shRNA DMT1 #4
shRNA DMT1 #5

modulation of ZIP proteins, a family of 14 zinc transport proteins that function to increase cytosolic levels of zinc, could produce the Zn^{2+} phenotypes observed in treated cells (reviewed in (24)). To examine the validity of this hypothesis, we first conducted a data analysis experiment profiling relative ZIP gene expression levels to assess whether the genes were expressed and if so, to what extent. Normalized data from the next-generation RNA sequencing experiment was extracted from the vehicle-treated control sample analyses and rank ordered according to expression (Table 5.2). A variety of expression levels were observed within the family, with ZIP6 and ZIP7 having the highest expression levels in MCF-7 cells while ZIP2 and ZIP12 expression fell below the detection limit. In all, these results define a general profile for the expression of ZIP proteins in these cells.

Next, an experiment was designed to test the importance of ZIP protein family members on ZNA's mode of action. Considering that structural redundancy within the ZIP family might confound the results of experiments aimed at understanding the contribution of an individual ZIP protein, an alternative strategy was developed. Using a pooled shRNA knockdown approach, constructs targeting the expression of the 14 ZIP family members (with a minimum of two constructs per gene) were pooled and used for the transduction of MCF-7 cells. With this strategy, random viral integrations with constructs targeting multiple ZIP proteins would be expected within a single cell. As such, the experimental design would allow for the identification of ZIP proteins whose function would normally be replaced by a family member with redundant activity. Despite the advantages of the pooled shRNA approach though, the experiment failed to generate clones with resistance to ZNA. This result may be indicative of two possibilities: that ZIP proteins are uninvolved in ZNA's mode of action or that functional

Table 5.2. Rank ordered expressions of ZIP (SLC39A) transcripts in MCF-7 cells

Gene	Sample 1 FPKM	Sample 2 FPKM	Sample 3 FPKM	Sample 4 FPKM	Sample 5 FPKM	Sample 6 FPKM	Average FPKM rank ordered
SLC39A6	162.683	162.948	158.333	156.980	149.309	141.218	155.25
SLC39A7	88.933	88.995	90.064	95.634	97.763	91.431	92.14
SLC39A8	69.794	61.731	62.656	65.261	74.018	66.111	66.60
SLC39A1	29.349	28.237	28.966	30.730	32.308	31.499	30.18
SLC39A9	16.602	15.370	15.326	15.314	15.242	14.141	15.33
SLC39A14	8.412	9.210	9.461	7.370	6.929	7.441	8.14
SLC39A11	4.627	4.486	4.541	5.080	6.045	5.301	5.01
SLC39A3	3.759	3.874	3.852	4.974	4.772	5.023	4.38
SLC39A13	3.179	3.453	3.850	3.865	3.223	4.131	3.62
SLC39A10	3.005	3.045	2.514	3.446	3.011	3.145	3.03
SLC39A4	2.658	2.405	2.673	3.149	2.822	3.051	2.79
SLC39A5	0.158	0.229	0.184	0.308	0.269	0.192	0.22
SLC39A2	0.000	0.000	0.000	0.000	0.000	0.000	0.00
SLC39A12	0.000	0.000	0.000	0.000	0.000	0.000	0.00

FPKM: Fragments per kilobase of exon per million fragments, as derived from next-generation RNA sequencing

redundancy within the protein family is more pervasive than first hypothesized. As such, the role of ZIP proteins in ZNA's biological mechanism of action remains enigmatic.

Considering a different ion transport family, we next conducted experiments to investigate the importance of transient receptor potential (TRP) channel proteins in ZNA's molecular mode of action. TRP channels serve a variety of biological functions and their roles in pain sensing, ion transduction, and sensory perception (e.g., pressure, vibration, heat, taste, etc.) have been well documented. At least 28 TRP family members grouped into six subfamilies have been identified in mammalian cells and their leitmotif of cation permeability extends largely to Ca^{2+}, Mg^{2+}, and Na^{2+} (reviewed in (25, 26)). More recently though, evidence has been presented indicating that some TRP channels can be permeated by other biological trace metals (27-31). Zinc ion transduction via TRP channels has specifically been reported for TRPM7, TRPA1, TRPC6, TRPV6, TRPM3, TRPM6, and TRPML1 but additional TRP channels with this function may yet be discovered (32-38). Considering that Zn^{2+} and Cu^{2+} potentiate ZNA-induced cell death, we hypothesized that TRP channels could be facilitating the uptake of these extracellular metal ions via direct ZNA-stimulated TRP activation. To test this hypothesis, a small molecule inhibitor of TRP channels, *N*-(p-amylcinnamoyl)anthranilic acid (ACA), was employed. ACA is frequently used as a broad spectrum TRP inhibitor and has been shown to specifically block TRPC6, TRPM2, TRPM8 channels; however, ACA's molecular activity is not fully defined and the molecule may also have stimulatory effects on TRPC3, TRPC5, TRPV1 and TRPV4 channels (39, 40). With the limited commercial availability of broad spectrum TRP inhibitors, ACA was considered a reasonable first option for examining the role of TRP channels in ZNA-induced cancer cell death. As such, MCF-7 cells were treated with ACA in combination with either ZNA or

ZNA/$ZnSO_4$ for 3 hours and intracellular Zn^{2+} was quantified with FluoZin-3 by flow cytometry analysis (Figure 5.13). Interestingly, the combination of ACA with ZNA/$ZnSO_4$ produced the highest levels of FluoZin-3 fluorescence—more than 2 times higher than ZNA/$ZnSO_4$ and more than 80 times higher than control-treated cells. This dramatic increase in fluorescence with the ACA/ZNA/$ZnSO_4$ combination treatment suggests that TRP channels could be contributing directly to ZNA's phenotype in cancer cells. However, the ambiguity associated with ACA's molecular targets confounds efforts to fully understand the underlying mechanism for this effect. As such, experiments aimed at delineating the roles of individual TRP channels and their subfamilies will be paramount for understanding ZNA's effects on plasma membrane ion permeation.

Discussion

Herein was described the mechanism of action of the small molecule zinaamidole (ZNA). From a screen employing malignant pleural effusion cells obtained from drug refractory breast cancer patients, ZNA was identified for its ability to selectively reduce the viability of these cancer cells while leaving untransformed mammary epithelial cells largely unaffected. With the overall goal of utilizing ZNA as a molecular tool to probe and define pathways in drug insensitive tumors that could be targeted therapeutically, we implemented experiments to understand the small molecule's mode of action. Upon assessing ZNA's effects in different malignant and nonmalignant mammary epithelial cell types, we established a general profile of its activity and further validated the cancer-selective nature of its cytotoxicity. Next-generation RNA sequencing experiments were

Figure 5.13. The broad spectrum TRP channel inhibitor modulates ZNA/$ZnSO_4$-mediated Zn^{2+} influx. MCF-7 cells were treated with the TRP channel inhibitor *N*-(p-amylcinnamoyl)anthranilic acid (ACA) in combination with ZNA or ZNA/$ZnSO_4$ for 3 hours. Intracellular Zn^{2+} was then quantified by FluoZin-3 staining and flow cytometry analysis. Values plotted represent the mean of three replicates and the standard error of the mean.

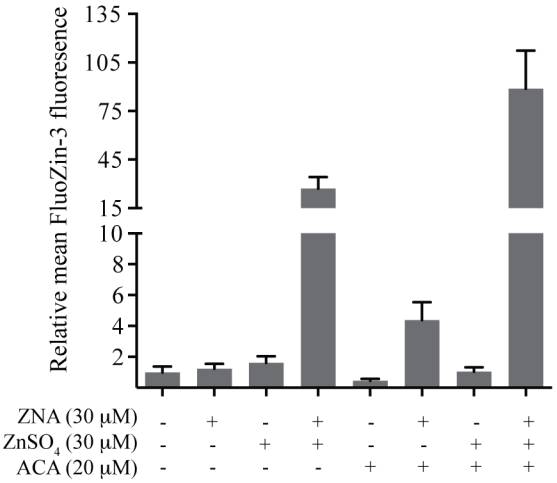
Relative mean FluoZin-3 fluoresence
135
105
75
45
15
10
8
6
4
2
ZNA (30 μM) - + - + - + - +
ZnSO4 (30 μM) - - + + - - + +
ACA (20 μM) - - - - + + + +

then employed to better understand ZNA's affect on the transcriptome. These experiments revealed a stark increase in metal trafficking transcripts and provided crucial insight into ZNA's mechanism of action.

Considering the impact of ZNA on metal trafficking gene transcription, a biological trace metal screen was conducted to assess how exogenously added transition metals might affect ZNA's biological activity. The results of the screen revealed that $CuSO_4$ and $ZnSO_4$ strongly potentiated ZNA's biological activity. Curiously though, ZNA/$CuSO_4$ was found to induce rapid cell death in all cell types while ZNA/$ZnSO_4$ was found to be cytotoxic only against malignant cells. This observation prompted the hypothesis that ZNA's cancer selective phenotype could be attributed to small molecule-induced perturbations in Zn^{2+} trafficking. Further experiments aimed at defining the form of cell death promoted by ZNA treatment revealed the small molecule induced caspase independent cell death, with autophagic processes activated in ZNA-sensitive cell types. These autophagic processes were found to contribute to activation of pro-death pathways only in T47D cells; though, the role of autophagic induction in MCF-7 and MDA-MB-231 cells remains unclear. Interestingly, the T47D cells also displayed an altered temporal induction of metal trafficking genes following treatment with ZNA. While MCF-10A, MCF-7, and MDA-MB-231 cells presented with acute increases at 3 hours followed by a reduction in expression at 24 hours, the T47D cells presented with acute increases at 3 hours followed by even greater increases at 24 hours. The molecular basis for the different response kinetics is not known, but the induction of autophagic, prodeath pathways in T47D cells may be connected to these transcriptional responses.

The ability of ZNA/$ZnSO_4$ to induce acute increases in cytosolic Zn^{2+} concentrations was demonstrated by FluoZin-3 staining as well as with atomic emission

spectroscopy analyses. ZNA/$ZnSO_4$'s effects on cytosolic Zn^{2+} concentrations in untransformed cells was significantly attenuated compared to the three malignant cell types evaluated, further suggesting that innate, cell-specific Zn^{2+} transport mechanisms play an important role in determining a cell's sensitivity to ZNA. The results of experiments utilizing Zinquin, a stain used with fixed cells to assess intracellular Zn^{2+} localization, revealed that MCF-7 cells treated with ZNA/$ZnSO_4$ had strong, punctate staining within the cytoplasm. This result suggests that MCF-7 cells mitigate the molecular insult of ZNA by sequestering the excess ion into discreet, intravescicular pools, potentially zincosomes (5, 41). In contrast to the result obtained with MCF-7 cells, MCF-10A cells presented with an increase in diffuse, nuclear Zinquin staining and no differences were observed in T47D and MDA-MB-231 cells compared to control-treated cells. Taken together, these results suggest that cellular responses to acute Zn^{2+} increases are varied and that injury mitigation, whether via efflux or sequestration, are likely cell-type dependent. Additional imaging experiments conducted with brighter, more photostable Zn^{2+} fluorescent indicators should be implemented for more precise cellular localization studies.

With the overall aim of defining pathways that can be targeted in drug refractory cancers, mouse models were utilized to determine whether ZNA's mode of action *in vitro* translated to whole organism systems. First, we sought to assess the bioavailability of ZNA and tested the small molecule's ability to induce metallothionein gene expression in tissue from nontumor bearing mice. The RT-PCR results were found to be analogous to the *in vitro* RT-PCR experiments: metallothionein gene expression was increased in renal and hepatic tissue following 3 hours of treatment, and depressed after a 24 hour-treatment. These results suggest that the pathways perturbed by ZNA *in vitro* are both

functional and responsive in a whole organism. With this information in hand, a study was conducted to assess the affect of ZNA on the survival of mammary tumor bearing mice. Both ZNA and ZNA/$ZnSO_4$ had profound effects on animal survival and significantly attenuated tumor burden compared to their respective controls.

Efforts to understand the biological target of ZNA led us to evaluate DMT1, ZIP proteins, and TRP channels, as each of these proteins/protein families have been reported to transport Zn^{2+} across the plasma membrane. Knockdown experiments aimed at studying the roles of DMT1 and ZIP proteins in ZNA's phenotype failed to produce evidence in support of their involvement. Experiments conducted with a broad spectrum TRP channel inhibitor, ACA, in combination with ZNA and ZNA/$ZnSO_4$, however, revealed a strong Zn^{2+} response in cells following treatment. ACA/ZNA/$ZnSO_4$-treatment was found to significantly increase FluoZin-3 fluorescence in MCF-7 cells compared to ZNA/$ZnSO_4$-treatment, suggesting a role for TRP channels in ZNA's mode of action. Unfortunately, the specificity of ACA's activity against different TRP channels has not been fully detailed, leaving open questions as to which TRP channels may be contributing to ZNA's phenotype. Furthermore, whether ZNA may agonize or antagonize the activity of these TRP channels has yet to be determined. Future experiments designed to test the involvement of TRP channels in ZNA's mode of action must also take into account the multimeric nature of the proteins. Structural studies have revealed that the channels are comprised of four individual TRP protein subunits, affording quaternary architecture (42, 43). Furthermore, homo- and heteromeric assemblies of the subunits have been reported, adding a subtle layer of complexity to the interpretation of experiments designed to analyze individual TRP channels (44-46).

The small molecule ZNA shows extraordinary promise for future investigations

aimed at defining biological pathways in drug refractory cancer cells that can be targeted therapeutically. The work presented herein describes a significant step in the process of understanding ZNA's mechanism of action, but important questions remain. While our *in vitro* and *in vivo* experiments consistently highlight the cancer-selectivity of ZNA, the precise molecular reason for this phenomenon is unknown. Differential ion transporter gene expression and differential trace metal trafficking programs are both plausible explanations for the ZNA's selectivity profile and genome-wide expression studies utilizing large data sets to analyze relative metal trafficking gene expressions would provide insight into this hypothesis. These bioinformatic studies could also be utilized to predict ZNA sensitivity in different malignancies, thereby generating an enrollment biomarker for future clinical trials with therapies designed to induce Zn^{2+} dyshomeostasis.

In conclusion, the small molecule ZNA has provided a tool for both the study of normal biological processes and malignant disease states. Substantial progress has been made towards understanding its biological mode of action but much of its biology has yet to be explored. In all, the application of a chemical biology approach towards understanding complex biological systems has proven fruitful and ZNA's expected contribution to our understanding of cancer will likely prove significant.

Methods

Tissue culture

All cells were cultured under standard conditions as described previously (1). MCF-7, MCF-10A, and T47D cells were a generous gift from Andrea Bild at the

University of Utah; MDA-MB-231 cells were obtained directly from the American Type Culture Collection (ATCC). All cell lines were authenticated by the ATCC in conjunction with Promega using short tandem repeat analysis.

Reagents and antibodies

The small molecule ZNA was synthesized as reported by Gibbons, J. B., Looper R. E., *et al*. (manuscript in preparation). Propidium iodide was obtained from Cell Signaling (Danvers, MA, USA). The Zn^{2+} indicator FluoZin-3 was obtained from Life Technologies (Carlsbad, CA, USA). Actinomycin D and chloroquine were obtained from Sigma (St. Louis, MO, USA). Antibodies against LC3A/B (Cell Signaling) and α-Tubulin (Sigma) were used at a concentration of 1:1000. IR800CW and IR680 secondary antibodies were obtained from LI-COR (Lincoln, NE, USA) and used at a concentration of 1:7500.

Dose response and clonogenic cell survival assays

All dose response assays were conducted as described previously (1). Cell viability was measured using an ATPlite assay (PerkinElmer, Waltham, MA, USA) following the manufacturer's protocol. Clonogenic cell survival assays were conducted as previously described (47).

Transcriptome sequencing

RNA was isolated using an RNeasy RNA isolation and purification kit (Qiagen, Hilden, Germany) per the manufacturer's protocol. Libraries were prepared for sequencing using standard Illumina protocols and sequencing was accomplished using an Illumina HiSeq instrument (Illumina, San Diego, CA, USA). Following completion of sequencing, genome alignment was conducted using NCBI build GRch37 and differential expression analysis was performed using the RNAseq application, which wraps the DESeq Bioconductor package (http://useq.sourceforge.net/cmdLnMenus.html#RNASeq); statistical significance was calculated as described by Anders and Huber (48). Sequencing data were deposited into Gene Expression Omnibus (accession number GSE59251).

Real-Time PCR (RT-PCR)

In preparation for RT-PCR, RNA was isolated using an RNeasy RNA isolation and purification kit (Qiagen). For tissue derived from mouse *in vivo* experiments, fresh tissue was homogenized using a TissueLyser II for 3 minutes at 30 Hz before isolating RNA. For experiments designed to measure gene expression, RT-PCR was conducted using a LightCycler 480 (Roche, Basel, Switzerland) and KAPA SYBR FAST qPCR Master Mix (Kapa Biosystems, Boston, MA, USA). Primers used have been reported previsouly (49). All data were normalized to internal reference genes and relative gene expression was assessed using the comparative CT method (50).

Measurement of intracellular Zn^{2+} by FluoZin-3 staining

Following the completion of treatment, the low serum (2% FBS) drug-containing media was removed and replaced with Hank's Balanced Salt Solution (HBSS, Life Technologies) containing 2.5 μM FluoZin-3. The cells were incubated with the indicator for 30 minutes at room temperature in the dark. After staining, the cells were trypsinized, resuspended in HBSS containing 2% FBS, and relative mean fluorescence was measured by flow cytometry (FACscan, BD Biosciences).

Measurement of cell death by propidium iodide staining

Following the completion of treatment, media and floating cells were collected and combined with trypsinized adherent cells. The cells were washed with 2% FBS/HBSS, and resuspended in a propidium iodide solution (Cell Signaling) for analysis by flow cytometry. The percentage of propidium iodide positive cells for each treatment condition were averaged and normalized to the vehicle-treated control.

Inductively coupled plasma-atomic emission spectroscopy
(ICP-AES) analysis

Following the completion of a 3-hour treatment, the media was discarded and the cells washed with 1xPBS. To each 10-cm plate, 1 mL of nitric acid (TraceSELECT Ultra for trace analysis, Sigma) was added directly to the plate. The nitric acid mixture was submitted for inductively coupled plasma-atomic emission spectroscopy (ICP-AES) analysis following methods established by the Environmental Protection Agency (51).

The experiment was performed in triplicate for each cell line and a fourth plate of cells was used to measure total protein (BCA assay, Thermo Fisher, Waltham, MA, USA). The ICP-AES data were then normalized to total protein for each cell line used.

Measurement of caspase activity

Caspase activity was measured using the Caspase Glo assay system (Promega, Madison, WI, USA) following the manufacturer's protocol.

Western blot analysis

All protein immunoblotting experiments were conducted as previously described (1).

Measurement of cellular proliferation

5-ethynyl-2′-deoxyuridine (EdU, Life Technologies) incorporation was used to measure cellular proliferation. Experiments were conducted according to the manufacturer's protocol and analyzed as previously described (1).

In vivo ZNA studies

Mouse studies were conducted with the approval of the University of Utah Institutional Animal Care and Use Committee. FVB/NJ mice were obtained from The

Jackson Laboratory (Bar Harbor, ME, USA). In preparation for the *in vivo* study, EF1α-PyMT mouse mammary tumors were generated in donor mice and the tumors resected and prepared as single cells as described previously by Smith *et al.* (22). These cells were suspended in Matrigel (BD Biosciences) and injected (50,000 cells per 10 μL injection) into the uncleared mammary fat pad of 3-week old female recipient FVB/NJ mice. Twenty-one days following the transplant, the mice were randomized and drug treatment was initiated; mice were treated once a day for 21 days and a tumor diameter ≥ 2 cm was established as an endpoint. ZNA (100 mg/kg) or the matched vehicle control was administered to each mouse via a 200-μL intraperitoneal injection of ZNA diluted into DMSO, then diluted into phosphate buffered saline to a final DMSO concentration of 5%. $ZnSO_4$ was administered continuously for the 21-day treatment period to the appropriate groups via drinking water (25 mM $ZnSO_4 \cdot 7H_2O$).

Statistics

The student's t-test (unpaired) was used to assess statistical significance and a $p \leq 0.05$ was considered statistically significant. Statistical significance between Kaplan-Meier survival curves was measured by the Mantel-Cox test using Prism 6.0 (GraphPad Software). The following p-values were used to annotate statistical significance: $p \leq 0.05$ = *; $p \leq 0.01$ = **; $p \leq 0.001$ = ***.

References

1. Gligorich K*, et al.* (2013) Development of a screen to identify selective small molecules active against patient-derived metastatic and chemoresistant breast cancer cells. *Breast Cancer Res* 15(4):R58.

2. Thirumoorthy N*, et al.* (2011) A review of metallothionein isoforms and their role in pathophysiology. *World J Surg Oncol* 9(1):54.

3. Thornalley PJ & Vašák M (1985) Possible role for metallothionein in protection against radiation-induced oxidative stress. Kinetics and mechanism of its reaction with superoxide and hydroxyl radicals. *Biochim Biophys Acta - Protein Structure and Molecular Enzymology* 827(1):36-44.

4. Chiaverini N & De Ley M (2010) Protective effect of metallothionein on oxidative stress-induced DNA damage. *Free Radic Res* 44(6):605-613.

5. Palmiter RD, Cole TB, & Dindley SD (1996) ZnT-2, a mammalian protein that confers resistance to zinc by facilitating vesicular sequestration. *EMBO J* 15(8):1784-1791.

6. Qin Y, Thomas D, Fontaine CP, & Colvin RA (2009) Silencing of ZnT1 reduces Zn2+ efflux in cultured cortical neurons. *Neurosci Lett* 450(2):206-210.

7. Snitsarev V*, et al.* (2001) Fluorescent detection of zn2+-rich vesicles with zinquin: mechanism of action in lipid environments. *Biophys J* 80(3):1538-1546.

8. Elmore S (2007) Apoptosis: A review of programmed cell death. *Toxicol Pathol* 35(4):495-516.

9. Earnshaw WC, Martins LM, & Kaufmann SH (1999) Mammalian caspases: structure, activation, substrates, and functions during apoptosis. *Annu Rev Biochem* 68(1):383-424.

10. Jänicke RU, Sprengart ML, Wati MR, & Porter AG (1998) Caspase-3 is required for DNA fragmentation and morphological changes associated with apoptosis. *J Biol Chem* 273(16):9357-9360.

11. Degterev A*, et al.* (2005) Chemical inhibitor of nonapoptotic cell death with therapeutic potential for ischemic brain injury. *Nat Chem Biol* 1(2):112-119.

12. Han W*, et al.* (2007) Shikonin circumvents cancer drug resistance by induction of a necroptotic death. *Mol Cancer Ther* 6(5):1641-1649.

13. He C & Klionsky DJ (2009) Regulation mechanisms and signaling pathways of autophagy. *Annu Rev Genet* 43(1):67-93.

14. Kabeya Y*, et al.* (2000) LC3, a mammalian homologue of yeast Apg8p, is localized in autophagosome membranes after processing. *EMBO J* 19(21):5720-5728.

15. Kimura T, Takabatake Y, Takahashi A, & Isaka Y (2013) Chloroquine in cancer therapy: a double-edged sword of autophagy. *Cancer Res* 73(1):3-7.

16. Wang Y, Zhu X, Yang Z, & Zhao X (2013) Honokiol induces caspase-independent paraptosis via reactive oxygen species production that is accompanied by apoptosis in leukemia cells. *Biochem Biophys Res Commun* 430(3):876-882.

17. Yang R*, et al.* (2014) Stearoyltyrosine protects against glutamate-induced oxidative toxicity by an apoptosis-inducing factor (aif)-mediated caspase-independent cell death pathway. *J Pharmacol Sci* 124(2):169-179.

18. Jambrina E*, et al.* (2003) Calcium influx through receptor-operated channel induces mitochondria-triggered paraptotic cell death. *J Biol Chem* 278(16):14134-14145.

19. Ho E & Ames BN (2002) Low intracellular zinc induces oxidative DNA damage, disrupts p53, NFκB, and AP1 DNA binding, and affects DNA repair in a rat glioma cell line. *Proc Natl Acad Sci USA* 99(26):16770-16775.

20. Zhou Z*, et al.* (2005) Zinc supplementation prevents alcoholic liver injury in mice through attenuation of oxidative stress. *Am J Pathol* 166(6):1681-1690.

21. Kilari S, Pullakhandam R, & Nair KM (2010) Zinc inhibits oxidative stress-induced iron signaling and apoptosis in Caco-2 cells. *Free Radic Biol Med* 48(7):961-968.

22. Smith BA*, et al.* (2012) Targeting the pymt oncogene to diverse mammary cell populations enhances tumor heterogeneity and generates rare breast cancer subtypes. *Genes Cancer* 3(9-10):550-563.

23. Espinoza A*, et al.* (2012) Iron, copper, and zinc transport: inhibition of divalent metal transporter 1 (DMT1) and human copper transporter 1 (hCTR1) by shRNA. *Biol Trace Elem Res* 146(2):281-286.

24. Guerinot ML (2000) The ZIP family of metal transporters. *Biochim Biophys Acta - Biomembranes* 1465(1–2):190-198.

25. Gees M, Colsoul B, & Nilius B (2010) The role of transient receptor potential cation channels in Ca2+ signaling. *Cold Spring Harb Perspect Biol* 2(10).

26. Ramsey IS, Delling M, & Clapham DE (2006) An introduction to TRP channels. *Annu Rev Physiol* 68(1):619-647.

27. Uchida K & Tominaga M (2013) Extracellular zinc ion regulates transient receptor potential melastatin 5 (TRPM5) channel activation through its interaction with a pore loop domain. *J Biol Chem* 288(36):25950-25955.

28. Bouron A, Kiselyov K, & Oberwinkler J (2014) Permeation, regulation and control of expression of TRP channels by trace metal ions. *Pflugers Arch - Eur J Physiol*:1-22.

29. Bouron A & Oberwinkler J (2014) Contribution of calcium-conducting channels to the transport of zinc ions. *Pflugers Arch - Eur J Physiol* 466(3):381-387.

30. Mwanjewe J & Grover AK (2004) Role of transient receptor potential canonical 6 (TRPC6) in non-transferrin-bound iron uptake in neuronal phenotype PC12 cells. *Biochem J* 378(3):975-982.

31. Li M, Jiang J, & Yue L (2006) Functional characterization of homo- and heteromeric channel kinases TRPM6 and TRPM7. *J Gen Physiol* 127(5):525-537.

32. Monteilh-Zoller MK*, et al.* (2003) TRPM7 provides an ion channel mechanism for cellular entry of trace metal ions. *J Gen Physiol* 121(1):49-60.

33. Hu H, Bandell M, Petrus MJ, Zhu MX, & Patapoutian A (2009) Zinc activates damage-sensing TRPA1 ion channels. *Nat Chem Biol* 5(3):183-190.

34. Gibon J*, et al.* (2011) The over-expression of TRPC6 channels in HEK-293 cells favours the intracellular accumulation of zinc. *Biochim Biophys Acta - Biomembranes* 1808(12):2807-2818.

35. Kovacs G*, et al.* (2011) Heavy metal cations permeate the TRPV6 epithelial cation channel. *Cell Calcium* 49(1):43-55.

36. Wagner TJ*, et al.* (2010) TRPM3 channels provide a regulated influx pathway for zinc in pancreatic beta cells. *Pflugers Arch - Eur J Physiol* 460(4):755-765.

37. Topala CN*, et al.* (2007) Molecular determinants of permeation through the cation channel TRPM6. *Cell Calcium* 41(6):513-523.

38. Dong X-P*, et al.* (2008) The type IV mucolipidosis-associated protein TRPML1 is an endolysosomal iron release channel. *Nature* 455(7215):992-996.

39. Harteneck C, Frenzel H, & Kraft R (2007) N-(p-amylcinnamoyl)anthranilic acid (ACA): A phospholipase A2 inhibitor and TRP channel blocker. *Cardiovasc Drug Rev* 25(1):61-75.

40. Kraft R, Grimm C, Frenzel H, & Harteneck C (2006) Inhibition of TRPM2 cation channels by N-(p-amylcinnamoyl)anthranilic acid. *Br J Pharmacol* 148(3):264-273.

41. Chai F, Truong-Tran AQ, Ho LH, & Zalewski PD (1999) Regulation of caspase activation and apoptosis by cellular zinc fluxes and zinc deprivation: a review. *Immunol Cell Biol* 77(3):272-278.

42. Hofmann T, Schaefer M, Schultz G, & Gudermann T (2002) Subunit composition of mammalian transient receptor potential channels in living cells. *Proc Natl Acad Sci USA* 99(11):7461-7466.

43. PK L & G B (2007) Molecular determinants of TRP channel assembly. *Biochem Soc Trans* 35:81-83.

44. Cheng W*, et al.* (2012) Heteromeric heat-sensitive transient receptor potential channels exhibit distinct temperature and chemical response. *J Biol Chem* 287(10):7279-7288.

45. Hellwig N, Albrecht N, Harteneck C, Schultz G, & Schaefer M (2005) Homo- and heteromeric assembly of TRPV channel subunits. *J Cell Sci* 118(5):917-928.

46. Schaefer M (2005) Homo- and heteromeric assembly of TRP channel subunits. *Pflugers Arch - Eur J Physiol* 451(1):35-42.

47. Franken NAP, Rodermond HM, Stap J, Haveman J, & van Bree C (2006) Clonogenic assay of cells in vitro. *Nat Protocols* 1(5):2315-2319.

48. Anders S & Huber W (2010) Differential expression analysis for sequence count data. *Genome Biol* 11(10):R106.

49. Xu Y-Q*, et al.* (2012) Diurnal variation of hepatic antioxidant gene expression in mice. *PLoS ONE* 7(8):e44237.

50. Schmittgen TD & Livak KJ (2008) Analyzing real-time PCR data by the comparative CT method. *Nat Protocols* 3(6):1101-1108.

51. Martin TD, Brockhoff CA, & Creed JT (1994) Method 200.7 Determination of Metals and Trace Elements in Water and Wastes by Inductively Coupled Plasma-Atomic Emission Spectrometry. *Environmental Monitoring Systems Laboratory, US Environmental Protection Agency*.

CHAPTER 6

CONCLUSION

Cancer is a living, dynamic entity. It is characterized by its ruthless drive to survive, but its opportunistic nature, paradoxically, leads it to exploit host resources until neither survives. The combined cancer mortality rates of men and women declined by only 12.1% between the years of 1950 and 2010 (1). This statistic is a direct reflection of the deep, innate complexity of cancer and its heterogeneous and adaptable nature. Significant, continued efforts aimed at understanding the molecular characteristics of cancer will be required by the scientific community if the disease is to be eradicated in our lifetimes.

Herein was presented work describing our efforts to define biological pathways in drug insensitive cancer cells that can be targeted for therapeutic intervention. Considering the significant lack of therapies available to patients who have developed drug-refractory and metastatic malignancies following initial treatments with frontline chemotherapeutics, we sought to both define the underlying biology of chemoresistance and also to establish pathways that might be exploited for therapeutic gain. Implementing a chemical biology approach, we established a unique small molecule screen utilizing malignant pleural effusion cells derived from drug-refractory breast cancer patients. Considering the relatively indiscriminant toxicities of currently prescribed chemotherapeutics, immortalized human mammary epithelial cells were incorporated into the screen such that molecules with cancer-specific phenotypes could be identified. From this screen, fourteen novel small molecules were identified for their ability to reduce the viability of the malignant pleural effusion cells while eliciting little to no effect on untransformed mammary epithelial cells. Two of these molecules, C-6 and zinaamidole (ZNA), were chosen for further mechanistic studies.

While the results of our studies revealed that C-6 and ZNA exerted their cancer-

selective cytotoxic effects via different biological mechanisms, a common theme was observed: the induction of caspase independent cell death. The role of caspase signaling in cell death has been studied extensively; defects in caspase signaling and apoptosis have also been well documented in some cancers (2, 3). As such, targeting caspase independent cell death may prove to be a beneficial strategy for the development of new therapeutics for late-stage, drug insensitive cancers. In addition to the common theme of caspase independent cell death, ion dyshomeostasis may comprise a shared mechanistic trait between C-6 and ZNA, although this is less clear in the case of C-6. Although evidence directly supporting the role of ion imbalances in C-6-induced cell death was not found, the characteristics of the cell death induced by the small molecule are consistent with ion dyshomeostasis. Specifically, the induction of endoplasmic reticulum stress, the strong mitochondrial disruption phenotype, and the observed caspase independent cell death have all been reported to occur in conjunction with perturbations in ion homeostasis (4-8). Considering then that both molecules may induce their cancer-selective effects via ion channel modulation, this brings to light the idea that targeting ion channels may be a useful strategy for cancer treatment. Furthermore, the cancer-selective nature of both molecules suggests that ion channels may be differentially expressed in malignant cell types such that wide therapeutic treatment windows might be obtained with an appropriately discerning drug. This approach is not without caveats though. Ion channels are expressed ubiquitously in every cell type and play critical roles in the function of excitable cells such as cardiac cells and neurons. Considering this, *in vivo* testing will be critical in the early stages of preclinical research to establish the effects of new therapeutics on cardiac/muscle function and also on the central nervous system.

In all, our multifaceted approach towards cancer research, incorporating

chemistry, molecular biology, and clinical oncology resources, has resulted in the identification of two molecular tools by which to investigate and untangle the complexities of cancer. More broadly though, this approach has allowed for new insight into the disease, hinting at the promise of both caspase independent cell death and ion dyshomeostasis for future therapeutic development. Despite the seemingly insurmountable research challenge presented by cancer, continued work is required to both define its origins and understand its vulnerabilities. Each small gain in our understanding of the molecular characteristics of cancer leads us closer to the development of new prevention and detection strategies in addition to more focused, more effective treatments.

References

1. Howlader N*, et al.* (2013) SEER Cancer Statistics Review, 1975-2010. *National Cancer Institute*, Bethesda, MD.

2. PK L & G B (2007) Molecular determinants of TRP channel assembly. *Biochem Soc Trans* 35:81-83.

3. Hanahan D & Weinberg RA (2011) Hallmarks of cancer: the next generation. *Cell* 144(5):646-674.

4. Papa L, Gomes E, & Rockwell P (2007) Reactive oxygen species induced by proteasome inhibition in neuronal cells mediate mitochondrial dysfunction and a caspase-independent cell death. *Apoptosis* 12(8):1389-1405.

5. Bury M*, et al.* (2013) Ophiobolin A induces paraptosis-like cell death in human glioblastoma cells by decreasing BKCa channel activity. *Cell Death Dis* 4:e561.

6. Schneider D*, et al.* (2004) Intracellular acidification by inhibition of the Na+/H+-exchanger leads to caspase-independent death of cerebellar granule neurons resembling paraptosis. *Cell Death Differ* 11(7):760-770.

7. Kroemer G & Martin SJ (2005) Caspase-independent cell death. *Nat Med*

11(7):725-730.

8. Bröker LE, Kruyt FAE, & Giaccone G (2005) Cell death independent of caspases: a review. *Clin Cancer Res* 11(9):3155-3162.